Biannual Report Feb 1986 PART 1

GRANT NAG -1-444

FINITE ELEMENT ANALYSIS OF STEADY AND TRANSIENTLY

MOVING/ROLLING NONLINEAR VISCOELASTIC STRUCTURE;

PART I - THEORY

Joe Padovan

Depts. of Mechanical and Polymer Engineering

University of Akron

Akron, Ohio 44325

Abstract

    In a three part series of papers, a generalized finite element analysis scheme is developed to handle the steady and transient response of moving/ rolling nonlinear viscoelastic structure. This paper considers the development of the moving/rolling element strategy, including the effects of large deformation kinematics and viscoelasticity modelled by fractional integro-differential operators. To improve the solution strategy, a special hier-archical constraint procedure is developed for the case of steady rolling/ translating as well as a transient scheme involving the use of a Grunwaldian representation of the fractional operator. In the second and third parts of the paper, 3-D extensions are developed along with transient contact strategies enabling the handling of impacts with obstructions. Overall the various developments are benchmarked via comprehensive 2- and 3-D simulations. These are correlated with experimental data to define modelling capabilities.

I. Introduction

While extensive effort has been given to handling the response of structure with fixed loading sites [1-3], much less is available for problems wherein either the load or contact regions move [4-10]. In this context, such structures as tires, rollers, compressors, bearings, pumps, turbines and manufacturing equipment (lathes, grinders, mills), all are typically excited by some form of traveling/moving load or boundary condition. Such problems have been partially addressed in the recent works of several authors [4-12]. For instance, Padovan et al. [6-10] introduced the use of so called moving coordinate systems to handle traveling/rolling/ rotating structural systems. This includes both total and updated formulations [9] involving primarily Hookean and Kelvin Voigt type formulations and 2-D benchmarks [6-10].

In the context of the foregoing this paper series will extend previous work by considering the development of large deformation viscoelastic FE formulations for steady and transient traveling/rolling/rotating structure. Overall special emphasis will be given to:

   i)   The development of large deformation viscoelastic moving finite element (FE) formulations involving nonlinear elasticity [13] and damping characteristics modelled by fractional integrodifferential operators [14,15];

   ii)   The creation of a specialized hierarchically constrained Newton Raphson solution scheme for steady rolling problems;

   iii) The development of an implicit transient solver which incorporates a Grunwaldian type simulation [16] of the fractional integro-

differential operator used to simulate the viscoelastic material behavior;

iv) The development of 3-D translating/rolling cubic isoparametric type elements;

v) The development of rolling/translating type shell elements;

vi) The creation of 3-D moving contact strategies;

vii) Comprehensive 3-D simulation of a steadily rolling tire where analysis is correlated with experimentally derived tire test data;

viii) The creation of transient rolling contact schemes capable of dealing with impacts with holes/bumps;

ix) Integrating rolling/translating FE scheme with transient contact methodology; and,

x) Comprehensively benchmark scheme with transient simulations of tire roll over events involving holes and bumps.

Due to the number of topics covered, the overall paper is separated into three parts. The first covers items i) - iv). The second outlines iv) - vii). Lastly, the third covers items viii) - x).

II   Governing Field Equations

To enable the modelling of rolling/moving structure undergoing large deformations, we shall employ the 2nd Piola Kirchhoff stress and Lagrangian strain tensor combination [9,17]. Secondly, to handle the moving/rolling motion, a change of reference base is used to define the requisite recti-

linear, Coriolis and centripetal accelerations. This yields the following equations of motion, namely

$$(S_{jk}(\delta_{ik} + u_{i,k})),j + f_i =$$

$$\rho \frac{d^2}{dt^2}(u_i) + 2\rho\varepsilon_{imn}\Omega_m \frac{d}{dt}(u_n) + \rho\varepsilon_{inr}\varepsilon_{mnk}\Omega_r\Omega_k u_m \qquad (2.1)$$

where δ_{ij}, S_{ij}, u_i, f_i, Ω_m, ρ and $d()/dt$ respectively define the Kronecker delta, the second Piola-Kirchhoff stress tensor, the displacement, body force, rotation vector, initial density and comoving time derivative. Since viscoelastic media are considered,

$$S_{ij} = S_{ij}(L_{11},\ldots, \frac{d}{dt}L_{11},\ldots) \qquad (2.2)$$

such that L_{ij} the Lagrangian strain tensor is defined by

$$L_{ij} = \frac{1}{2}(u_{i,i} + u_{j,i} + u_{\ell,i}u_{\ell,j}) \qquad (2.3)$$

The boundary conditions associated with (2.1) - (2.3) take the form

i) For $x_i \varepsilon \partial R_\sigma$;

$$S_{jk}(\delta_{ik} + u_{i,k})n_j = S_i \qquad (2.4)$$

ii) For $x_i \varepsilon \partial R_u$;

$$u_i = U_i \qquad (2.5)$$

where

$$\partial R = \partial R_u + \partial R_\sigma \qquad (2.6)$$

such that ∂R defines the surface of R. Since we are considering translating/rolling structures, the loads defined on certain of the boundaries are of the moving type namely

$$S_i = S_i(\underset{\sim}{x} - \underset{\sim}{c}(t),t) \qquad (2.7)$$

such that the vector $\underset{\sim}{x}$ defines the initial coordinates, $\underset{\sim}{c}(t)$ the trajectory undertaken by the load and t is time. Based on the functional dependence defined by (2.7), the various dependent field variables have the following form that is

$$S_{ij} = S_{ij}(\underset{\sim}{\eta},t)$$
$$u_i = u_i(\underset{\sim}{\eta},t) \qquad (2.8)$$
$$L_{ij} = L_{ij}(\underset{\sim}{\eta},t)$$

where

$$\underset{\sim}{\eta} = \underset{\sim}{\eta}(\underset{\sim}{x},r,\theta,t) \qquad (2.9)$$

with $\underset{\sim}{\eta}$ denoting the Galilean type position vector [9], and (r,θ) the radial and circumferential locations relative to the center of rotation.

Employing the functional representation defined by (2.8), the comoving derivative takes the form [10]

$$\frac{d}{dt}(\underset{\sim}{u}) = \frac{\partial}{\partial t}(\underset{\sim}{u}) + \Psi(\underset{\sim}{u}) \qquad (2.10)$$

$$\frac{d^2}{dt^2}(\underset{\sim}{u}) = \frac{\partial^2}{\partial t^2}(\underset{\sim}{u}) + 2\Psi(\frac{\partial}{\partial t}(\underset{\sim}{u})) + \gamma(\underset{\sim}{u}) \qquad (2.11)$$

$$\underset{\sim}{u} = \left\{ \begin{array}{c} u_1 \\ u_2 \\ u_3 \end{array} \right\} \qquad (2.12)$$

where the differential operators Ψ and γ are defined in the Appendix. For steadily translating/rolling structure, (2.10) and (2.11) reduce to

$$\frac{d}{dt}(\underset{\sim}{u}) = \Psi(\underset{\sim}{u}) \qquad (2.13)$$

and

$$\frac{d^2}{dt^2}(\underset{\sim}{u}) = \gamma(\underset{\sim}{u}) \qquad (2.14)$$

To enable the derivation of the requisite FE formulation, (2.1) -
(2.6), (2.10) and (2.11) can be employed to yield the virtual work prin-
ciple cast in moving coordinates. After several manipulations we yield
the expression

$$\int_R \{\delta(L)^T S + \delta(u)^T([m_1] \frac{\partial^2}{\partial t^2} (u) +$$

$$[[m_2] + 2[m_1]\Psi(\ )] \frac{\partial}{\partial t} (u) + [[m_3] +$$

$$[m_2]\Psi(\ ) + [m_1]\gamma(\ )]u)\} dv$$

$$=$$

$$\int_{\partial R} S_{jk}(\delta_{ik} + u_{i,k})n_j du_i ds \tag{2.15}$$

where $(\ )^T$ denotes matrix transposition, $\delta(\ )$ the first variation and

$$S^T = (S_{11}, S_{22}, S_{33}, S_{12}, S_{23}, S_{13}) \tag{2.16}$$

$$L^T = (L_{11}, L_{22}, L_{33}, L_{12}, L_{23}, L_{13}) \tag{2.17}$$

$$[m_1] \equiv \rho[I] \tag{2.18}$$

$$[m_2] \equiv 2\rho\varepsilon_{imn}\Omega_m \tag{2.19}$$

$$[m_3] \equiv \rho\varepsilon_{inr}\varepsilon_{mnk}\Omega_r\Omega_k \tag{2.20}$$

For the case of steady rolling/translating, (2.14) reduces to the form

$$\int_R \{\delta(L)^T S + \delta(u)^T[[m_3] + [m_2]\Psi(\ ) + [m_1]\gamma(\ )]u\} dv =$$

$$\int_{\partial R} S_{jk}(\delta_{ik} + u_{i,k}) n_j \delta u_i ds \tag{2.21}$$

where here due to the use of Galilean type coordinates [9], time is removed
from the formulation for both linear and nonlinear situations.

The preceeding formulations were cast in so called total Lagrangian form wherein all kinematic fields are referenced relative to the initial configuration. Alternatively, for very large deformation situations, the updated Lagrangian strategy can be used. For such a formulation, the reference base is reassigned intermittantly to intermediate kinematic states. In this context u_i, S_{ij} and L_{ij} are recast in the form

$$u_i = V_i + {_\tau}u_i$$

$$L_{ij} = L_{ij} + {_\tau}L_{ij} \qquad\qquad (2.22)$$

$$S_{ij} = S_{ij} + {_\tau}S_{ij}$$

where (V_i, L_{ij}, S_{ij}) and $({_\tau}u_i, {_\tau}L_{ij}, {_\tau}S_{ij})$ are respectively the displacement, strain and stress fields defining the reference state at τ and their associated excursions. Based on (2.21), (2.14) takes the form

$$\int_{_\tau R} \{\delta({_\tau}\underset{\sim}{L})^T_\tau \underset{\sim}{S} + \delta({_\tau}\underset{\sim}{L}^*)^T \underset{\sim}{S} + \delta({_\tau}\underset{\sim}{u})([m_1] \frac{\partial^2}{\partial t^2} ({_\tau}\underset{\sim}{u}) +$$

$$[[m_2] + 2[m_1]\Psi[1] \frac{\partial}{\partial t} ({_\tau}\underset{\sim}{u}) + [[m_3] +$$

$$[m_2]\Psi(\ ) + [m_1]\gamma(\ )]{_\tau}\underset{\sim}{u})\} \, dv =$$

$$\int_{\partial_\tau R} ({_\tau}S_{jk}(\delta_{ik} + V_{i,k} + {_\tau}u_{i,k}) +$$

$$S_{jk}\,{_\tau}u_{i,k}) \, n_j\delta({_\tau}u_i) \, ds \qquad\qquad (2.23)$$

where

$$\delta({_\tau}\underset{\sim}{L}) \equiv \frac{1}{2} \{\delta({_\tau}u_{i,j} + \delta({_\tau}u_{j,i}) +$$

$$V_{\ell,i}\delta({_\tau}u_{\ell,j}) + V_{\ell,j}\delta({_\tau}u_{\ell,i}) +$$

$$_\tau u_{\ell,i}\delta({_\tau}u_{\ell,i}) + \delta({_\tau}u_{\ell,i})_\tau u_{\ell,j}\} \qquad\qquad (2.24)$$

$$\delta(_\tau\underset{\sim}{L}^*) \equiv u_{i,k}\delta(_\tau u_j) \tag{2.25}$$

For the steady case, (2.23) reduces to the form

$$\int_{_\tau R} \{\delta(_\tau\underset{\sim}{L})^T \underset{\sim}{_\tau S} + \delta(_\tau\underset{\sim}{L}^*)^T \underset{\sim}{S} + \delta(_\tau\underset{\sim}{u})[[m_3] +$$

$$[m_2]\Psi(\ ) + [m_1]\gamma(\ )]_\tau\underset{\sim}{u}\} \, dv =$$

$$\int_{\partial_\tau R} (_\tau S_{jk}(\delta_{ik} + V_{i,k} + _\tau u_{i,k}) +$$

$$S_{jk}\,_\tau u_{i,k})\, n_j\delta(_\tau u_i) \, ds \tag{2.26}$$

III. Viscoelastic Material Properties

To complete the set of governing field equations, constitutive relations need to be defined. For the current purposes we shall consider the translating/rolling of viscoelastic structure. Since rolling/translating on smooth or uneven surfaces involves a wide range of speeds and potential spectral excitations, the viscoelastic formulation must be able to accommodate such factors. In this context it is well known that the use of the traditional Kelvin Voigt [17] simulation cannot handle problems involving a perfusion of spectra. Because of this we turn to the use of fractional integrodifferential representations [16]. As shown by Bagley and Torvik, [14,15] such operators have an improved capacity to handle frequency variations.

To enable the development of such a formulation, we recall the classical generalized Maxwell-Kelvin-Voigt type representation, namely [17]

$$S_{ij} + \sum_\ell \mu_{ijab}^{(\ell)} \frac{d^\ell}{dt^\ell}(S_{ab}) = G_{ij}(L_{11},L_{22},\ldots) + \sum_\ell \alpha_{ijab}^{(\ell)} \frac{d^\ell}{dt^\ell}(L_{ab}) \tag{3.1}$$

where here $\mu_{ijab}^{(\ell)}$ and $\alpha_{ijab}^{(\ell)}$ are respectively the compliance and

stiffness properties of the various stress and strain rate terms. Note $G_{ij}(L_{11},...)$ defines the nonlinear elastic behavior which say in the case of rubber would be the Mooney-Rivilin correlation [13]. Reinterpreting the integer ordered differential operators appearing in (3.1) to be of the more comprehensive fraction type [14-16], we yield the expression

$$S_{ij} + \sum_{\ell} u^{(\ell)}_{ijab} D_{p_\ell}(S_{ab}) =$$

$$G_{ij}(L_{11},L_{22},...L_{13}) + \sum_{\ell} \alpha^{(\ell)}_{ijab} D_{q_\ell}(L_{ab}) + \beta_{ijab} \frac{d}{dt}(L_{ab}) \qquad (3.2)$$

such that here in Riemann-Liouville form

$$D_{p_\ell}(S_{ab}) = \frac{1}{\Gamma(-P_\ell)} \int_o^t \frac{1}{(t-\tau)^{P_\ell}} S_{ab}(\tau) \, d\tau \qquad (3.3)$$

with Γ defining the gamma function [18]. Alternatively, $D_{p_\ell}(\ )$ can be expressed in the computationally more convenient but equivalent form developed by Grunwald[16] namely

$$D_{p_\ell}(S) = \sum_j (\Delta t)^{-P_\ell} A(p_\ell,j+1)S(t-j\Delta t) \qquad (3.4)$$

such that

$$A(p_\ell,j+1) = (-1)^j \binom{P_\ell}{j} = \frac{\Gamma(j-p_\ell)}{\Gamma(-p_\ell)\Gamma(j+1)} \qquad (3.5)$$

Note, the coefficients $A(p_\ell,j+1)$ denote the memory of the material. For appropriately chosen p_ℓ, they represent an essentially monotone decreasing set. As p_ℓ the order of the fractional derivative can be experimentally chosen [14,15], a wide ranging series of histories can be accommodated by (3.2).

To expedite the development of the requisite solution algorithm, (3.2) is converted to matrix form namely

$$\underset{\sim}{S} + \sum_{\ell} [\mu^{(\ell)}] D_{P_\ell} (\underset{\sim}{S}) =$$

$$\underset{\sim}{G}(\underset{\sim}{L}) + \sum_{\ell} [\alpha^{(\ell)}] D_{q_\ell} (\underset{\sim}{L}) + [\beta] \frac{d}{dt} (\underset{\sim}{L}) \tag{3.6}$$

where here

$$[\mu^\ell] \equiv \mu^{(\ell)}_{ijab}$$

$$[\alpha^{(\ell)}] \equiv \alpha^{(\ell)}_{ijab} \tag{3.7}$$

$$[\beta] \equiv \beta_{ijab}$$

and based on (3.4) we see that

$$D_{P_\ell} (\underset{\sim}{S}) = (\Delta t)^{-P_\ell} \sum_{j=0} A(p_{\ell,j+1}) \underset{\sim}{S}(\underset{\sim}{x}, t-j\Delta t) \tag{3.8}$$

$$D_{q_\ell} (\underset{\sim}{L}) = (\Delta t)^{-q_\ell} \sum_{j=0} A(q_{\ell,j+1}) \underset{\sim}{L}(\underset{\sim}{x}, t-j\Delta t) \tag{3.9}$$

Since we are dealing with rolling/translating structure, recalling the use of the Galilean transform [9], it follows that (3.6) converts to the form

$$\underset{\sim}{S}(\eta,t) +$$

$$\sum_{\ell} [\mu^{(\ell)}](\Delta t)^{-P_\ell} \sum_{j} A(p_{\ell,j+1}) \underset{\sim}{S}(\eta(\underset{\sim}{x}-\underset{\sim}{c}(t-j\Delta t)), t-j\Delta t) =$$

$$\underset{\sim}{G}(\underset{\sim}{L}(\eta,t)) + [\beta](\Psi(\underset{\sim}{L}(\eta,t)) + \frac{d}{dt} (\underset{\sim}{L}(\eta,t)) +$$

$$\sum_{\ell} [\alpha^{(\ell)}](\Delta t)^{-q_\ell} \sum_{j} A(q_{\ell,j+1}) L(\eta(x-c(t-j\Delta t)), t-j\Delta t) \tag{3.10}$$

To recast (3.10) into a more convenient form, it must be recognized that the family of terms defined by $\underset{\sim}{S}(\eta(\underset{\sim}{x}-\underset{\sim}{c}(t-j\Delta t)), t-j\Delta t)$ and $\underset{\sim}{L}(\eta(\underset{\sim}{x}-\underset{\sim}{c}(t-j\Delta t)), t-j\Delta t)$ $j\epsilon[0,\infty)$ represents the history of a given particle. Obviously the particle occupies different locations during its history. For simplicity we shall designate the succession of positions by the nomenclature

$(r,m,t+\Delta t)$ such that r designates the radial position, m the circumferential positions and $t+\Delta t$ the time.

For rotating bodies, the mth circumferential location is defined by $j\Delta\underset{\sim}{\eta}_r$ wherein

$$\Delta\underset{\sim}{\eta}_r = \underset{\sim}{c}_r\Delta t \tag{3.11}$$

In this context at time t the location of the particle is given by $(r,m-1,t)$. Based on such nomenclature, S is cast in the form $_{t+\Delta t}\underset{\sim}{S}^{(r,m)}$

$$_{t+\Delta t}\underset{\sim}{S}^{(r,m)} \equiv \underset{\sim}{S}(\underset{\sim}{\eta}_r + (m+kJ_r)\Delta\underset{\sim}{\eta}_r,t+\Delta t) \tag{3.12}$$

such that $\underset{\sim}{\eta}_r$ is the initial position, k the total number of complete revolutions, J_r the number of time increments required to define a given revolution and $\Delta\underset{\sim}{\eta}_r$ the incremental circumferential motion of the rth position. In a similar context, we see that

$$_{t+\Delta t}\underset{\sim}{L}^{(r,m)} = \underset{\sim}{L}(\underset{\sim}{\eta}_r + (m+kJ_r)\Delta\underset{\sim}{\eta}_r,t+\Delta t) \tag{3.13}$$

Employing the foregoing nomenclature, it follows that (3.6) reduces to

$$_{t+\Delta t}\underset{\sim}{S}^{(r,m)} + \sum_\ell [\mu^{(\ell)}]D_{p_\ell}(_{t+\Delta t}\underset{\sim}{S}^{(r,m)}) =$$

$$\underset{\sim}{G}(_{r+\Delta t}\underset{\sim}{L}^{(r,m)}) + [\beta](\Psi(_{t+\Delta t}\underset{\sim}{L}^{(r,m)}) +$$

$$\frac{\partial}{\partial t}(_{t+\Delta t}\underset{\sim}{L}^{(r,m)}) + \sum_\ell [\alpha^{(\ell)}]D_{q_\ell}(_{t+\Delta t}\underset{\sim}{L}^{(r,m)})) \tag{3.14}$$

Generally the solution to FE simulations involves the use of tangent type material formulations. In this context, we note that

$$_{t+\Delta t}\underset{\sim}{S}^{(r,m)} = \Delta\underset{\sim}{S}^{(r,m)} + {}_t\underset{\sim}{S}^{(r,m-1)} \tag{3.15}$$

$$_{t+\Delta t}\underset{\sim}{L}^{(r,m)} = \Delta\underset{\sim}{L}^{(r,m)} + {}_{t}\underset{\sim}{L}^{(r,m-1)} \tag{3.16}$$

and

$$\underset{\sim}{G}({}_{t+\Delta t}\underset{\sim}{L}^{(r,m)}) = [D_T^{(r,m)}]\ \Delta\underset{\sim}{L}^{(r,m)} + \underset{\sim}{G}({}_{t}\underset{\sim}{L}^{(r,m-1)}) \tag{3.17}$$

where here $[D_T]$ defines the tangent elastic properties. Based on these expressions, it follows that (3.14) reduces to the form

$$\Delta\underset{\sim}{S}^{(r,m)} + {}_{t}\underset{\sim}{S}^{(r,m-1)} +$$

$$\sum_{\ell} [\mu^{(\ell)}](\Delta t)^{-p_\ell} \{A(p_\ell,1)(\Delta\underset{\sim}{S}^{(r,m)} + {}_{t}\underset{\sim}{S}^{(r,m-1)}) +$$

$$\sum_{j=1} A(p\ell,j+1){}_{t-(j-1)\Delta t}\underset{\sim}{S}^{(r,m-j)}\} \ =$$

$$\underset{\sim}{G}({}_{t}\underset{\sim}{L}^{(r,m-1)}) + [D_T^{(r,m)}]\ \Delta\underset{\sim}{L}^{(r,m)} +$$

$$\sum_{\ell} [\alpha^{(\ell)}](\Delta t)^{-q_\ell} \{A(q_\ell,1)(\Delta\underset{\sim}{L}^{(r,m)} + {}_{t}\underset{\sim}{L}^{(r,m-1)}) +$$

$$\sum_{j=1} A(q_\ell,j+1){}_{t-(j-1)\Delta t}\underset{\sim}{L}^{(r,m-1)}\} +$$

$$[\beta] \{\Psi(\Delta\underset{\sim}{L}^{(r,m)}) + \Psi({}_{t}\underset{\sim}{L}^{(r,m-1)}) +$$

$$\frac{\partial}{\partial t} (\Delta\underset{\sim}{L}^{(r,m)} + {}_{t}\underset{\sim}{L}^{(r,m-1)})\} \tag{3.18}$$

At time t the prior location of the particle is (r,m-1), hence we have that

$$_{t}\underset{\sim}{S}^{(r,m-1)} +$$

$$\sum_{\ell}[\mu^{(\ell)}](\Delta t)^{-p_\ell} \sum_{j=0} A(p_\ell,j+1){}_{t-j\Delta t}\underset{\sim}{S}^{(r,m-1-j)} \ =$$

$$\underset{\sim}{G}({}_{t}\underset{\sim}{L}^{(r,m-1)}) +$$

(over)

$$\sum_\ell \, [\alpha^{(\ell)}](\Delta t)^{-p_\ell} \, \sum_{j=0} \, A(q_\ell, j+1)_{t-j\Delta t} \underset{\sim}{L}^{(r,m-1-j)} \quad +$$

$$[\beta] \, \{\Psi(_{t}\underset{\sim}{L}^{(r,m-1)}) + \frac{\partial}{\partial t} \, (_{t}\underset{\sim}{L}^{(r,m-1)})\} \tag{3.19}$$

Differencing (3.18) and (3.19) we yield the incremental expression

$$[\mu^{(r,m)}] \, \Delta \underset{\sim}{S}^{(r,m)} \quad =$$

$$[\alpha^{(r,m)}] \, \Delta \underset{\sim}{L}^{r,m} + [\beta] \, \Psi(\Delta \underset{\sim}{L}^{(r,m)}) \quad +$$

$$[\beta] \, \frac{\partial}{\partial t} \, (\Delta \underset{\sim}{L}^{(r,m)}) + _{t+\Delta t}\underset{\sim}{h}^{(r,m)}_{\mu\alpha\beta} \tag{3.20}$$

where

$$[\mu^{(r,m)}] = [[I] + \sum_\ell \, (\Delta t)^{-p_\ell} A(p_\ell, 1)]\mu^{(\ell)}]] \tag{3.21}$$

$$[\alpha^{(r,m)}] = [[D_T^{(r,m)}] + \sum_\ell \, (\Delta t)^{-q_\ell} A(q_\ell, 1)[\alpha^{(\ell)}]] \tag{3.22}$$

and

$$_{t+\Delta t}\underset{\sim}{h}^{(r,m)}_{\mu\alpha\beta} = \sum_\ell \, (\Delta t)^{-q_\ell} \, [\alpha^{(\ell)}] \, \sum_{j=0} \, (A(q_\ell, j+2) - (1-$$

$$sgn(j,0))A(q_\ell, j+1))_{t-j\Delta t}\underset{\sim}{L}^{(r,m-1-j)} \quad -$$

$$\sum_\ell \, (\Delta t)^{-p_\ell} \, [\mu^{(\ell)}] \, \sum_{j=0} \, (A(p_\ell, j+2) - (1-$$

$$sgn(j,0))A(p_\ell, j+1))_{t-j\Delta t}\underset{\sim}{S}^{(r,m-1-j)} \tag{3.23}$$

IV. FE Formulation

For the current purposes, a displacement type representation is employed to develop the requisite FE formulation. In this context we have that [2]

$$\underset{\sim}{u} = [N]\underset{\sim}{Y} \qquad (4.1)$$

where [N] is the shape function and $\underset{\sim}{Y}$ the nodal deflections. For transient situations it follows that [9,10]

$$[N] = [N(\underset{\sim}{\eta})] \qquad (4.2)$$

and [10]

$$\underset{\sim}{Y} = Y(t) \qquad (4.3)$$

Based on (4.1), (2.10) and (2.11) yield the following expressions for velocity and acceleration, namely

$$\frac{d}{dt} (\underset{\sim}{u}) = \Psi ([N])\underset{\sim}{Y} + [N] \frac{\partial}{\partial t} (\underset{\sim}{Y}) \qquad (4.4)$$

$$\frac{d^2}{dt^2} (\underset{\sim}{u}) = \gamma ([N])\underset{\sim}{Y} + 2\Psi([N]) \frac{\partial}{\partial t} (\underset{\sim}{Y}) + [N] \frac{\partial^2}{\partial t^2} (\underset{\sim}{Y}) \qquad (4.5)$$

Continuing, $\delta\underset{\sim}{L}$ takes the form [9]

$$\delta\underset{\sim}{L} = [B*]\delta\underset{\sim}{Y} \qquad (4.6)$$

Employing (4.4) - (4.6), (2.14) can be used to develop the following FE formulation, that is

$$\int_R \{[B*]^T \underset{\sim}{S} + [N]^T([m_1][N]\ddot{\underset{\sim}{Y}} +$$

$$[[m_2][N] + 2[m_1]\Psi([N])]\dot{\underset{\sim}{Y}} + [[m_3][N] + [m_3]\Psi([N]) +$$

$$[m_1]\gamma([N])]\underset{\sim}{Y})\} \ dv = \underset{\sim}{F} \qquad (4.7)$$

In the case of steady translating/rolling Eq. (4.7) reduces to the form

$$\int_R \{[B^*]\underset{\sim}{S} + [N]^T([m_3][N] +$$

$$[m_2]\Psi([N]) + [m_1]\gamma([N]))\underset{\sim}{Y} \} \, dv = F \qquad (4.8)$$

Since (4.7) and (4.8) are inherently nonlinear, numerical schemes are required to generate their solution. This will be developed in the next section.

V. Solution Algorithms

The FE simulations given by (4.7) and (4.8) respectively define transient and steady state aspects of the translating/rolling problem. Solution algorithms to such models are developed in the succeeding subsections.

V.1 Steady Problem

Since (4.8) is inherently nonlinear, the Newton-Raphson scheme will be employed to affect its solution. To improve the resulting algorithms' stability and self adaptiveness, a locally constrained version will be developed. To start, (4.8) is recast in incremental form namely

$$\int_R \{[G]^T[S][G] + [B^*]\Delta\underset{\sim}{S} + [[m_3][N] + [m_2]\Psi([N]) +$$

$$[m_1]\gamma([N])]\Delta Y \} \, dv = \Delta\underset{\sim}{F} \qquad (5.1)$$

such that [S] is the prestress matrix. At this stage, it must be recognized that due to the viscoelastic properties, (5.1) must reflect the appropriate history effects on $\Delta\underset{\sim}{S}$. In this context, for each point in the domain given by R, $\Delta\underset{\sim}{S}$ and [S] must be linked to its past so as to define the requisite history effects. Hence, (5.1) is recast as follows:

$$\int_R \{[G^{(r,m)}]^T[_{t+\Delta t}S^{(r,m)}][G^{(r,m)}] +$$

$$[B^{*(r,m)}]\Delta\underset{\sim}{S}^{(r,m)} + [[m_3][N] + [m_2]\Psi([N]) +$$

$$[m_1]\gamma([N])]\Delta\underset{\sim}{Y}^{(r,m)}\} = \Delta\underset{\sim}{F}^{(r,m)}$$

Employing (3.20) in conjunction with (5.1) we yield the following assembled algorithmic expression

$$_i\Delta\underset{\sim}{Y} = {_{i-1}}[K]^{-1}(_i\Delta\underset{\sim}{F} - {_i}\underset{\sim}{H}_{\mu\alpha\beta}) \tag{5.2}$$

$$_{i-1}[K] = {_{i-1}}[[K_T] + [K_{\mu\beta}] + [K_\rho]] \tag{5.3}$$

where

$$_{i-1}[K_T] = \int_R \{[G]^T[_{i-1}S][G] + {_{i-1}}([B^*]^T[\mu]^{-1}[\alpha][B^*])\} \, dv \tag{5.4}$$

$$_{i-1}[K_{\mu\beta}] = \int_R {_{i-1}}([B^*]^T[\mu]^{-1}[\beta]\Psi([B^*])) \, dv \tag{5.5}$$

$$_{i-1}[K_\rho] = \int_R [N]^T {_{i-1}}([m_3][N] + [m_2]\Psi([N]) + [m_1]\gamma([N])) \, dv \tag{5.6}$$

$$_i\Delta F = \underset{\sim}{F} - \int_R {_{i-1}}\{[B^*]^T\underset{\sim}{S} + [N]^T([m_3][N] +$$

$$[m_2]\Psi([N]) + [m_1]\gamma([N]))\underset{\sim}{Y}\} \, dv \tag{5.7}$$

and

$$_i\underset{\sim}{H}_{\mu\alpha\beta} = \int_R [\mu]^{-1} {_i}\underset{\sim}{h}_{\mu\alpha\beta} dv \tag{5.8}$$

such that $[\mu]$, $[\alpha]$ and $\underset{\sim}{h}_{\mu\alpha\beta}$ are the assembled versions of $[\mu^{(r,m)}]$, $[\alpha^{(r,m)}]$ and $\underset{\sim}{h}^{(r,m)}_{\mu\alpha\beta}$.

Note, for rolling geometries which are symmetric, the various mechanical fields are periodic. Because of this, the computation of $_i\underset{\sim}{H}_{\mu\alpha\beta}$ is greatly simplified. Specifically, turning to the instantaneous local $(r,m,t+\Delta t)$

particle location, we see that due to periodicity, for the previous roll the $(r,m-J_r,t+\Delta t-J_r\Delta t)$ position possesses the same mechanical fields. In this context, it follows that

$$_{t+\Delta t}\underset{\sim}{S}{}^{(r,m)} = \underset{\sim}{S}(\underset{\sim}{\eta}_r + (m+kJ_r)\Delta\underset{\sim}{h}_r, t+\Delta t)$$

$$= \underset{\sim}{S}(\underset{\sim}{\eta}_r + (m-1+kJ_r)\Delta\underset{\sim}{\eta}_r, t+(1-J_r)\Delta t)$$

Hence, for the steady rolling case we have the following interrelationship between succeeding rolling states, that is

$$_{t+\Delta t}\underset{\sim}{S}{}^{(r,m)} = \underset{\sim}{S}(\underset{\sim}{\eta}_r + (m+kJ_r)\Delta\underset{\sim}{\eta}_r, t+\Delta t)$$

$$\underset{\sim}{S}{}^{(r,m)} = \underset{\sim}{S}(\underset{\sim}{\eta}_r + (m+kJ_r)\Delta\underset{\sim}{\eta}_r)$$

$$\underset{\sim}{S}{}^{(r,m)} = \underset{\sim}{S}(\underset{\sim}{\eta}_r + m\Delta\underset{\sim}{\eta}_r) \tag{5.9}$$

for all $m\varepsilon[1,J_r]$ and $k\varepsilon[0,\infty)$. Similarly,

$$\underset{\sim}{L}(\underset{\sim}{\eta}_r + (m+kJ_r)\Delta\underset{\sim}{\eta}_r) \equiv \underset{\sim}{L}(\underset{\sim}{\eta}_r + m\Delta\underset{\sim}{\eta}_r) \tag{5.10}$$

Based on the mechanical history defined by $\underset{\sim}{S}{}^{(r,m)}$ and $\underset{\sim}{L}{}^{(r,m)}$, (3.23) reduces to the more convenient form

$$\underset{\sim}{h}{}^{(r,m)}_{\mu\alpha\beta} \equiv \sum_\ell (\Delta t)^{-q_\ell} [\alpha^{(\ell)}] \sum_{j=1}^{J_r} C(q_\ell,j,m,r) \underset{\sim}{L}{}^{(r,j)} -$$

$$\sum_\ell (\Delta t)^{-p_\ell} [\mu^{(\ell)}] \sum_{j=1}^{J_r} C(p_\ell,j,m,r) \underset{\sim}{S}{}^{(r,j)} \tag{5.11}$$

where

$$C(q_\ell,j,m,J_r) = \sum_k (A(q_\ell,m+1-j + (\text{sgn }(j,m) + k)J_r) - (1-$$

$$\text{sgn }(j,m))A(q_\ell,m-j + \text{sgn }(j,m) + k)J_r) \tag{5.12}$$

$$C(p_\ell, j, m, J_r) = \sum_k (A(p_\ell, m+1-j + (sgn\ (j,m) + k)\ J_r) - (1 -$$

$$sgn\ (j,m))A)p_\ell, m-j + (sgn\ (j,m) + k)\ J_r)) \qquad (5.13)$$

The coefficient families $C(q_\ell, ...)$, $C(p_\ell, ...)$ represent the history effects on the $(r,m)^{th}$ particle. For instance, (5.12) defines the influence on the strain state of the succession of $k\varepsilon[1,\infty)$ rolls through the (r,j) orientation. Similarly, (5.13) defines the influence on the stress state of the succession of $k\varepsilon[1,\infty)$ rolls through the same orientation. As seen from (5.11), the net $(r,m)^{th}$ history is obtained by summing through all the $j\varepsilon[1,J_r]$ positional effects for all $k\varepsilon[0,\infty)$ rolls.

The algorithm defined by (5.3) yields the succession of $_i\Delta\underset{\sim}{Y}$ converging to the solution

$$\underset{\sim}{Y}_i = \underset{\sim}{Y}_{i-1} + {}_i\Delta\underset{\sim}{Y}\ ;\ i=1,2,3... \qquad (5.14)$$

To improve the robustness of the overall solution process, local constraints are introduced. Since rolling structures have a variety of substructural zones undergoing different levels of nonlinearity, $\Delta\underset{\sim}{Y}$ is controlled separately through the use of a partitioned constraint process. Namely, (5.3) is replaced by

$$_i\Delta\underset{\sim}{Y} = diag\ [\lambda_i]_{i-1}[K]^{-1}(\underset{\sim}{F} - {}_iH_{\mu\alpha\beta}) - {}_{i-1}[k]^{-1} \int_R {}_{i-1}([B^*]^T\underset{\sim}{S})dv \qquad (5.15)$$

where diag $[\lambda_i]$ is defined such that $_i\Delta\underset{\sim}{Y}$ is hierarchically controlled. In particular

$$diag\ [\lambda_i] = \begin{bmatrix} \lambda_{i1}[I_1] & & & \\ & \lambda_{i2}[I_2] & & 0 \\ & & \ddots & \\ & 0 & & \lambda_{iK}[I_K] \end{bmatrix} \qquad (5.16)$$

such that $\lambda_{i\ell}$, $\ell\epsilon[1,]$ are the various constraints and $[I_\ell]$; $\ell\epsilon[1,\kappa]$ a set of identity matrices whose individual sizes define the groups of degrees of freedom controlled by each given $\lambda_{i\ell}$. The choice of the $\lambda_{i\ell}$; $\ell\epsilon[1,\kappa]$ family is obtained by either:

i)   Requiring each of the various partitions of $_i\Delta\underset{\sim}{Y}$ to remain upper bounded by a specified linear constraint; or

ii) By employing a more general functional constraint say as in the hyperelliptic constraint surface of Padovan et al.[19,20].

Before establishing either of the foregoing schemes, all the various key vectors and matrices must be appropriately partitioned. In particular we let

$$_i\Delta\underset{\sim}{Y}^T = (_i\Delta\underset{\sim}{y}_1^T, \ _i\Delta\underset{\sim}{y}_2^T, \ \ldots, \ _i\Delta\underset{\sim}{y}_\kappa^T) \tag{5.17}$$

$$(_{i-1}[K]^{-1})^T = [_i[E_1], \ _i[E_2],\ldots,_i[E_\kappa]] \tag{5.18}$$

with

$$_i E_\ell] \equiv \ _{i-1}[[K_{T\ell}] + [K_{\mu\beta\ell}] + [\kappa_{\rho\ell}]] \tag{5.19}$$

such that the various partitions $_i\underset{\sim}{y}_\ell$ and $_i[E_\ell]$, $\ell\epsilon[1,\kappa]$ have respectively the same number of rows as the identity matrices $[I_\ell]$; $\ell\epsilon[1,\kappa]$. For simplicity, the driving potential $\underset{\sim}{F} - \ _i\underset{\sim}{H}_{\mu\alpha\beta}$ is recast as

$$_i\underset{\sim}{F} = \underset{\sim}{F} - \ _i\underset{\sim}{H}_{\mu\alpha\beta} \tag{5.20}$$

Hence, employing (5.17), (5.18), and (5.20), (5.3) reduces to

$$_i\Delta\underset{\sim}{y}_\ell = (\lambda_{i\ell})_i[E_\ell]_i\underset{\sim}{F} - \ _i[E_\ell]\!\int_{i-1}([B^*]^T\underset{\sim}{S})dv \ ; \ \ell\epsilon[1,\kappa] \tag{5.21}$$

Considering the elliptic constraint function approach[19], we introduce the localized version

$$\theta_\ell \, ||_i \underset{\sim}{y}_\ell||^2 + ||_i \underset{\sim}{f}_\ell||^2 = ||_o \Delta \underset{\sim}{F}||^2 \tag{5.22}$$

where $\ell \epsilon [1, \kappa]$ and

$$_i \underset{\sim}{y}_\ell = {}_{i-1} \underset{\sim}{y}_\ell + {}_i \Delta \underset{\sim}{y}_\ell \tag{5.23}$$

$$_i \underset{\sim}{f}_\ell = (\lambda_{i\ell})_i \underset{\sim}{F} \tag{5.24}$$

such that θ_ℓ defines the aspect ratio of the ellipse. Its choice will be discussed later. Solving (5.21) - (5.24) simultaneously, we yield a quadrative expression in $\lambda_{i\ell}$ namely

$$_i A_{\ell 1} (\lambda_{i\ell})^2 + {}_i A_{\ell 2} (\lambda_{i\ell}) + {}_i A_{\ell 3} = 0 \tag{5.25}$$

Since the coefficients $_i A_{\ell 1}, \dots$ are known scalars, $\lambda_{i\ell}$ can be directly evaluated from (5.25). Note, the roots chosen will be dependent on the state of definiteness of $[\kappa_{T\mu\beta\rho}]$.

The choice of the size of the $[I_\ell]$ partitions and their associated warping parameters θ_ℓ can either be user defined or automatically/self-adaptively generated. If user chosen, the size of the various partitions can be taken from a variety of factors namely

   i)   Inherent substructuring of a given system into component parts defined by

       • geometry
       • material groups
       • boundary conditions

   or

   ii) By geometry, material or boundary condition induced nonlinearity.

Such an approach also points to the appropriate choice of the local warps θ_ℓ. Note, the control of the size of allowable local field excursions

is obtained by requiring that they remain bounded by the family of elliptic constraints defined by (5.22 - 5.24).

For instance, from blueprint information clearances are often given for various substructural components. Such information can be used to determine upper bounds on a given ΔY_{ℓ} allowable. In terms of (5.22), such allowables would yield the following choice of θ_{ℓ} namely

$$\theta_{\ell} \leq ||_o \Delta F||^2 / ||Y_{\ell \text{ allowable}}||^2 \tag{5.26}$$

To self adaptively update such partitioning and warping, running checks can be made on:

i)   The normed partition level out of balance loads;

ii)   The level of strain energy stored/dissipated; or,

iii)   The normed excursions in the associated mechanical fields.

Once various combinations of i) - iii) are triggered, the appropriate partitions may be enlarged or shrunken along with associated changes in θ_{ℓ}. Noting the architecture of the constrained algorithm defined by (5.21) - (5.25), such partition and warping updates involve only straightforward accounting changes to define/locate a given partition.

V.2. Transient Problems

To handle transient problems, we shall adopt the implicit manner of formulation. In this context we recast (4.7) in so called incremental format, that is

$$\int_R \{[G]^T [S][G] + [B^*]^T \Delta S + [N]^T ([m_1][N]\Delta \ddot{Y} + [[m_2][N] + $$

$$2[m_1]\Psi([N])]\Delta Y + [[m_3][N] + [m_2]\Psi([N]) + [m_1]\gamma([N])]\Delta Y)\} \, dv = \Delta F \tag{5.27}$$

For the current purposes, the solution to (5.27) is obtained by employing the Newmark Beta method as defined by the following time stepping algorithm namely [1]

$$_{t+\Delta t}\ddot{\underline{Y}} = a_0 \Delta \underline{Y} - a_2 \, _t\dot{\underline{Y}} - a_3 \, _t\ddot{\underline{Y}} \tag{5.28}$$

$$_{t+\Delta t}\dot{\underline{Y}} = \, _t\dot{\underline{Y}} + a_0 \, _t\ddot{\underline{Y}} + a_7 \, _{t+\Delta t}\ddot{\underline{Y}} \tag{5.29}$$

$$
\begin{array}{llll}
a_0 = & 1/(\beta \Delta t^2) & a_4 = & \gamma/\beta - 1 \\
a_1 = & \gamma/(\beta \Delta t) & a_5 = & \Delta t/2(\gamma/\beta - 2) \\
a_2 = & 1/(\beta \Delta t) & a_6 = & \Delta t(1-\gamma) \\
a_3 = & 1/(2\beta) - 1 & a_7 = & \gamma \Delta t
\end{array}
\tag{5.30}
$$

Rearranging (5.28) and (5.29) into incremental form we obtain the expressions

$$\Delta \dot{\underline{Y}} = C_0 \Delta \underline{Y} + C_1 \, _t\dot{\underline{Y}} + C_2 \, _t\ddot{\underline{Y}} \tag{5.31}$$

$$\Delta \ddot{\underline{Y}} = C_3 \Delta \underline{Y} + C_4 \, _g\dot{\underline{Y}} + C_5 \, _t\ddot{\underline{Y}} \tag{5.32}$$

where

$$
\begin{array}{llll}
C_0 = & a_7 a_0 & C_3 = & a_0 \\
C_1 = & -a_7 a_2 & C_4 = & -a_2 \\
C_2 = & a_0 - a_7(a_1 - 1) & C_5 = & -(a_3 - 1)
\end{array}
\tag{5.33}
$$

Based on (5.31), (3.20) takes on the following form

$$\Delta \underline{S}^{(r,m)} = [\mu^{(r,m)}]^{-1}[[\alpha^{(r,m)}][B^{*(r,m)}] +$$

$$[\beta]\Psi([B^{*(r,m)}]) + C_0[\beta][B^{*(r,m)}]]\Delta \underline{Y}^{(r,m)} +$$

$$[\mu^{(r,m)}]^{-1} \, _{t+\Delta t}\underline{g}^{(r,m)}_{\mu\alpha\beta} \tag{5.34}$$

such that

$$_{t+\Delta t}\underset{\sim}{g}^{(r,m)}_{\mu\alpha\beta} =$$

$$_{t+\Delta t}\underset{\sim}{h}^{(r,m)}_{\mu\alpha\beta} + [\beta][B^{*(r,m)}] \{C_1 \ _t\underset{\sim}{\dot{Y}}^{(r,m-1)} + C_2 \ _t\underset{\sim}{\ddot{Y}}^{(r,m-1)}\} \qquad (5.35)$$

At this stage, employing (5.31), (5.32) and (5.35), it follows that at the fully assembled level (5.27) yields the following expression

$$_{t+\Delta t}[[K_T] + [K_{\mu\beta}] + [K_\rho]]\Delta Y = \ _{t+\Delta t}(\underset{\sim}{G}_{\mu\alpha\beta} + \Delta\underset{\sim}{F} + \underset{\sim}{I}_\rho) \qquad (5.36)$$

where here

$$_{t+\Delta t}G_{\mu\alpha\beta} \equiv \int_R \sum_{r,m} [\mu^{(r,m)}] \ _{t+\Delta t}\underset{\sim}{g}^{(r,m)}_{\mu\alpha\beta} \ dv \qquad (5.37)$$

$$_{t+\Delta t}\Delta\underset{\sim}{F} = \ _{t+\Delta t}\underset{\sim}{F} - \int_R [B^*]^T \underset{\sim}{S} \ dv \ \Big|_t \qquad (5.38)$$

$$_{t+\Delta t}[K_{\mu\beta}] = \int_R [B^*]^T[\mu]^{-1}[C_0[\beta][B^*] + [\beta]\Psi([B^*])] \ dv \qquad (5.39)$$

$$_{t+\Delta t}[K_\rho] = \int_R [N]^T[C_3[m_1][N] + C_0([m_2][N] +$$

$$2[m_2]\Psi([N])) + [m_3][N] + [m_2]\Psi([N]) + [m_1]\gamma([N])] \ dv \qquad (5.40)$$

and lastly

$$_{t+\Delta t}\underset{\sim}{I}_\rho = \int_R [N]^T \ \{[C_4[m_1][N] + C_1([m_2][N] +$$

$$2[m_1]\Psi([N]))]_t\underset{\sim}{\dot{Y}} + [C_5[m_1][N] +$$

$$C_2([m_2][N] + 2[m_1]\Psi([N]))]_t\underset{\sim}{\ddot{Y}}\} \ dv \qquad (5.41)$$

Solving (5.36) for $\underset{\sim}{Y}$ yields

$$\Delta\underset{\sim}{Y} = \ _{t+\Delta t}[K_D]^{-1} \ _{t+\Delta t}(\underset{\sim}{G}_{\mu\alpha\beta} + \Delta\underset{\sim}{F} + \underset{\sim}{I}_\rho) \qquad (5.42)$$

where the dynamic stiffness is given by the relation

$$_{t+\Delta t}[K_D] = {}_{t+\Delta t}[[K_T] + [K_{\mu\beta}] + [K_\rho]]$$ (5.43)

Based on (5.41), the time marching scheme defined yields the overall solution

$$_{t+\Delta t}\underset{\sim}{Y} = {}_{t}\underset{\sim}{Y} + \Delta\underset{\sim}{Y}$$ (5.44)

To improve the solution, (5.42) can be iterated in much the same manner as the steady case. Convergence for such a process is defined by the usual displacement norm check [20].

VI. Discussion

In the preceeding sections, a generalized nonlinear viscoelastic FE formulation was derived for translating and rotating structure. This included the development of both steady and transient solution algorithms. In the case of the steady formulation, a new locally constrained solution algorithm was created. For the transient case, an implicit algorithm involving the use of the Newmark Beta method [1] was developed. Note to enhance the capabilities of the overall formulation, the more comprehensive fractional operator [14-16] is used to represent the viscoelastic effects.

In parts II and III of this paper, the foregoing algorithms will be extensively benchmarked for both steady and transient situations. As noted earlier, this will include evaluating steady 3-D rolling contact simulations of pressurized tires. For the transient case rolling/translating over bumps and holes will be simulated. To enable such simulations, part II will include:

i) The development of 3-D rolling/translating elements handling nonlinear kinematics and material properties;

ii) The development of rolling/translating shell elements;

iii) The generalization of 3-D contact strategies to handle rolling contact; and,

iv) Comprehensive 3-D benchmarks with experimental verification.

In part III, the main thrust will be to:

i) Develop transient rolling contact schemes capable of handling impacts with obstructions;

ii) Develop the overall solution architecture integrating both the rolling/translating FE scheme with the transient contact scheme; and,

iii) To comprehensively benchmark the scheme.

Note the transient and steady translating/rolling FE simulations and associated solution algorithms have architectures essentially compatible with traditional formulations. Apart from the nonsymmetry induced in the static and dynamic stiffness, the changes required to incorporate such schemes in GP codes are minimal.

Acknowledgement

References

1. Bathe, K.J., <u>Finite Element Procedures in Engineering Analysis</u>, Prentice Hall, New Jersey, 1983.

2. Zienkiewicz, O.C., <u>The Finite Element Method</u>, McGraw Hill, New York, 1982.

3. Cook, R.D., <u>Concepts and Applications of Finite Element Analysis</u>, Wiley, New York, 1981.

4. Browne, A.L., Whicker, D., and Segalman, D.J., "A General Model for Power Loss in Pneumatic Tires", ASME AMD - Vol. 40, 1980.

5. Wildheim, J., "Excitation of Rotating Circumferentially Periodic Structures", Jr. of Sound and Vibration, 75, 397, 1981.

6. Padovan, J., "On Moving Thermal Contact Problems", AIAA Jr., 15, 1811, 1977.

7. Padovan, J., and Zeid, I., "On the Development of Traveling Load Finite Elements", Jr. of Computers and Structures, 12, 77, 1980.

8. Padovan, J. and Zeid, I., "Finite Element Modelling of Rolling Contact", Jr. Computers and Structures, 14, 163, 1981.

9. Padovan, J. and Tovichakchaikul, S., "Finite Element Analysis of Steadily Moving Contact Fields", Jr. of Computers and Structures, 18, 191, 1984.

10. Padovan, J. and Paramadilok, O., "Transient and Steady State Viscoelastic Rolling Contact", Jr. of Computers and Structures, 20, 545, 1985.

11. Brown, A.L., Whicker, D., and Segalman, D.J., "The Structure and Use of the GMR Combined Thermo-mechanical Tire Power Loss Model", SAE Paper No. 810164, 1981.

12. Clark, S.K., "Mechanics of Pneumatic Tires", U.S. DOT U.S. Printing Office, Washington DC, 1979.

13. Green, A.E. and Adkins, J.E., "Large Elastic Deformations and Non-linear Continuum Mechanics", Oxford - Clarendon Press, 1960.

14. Bagley, R.L. and Torvik, P.J., "Fractional Calculus - A Different Approach to the Analysis of Viscoelastically Damped Structures", AIAA Jr., 21, 741, 1983.

15. Bagley, R.L. and Torvik, P.J., "Fractional Calculus in the Transient Analysis of Viscoelastically Damped Structures", AIAA Jr., 23, 910, 1985.

16. Grunwald, A.K., "Veber, begrenzte", Derwationen und deren Anwendung", Z. Math Phys., 12, 441, 1867.

17. Fung, Y.C., Foundations of Solid Mechanics, Prentice Hall, New Jersey, 1965.

18. Abramowitz, M. and Stegun, I.A., Handbook of Mathematical Functions, Dover, New York, 1965.

19. Padovan, J., and Arechaga, T., "Formal Convergence Characteristics of Elliptically Constrained Incremental Newton Raphson Algorithm", Int. Jr. Engrg. Sci., 20, 1077, 1982.

20. Padovan, J., and Moscarello, R., "Locally Bound Constrained Newton Raphson Solution Algorithms", Jr. of Computers and Structures, (in press).

Appendix

In section II the governing field equations were developed. Here the so called moving total/updated Lagrangian coordinates were introduced. Assuming a cylindrical type coordinate system to define the geometry of rolling/translating structures, $\underset{\sim}{\eta}$ can be defined by the expression

$$\underset{\sim}{\eta} = \left\{ \begin{array}{l} r \cos (\theta + \phi(t)) \\ r \sin (\theta + \phi(t)) \\ x_e \end{array} \right\} \tag{A.1}$$

where here for constant rolling speeds about the x_3 axis

$$\phi(t) = \Omega t \tag{A.2}$$

Based on (A.1) and the fact that $u_i = u_i(\underset{\sim}{\eta}, t)$, we see that the first total derivative is given by

$$\frac{d}{dt}(u_i) = \frac{\partial u_i}{\partial t} + \frac{\partial}{\partial \eta_j}(u_i) \frac{\partial \eta_j}{\partial t} \tag{A.3}$$

where

$$\frac{\partial \eta_1}{\partial t} = -\Omega r \sin (\theta + \phi) \tag{A.4}$$

$$\frac{\partial \eta_2}{\partial t} = \Omega r \cos (\theta + \phi) \tag{A.5}$$

Combining (A.3) - (A.5) we see that

$$\frac{d}{dt}(u_i) = \frac{\partial}{\partial t}(u_i) + \Psi(u_i) \tag{A.6}$$

such that the $\Psi(\ )$ operator is defined by the expression

$$\Psi(\ ) = -\Omega r \sin (\theta + \phi) \frac{\partial}{\partial \eta_1}(\ ) + \Omega r \cos (\theta + \phi) \frac{\partial}{\partial \eta_2}(\ ) \tag{A.7}$$

Continuing, the second total derivative takes the form

$$\frac{d^2}{dt^2}(u_i) = \frac{\partial^2}{\partial t^2}(u_i) + 2\Psi\left(\frac{\partial}{\partial t}(u_i)\right) + \gamma(u_i) \tag{A.8}$$

where here

$$\gamma(\ ) = -\Omega^2 r \cos(\theta+\phi)\frac{\partial}{\partial \eta_1}(\ )-\Omega^2 r \sin(\theta+\phi)\frac{\partial}{\partial \eta_2}(\ ) +$$

$$\Omega^2 r^2 \sin^2(\theta+\phi)\frac{\partial^2}{\partial \eta_1^2}(\ ) + \Omega^2 r^2 \cos^2(\theta+\phi)\frac{\partial^2}{\partial \eta_2^2}(\ ) -$$

$$2\Omega^2 r^2 \sin(\theta+\phi)\cos(\theta+\phi)\frac{\partial^2}{\partial \eta_1 \partial \eta_2}(\ ) \tag{A.9}$$

For the special case of steady rolling, it follows that $u_i = u_i(\eta)$. In this context (A.6) and (A.8) reduce to the expressions

$$\frac{d}{dt}(u_i) = \Psi(u_i) \tag{A.10}$$

$$\frac{d^2}{dt^2}(u_i) = \gamma(u_i) \tag{A.11}$$

where here time appears implicitly through the definition of $\underset{\sim}{\eta}$. As can be seen through (A.10) and (A.11) the time derivative is replaced by a spatial one.

FINITE ELEMENT ANALYSIS OF STEADY

AND TRANSIENTLY MOVING/ROLLING

NONLINEAR VISCOELASTIC STRUCTURE:

PART 2: SHELL AND 3-D SIMULATIONS

Joe Padovan

Departments of Mechanical and Polymer Engineering

University of Akron

Akron, Ohio 44325

Abstract

In a three-part series of papers, a generalized finite element solution strategy is developed to handle traveling load problems in rolling, moving and rotating structure. The main thrust of this section consists of the development of 3-D and shell type moving elements. In conjunction with this work, a compatible 3-D contact strategy is also developed. Based on these modelling capabilities, extensive analytical and experimental benchmarking is presented. Such testing includes traveling loads in rotating structure as well as, low and high speed rolling contact involving standing wave type response behavior. These point to the excellent modelling capabilities of moving element strategies.

I. Introduction

This is the second paper in a series of three considering the development of large deformation viscoelastic FE formulations for steady and transient travelling/rolling/rotating structure. Overall, this part will give special emphasis to:

i)   The development of 3-D translating/rolling isoparametric type elements;

ii) The development of rolling/translating type shell elements;

iii) The creation of 3-D moving contact strategies, and

iv) The comprehensive 3-D simulation of a steadily rolling tire; here the analysis is correlated with experimentally derived tire test data to provide real world corroboration.

Since part one of this series has provided a fairly thorough review of previous work, for the sake of conciseness, we shall immediately get into the development. Note, the overall structure of the paper follows that defined by items i) - iv) noted earlier. Of particular importance is the benchmarking phase which involves both analytical comparisons, as well as, experimental test data. The empirical numerical correlations include:

i)   Standing contact;

ii) Frequency properties as per small deformation superposed on large and;

iii) Full rolling contact through all possible ranges of velocity.

1

2. Three Dimensional Formulation

Recalling Part 1 of this series, FE equations were derived for moving load problems involving:

i)   Transient inertial effects;

ii) Large deformation kinematics; and

iii) Viscoelastic properties.

Based on the use of a transient version of the Galilean transform [1-3], the following moving formulation was developed.

$$\int_R \{[B^*]^T \underset{\sim}{S} + [N]^T([m_1][N]\,\ddot{\underset{\sim}{Y}} + [[m_2][N] +$$

$$2[m_1]\,\Psi([N])]\,\dot{\underset{\sim}{Y}} + [[m_3][N] + [m_2]\,\Psi([N]) +$$

$$[m_1]\,\gamma([N])]\underset{\sim}{Y})\}dv = \underset{\sim}{F} \tag{2.1}$$

For the case of steady state motion, the use of the multiply constrained partitioned Newton Raphson scheme [3,4] yields the following solution algorithm namely

$$_i\Delta\underset{\sim}{Y} = \text{diag}\,[\lambda_i]\,_{i-1}[K]^{-1}(\underset{\sim}{F} - _iH_{\mu\alpha\beta}) -$$

$$_{i-1}[K]^{-1}\int_R\,_{i-1}([B^*]^T\underset{\sim}{S})dv \tag{2.2}$$

For this case, the consistent mass matrices are embedded within [K], that is

$$_{i-1}[K] = {}_{i-1}[[K_T] + [K_{\mu\beta}] + [K_\rho]] \tag{2.3}$$

where

$$_{i-1}[K_\rho] = \int_R [N]_{i-1}([m_3][N] + [m_2]\Psi([N]) + [m_1]\gamma([N]))dv \qquad (2.4)$$

To establish $_{i-1}[K_\rho]$ for 3-D formulations, we shall employ a 20 node isoparametric serendipity type brick element. Noting Fig. 2.1, it has three displacement degrees of freedom per node. The displacement fields in the 20 node solid element depend quadratically on the position within the element [5,6]. That is, the components of the shape function of this element have quadratic terms involving the isoparametric coordinates. Figure 2.2 shows the element in isoparametric space. The components of the shape function of this element are given in Table 2.1.

Noting the differential operators $\Psi(\ )$ and $\gamma(\ )$ given in (2.4), the shape functions must be differentiated spatially. Because isoparametric elements are used, the first step is to relate the derivatives with respect to the global Cartesian coordinates (x_1, x_2, x_3) to derivatives with respect to the elements isoparametric coordinates (ξ_1, ξ_2, ξ_3). This is necessary because the shape functions of isoparametric elements are written with respect to the ξ coordinates. By convention, these shape functions are used to relate the displacement fields in the element to the nodal displacements.

Noting (2.4), it is seen that expressions for

$$\left\{\frac{\partial u_i}{\partial(n_1, n_2, n_3)}\right\} = \left\{\begin{array}{c} \dfrac{\partial u_i}{\partial n_1} \\[2mm] \dfrac{\partial u_i}{\partial n_2} \\[2mm] \dfrac{\partial u_i}{\partial n_3} \end{array}\right\} \qquad , \qquad (2.5)$$

and

$$\left\{\frac{\partial^2 u_i}{\partial(n_1, n_2, n_3)^2}\right\} = \left\{\begin{array}{c} \dfrac{\partial^2 u_i}{\partial n_1^2} \\[12pt] \dfrac{\partial^2 u_i}{\partial n_2^2} \\[12pt] \dfrac{\partial^2 u_i}{\partial n_1 \partial n_3} \end{array}\right\} \qquad , \qquad (2.6)$$

must be found in terms of the nodal displacements. The forms used in (2.5) and (2.6) are shorthand for the full number of first and second derivatives, namely

$$(\partial u_i / \partial n_j, \; \partial^2 u_i / \partial n_i \partial n_j); \; (i,j)\epsilon[1,3].$$

The first derivatives are related by

$$\left\{\frac{\partial u_i}{\partial(\xi_1, \xi_2, \xi_3)}\right\} = [J] \left\{\frac{\partial u_i}{\partial(n_1, n_2, n_3)}\right\} \qquad (2.7)$$

where [J] is the Jacobian matrix given by

$$[J] = [\frac{\partial n_i}{\partial \xi_j}] \; \{ \begin{array}{l} i \text{ - row} \\ j \text{ - column} \end{array} \qquad (2.8)$$

This expression can be inverted to give the relationship between the Cartesian and isoparametric spaces needed for the first derivatives, that is

$$\left\{\frac{\partial u_i}{\partial(n_1, n_2, n_3)}\right\} = [J]^{-1} \left\{\frac{\partial u_i}{\partial(\xi_1, \xi_2, \xi_3)}\right\} \qquad (2.9)$$

To establish the requisite second derivatives, the chain rule is applied twice. In the context of the $\partial(\ )/\xi_1$ and $\partial^2(\ )/\partial\xi_1^2$ derivatives, such an operation yields

$$\frac{\partial u_i}{\partial \xi_j} = \sum_{\ell=1}^{3} \frac{\partial u_i}{\partial n_\ell} \frac{\partial n_\ell}{\partial \xi_j} \qquad (2.10)$$

and

$$\frac{\partial^2 u_i}{\partial \xi_j^2} = \sum_{\ell=1}^{3} \frac{\partial}{\partial \xi_j} \left(\frac{\partial u_i}{\partial n_\ell} \frac{\partial n_\ell}{\partial \xi_j} \right) \qquad , \qquad (2.11)$$

which upon expansion and combination of like terms reduces to

$$\frac{\partial^2 u_i}{\partial \xi_j^2} = \sum_{\ell=1}^{3} \left\{ \frac{\partial^2 u_i}{\partial n_\ell^2} \left(\frac{\partial n_\ell}{\partial \xi_j} \right)^2 + \frac{\partial u_i}{\partial n_\ell} \frac{\partial^2 n_\ell}{\partial \xi_j^2} \right\} + 2 \frac{\partial^2 u_i}{\partial n_1 \partial n_2} \frac{\partial n_1}{\partial \xi_j} \frac{\partial n_2}{\partial \xi_j} +$$

$$2 \frac{\partial^2 u_i}{\partial n_1 \partial n_3} \frac{\partial n_1}{\partial \xi_j} \frac{\partial n_2}{\partial \xi_j} + 2 \frac{\partial^2 u_i}{\partial n_2 \partial n_3} \frac{\partial n_2}{\partial \xi_j} \frac{\partial n_3}{\partial \xi_j} \qquad (2.12)$$

Repeating this process for the remaining second derivatives, we obtain the following overall operator expression namely

$$\left\{ \frac{\partial^2 u_i}{\partial(\xi_1,\xi_2,\xi_3)^2} \right\} = [J_1] \left\{ \frac{\partial^2 u_i}{\partial(n_1,n_2,n_3)^2} \right\} + [J_2] \left\{ \frac{\partial u_i}{\partial(n_1,n_2,n_3)} \right\} \qquad (2.13)$$

The matrix $[J_1]$ is (6x6) and $[J_2]$ is (6x3). Now, based on (2.9), (2.13) can be inverted to yield

$$\left\{ \frac{\partial^2 u_i}{\partial(n_1,n_2,n_3)^2} \right\} = [J_1]^{-1} \left\{ \frac{\partial^2 u_i}{\partial(\xi_1,\xi_2,\xi_3)^2} \right\} - [J_3] \left\{ \frac{\partial u_i}{\partial(\xi_1,\xi_2,\xi_3)} \right\} \qquad (2.14)$$

where

$$[J_3] = [J_1]^{-1} [J_2] [J]^{-1} \tag{2.15}$$

The first and second derivatives on the right side of (2.14) are with respect to the element's isoparametric coordinates. The shape function and hence the displacement fields are described using this coordinate system. Recalling Part 1, the displacement field in the element is related to the nodal degrees of freedom by

$$\underset{\sim}{u} = [N]\underset{\sim}{Y} \tag{2.16}$$

For the u_i components, (2.16) yields that

$$u_i = {}_i\underset{\sim}{N}^T \underset{\sim}{Y} \tag{2.17}$$

where ${}_i\underset{\sim}{N}^T$; $i = 1, 2, 3$ denote the three rows of $[N]$.

In (2.17), since $\underset{\sim}{Y}$ are not spatially dependent, we see that

$$\{\frac{\partial u_i}{\partial(\xi_1,\xi_2,\xi_3)}\} = [\frac{\partial}{\partial(\xi_1,\xi_2,\xi_3)}({}_i\underset{\sim}{N}^T)]\underset{\sim}{Y} \tag{2.18}$$

$$\{\frac{\partial^2 u_i}{\partial(\xi_1,\xi_2,\xi_3)^2}\} = [\frac{\partial^2}{\partial(\xi_1,\xi_2,\xi_3)^2}({}_i\underset{\sim}{N}^T)]\underset{\sim}{Y} \tag{2.19}$$

where here

$$[\frac{\partial}{\partial(\xi_1,\xi_2,\xi_3)}({}_i\underset{\sim}{N}^T)] = \begin{bmatrix} \frac{\partial}{\partial\xi_1}({}_i\underset{\sim}{N}^T) \\[2ex] \frac{\partial}{\partial\xi_2}({}_i\underset{\sim}{N}^T) \\[2ex] \frac{\partial}{\partial\xi_3}({}_i\underset{\sim}{N}^T) \end{bmatrix} \tag{2.20}$$

and

$$[\frac{\partial^2}{\partial(\xi_1,\xi_2,\xi_3)^2}(_iN^T)] = \begin{Bmatrix} \frac{\partial^2}{\partial\xi_1^2}(_iN^T) \\ \\ \frac{\partial^2}{\partial\xi_2^2}(_iN^T) \\ \vdots \\ \frac{\partial^2}{\partial\xi_1\partial\xi_3}(_iN^T) \end{Bmatrix} \qquad (2.21)$$

The details of the differentiation of the actual components of [N] is given in Tables (2.2) - (2.4). Here $\frac{\partial}{\partial\xi_1}(\ )$, $\frac{\partial^2}{\partial\xi_1^2}(\ )$ and $\frac{\partial^2}{\partial\xi_1\partial\xi_2}(\ )$ are depicted. Based on these expressions, the various other derivative expressions can be generated.

In the context of the foregoing nomenclature, the following expression can be generated for $\partial u_i/\partial(n_1,n_2,\ n_3)$ namely

$$\{\frac{\partial u_i}{\partial(n_1,n_2,n_3)}\} = [J]^{-1} [\frac{\partial}{\partial(\xi_1,\xi_2,\xi_3)}(_iN^T)]\underline{Y} \qquad (2.22)$$

where $i\epsilon[1,3]$. In a similar manner, (2.14), (2.20) and (2.21) yield the relation

$$\{\frac{\partial^2u_i}{\partial(n_1,n_2n_3)}\} =$$

$$[J_1]^{-1} [\frac{\partial^2}{\partial(\xi_1,\xi_2,\xi_3)^2}(_iN^T)]\underline{Y} - [J_3] [\frac{\partial}{\partial(\xi_1,\xi_2,\xi_3)}(_iN^T)]\underline{Y} \qquad (2.23)$$

For transient situations, Part I derived the following FE formulation namely

$$\int_R \{[G]^T[S][G] + [B^*]^T \Delta\underline{S} + [N]^T([m_1][N]\Delta\underline{\ddot{Y}} + [[m_2][N] +$$

$$2[m_1]\Psi([N])]\underline{\dot{Y}} + [[m_3][N] + [m_2]\Psi([N]) +$$

$$[m_1]\gamma([N])]\Delta\underline{Y})\}dv = \Delta\underline{F} \qquad (2.24)$$

Upon use of the Newmark Beta type integration method, (2.24) was seen to reduce to the following more tractable form, that is

$$_{t+\Delta t}[[K_T] + [K_{\mu\beta}] + [K_\rho]]\Delta\underline{Y} = {}_{t+\Delta t}(\underline{G}_{\mu\alpha\beta} + \Delta\underline{F} + I_\rho) \qquad (2.25)$$

where here

$$_{t+\Delta t}[K_\rho] =$$

$$\int_R [N]^T[C_3[m_1][N] + c_o([m_2][N] +$$

$$2[m_2]\Psi([N])) + [m_3][N] + [m_2]\Psi([N]) + [m_1]\gamma([N])]dv \qquad (2.26)$$

As can be seen again, consistent mass terms are embedded in (2.25) which involve the $\Psi(\ )$ and $\gamma(\ )$ differential operators. These can be treated through the use of (2.22) and (2.23) wherein the various derivatives of the components of [N] can be obtained/generated from Tables 2.1-2.4.

3. Thick Shell Element Formulation

Certain engineered structures have the property that their normal strain components in the thickness direction are negligible in comparison to the in-plane values. In these cases, the structure can be modelled as a shell. For such situations, enhanced computational savings are obtained since the normal components in the thickness direction are entirely neglected.

To allow for this modelling feature in steady and transient moving load problems, an eight node isoparametric shell element is developed. It is obtained by degenerating a three dimensional solid element [5,6]. A typical shell element and its associated nodes is shown in Fig. 3.1.

To start the development, it is noted that the in-plane shape function components are the same as those for the (ξ_1, ξ_2) plane $(\xi_3 \equiv 0)$ in the solid element. The relative in-plane displacements between the top and bottom surfaces of the solid element are handled by rotational degrees of freedom and the thickness. These rotational degrees of freedom are with respect to the local axes, as shown in Fig. 3.2. The element has three displacement and two rotational degrees of freedom at each node.

The displacement field in the element, for the ith global direction is expressed as

$$u_i = \sum_{k=1}^{8} N_k(\xi_1, \xi_2) u_i^k + \frac{\xi_3}{2} N_k(\xi_1, \xi_2) h_k (-v_{2i}^k \theta_1^k + v_{1i}^k \theta_2^k) \qquad (3.1)$$

where u_i^k is the displacement of node k in the ith direction, h_k is the thickness at the given node, (v_{1i}^k, v_{2i}^k) are components of the local vector in the (1,2) directions and lastly (θ_1^k, θ_2^k) are the rotational degrees of freedom about the local (1,2) axes at the kth node. The derivatives with respect to the in-plane variables ξ_1 and ξ_2 of (3.1) will be of the same form, except that the shape function is replaced by the appropriate derivative. For example, the displacement derivative with respect to ξ_1 is

$$\frac{\partial u_i}{\partial \xi_1} = \sum_{k=1}^{8} \left(\frac{\partial N_k(\xi_1, \xi_2)}{\partial \xi_1} u_i^k + \frac{\xi_3}{2} \frac{\partial N_k(\xi_1, \xi_2)}{\partial \xi_1} h_k (-v_{2i}^k \theta_1^k + v_{1i}^k \theta_2^k) \right) \qquad (3.2)$$

Similar expressions can be derived for the remaining first and second derivatives. Note, the values of the requisite components of the shape function and their associated derivatives can be found using Tables (2.1) - (2.4) by setting ξ_3 to zero.

The first derivative of the displacement components with respect to the out of plane coordinate ξ_3 is given by

$$\frac{\partial u_i}{\partial \xi_3} = \sum_{k=1}^{8} \frac{1}{2} N_k(\xi_1, \xi_2) h_k (-v_{2i}^k \theta_1^k + v_{1i}^k \theta_2^k) \tag{3.3}$$

The second derivative namely $\partial^2 u_i / \partial \xi_3^2$ is zero. Continuing, the second derivatives with respect to (ξ_1, ξ_3) and (ξ_2, ξ_3) are a combination of (3.2) and (3.3). The forms of (3.2) and (3.3) and the appropriate values of the shape functions and their derivatives are used to give the quantities needed to define the transformed inertia matrices.

The calculation of the transformed mass matrix using the formulation just described requires extensive numerical integration. Obviously, it would be preferred from a computational point of view to have a closed form expression for the transformed mass matrix. This is possible for the special case of rotation about a single axis.

As a simplification of the formulation, considering body of revolution coordinates, the inertia in the circumferential and radial directions can be handled by the consistent approach [7], while the meridional direction inertia is handled by the lumped approach [7]. This is chosen because the inertia due to rotation lies in the circumferential - radial plane. Also, this way of expressing the problem will simplify the formulation and allow for closed form integration of the transformed mass matrix. Shape functions

for the consistent part of the formulation are written with respect to the

element's local coordinate system rather than the isoparametric system.

This puts a restriction on the shape and orientation of the element - its

sides must lie in the circumferential, meridional, and radial directions.

This is really not a restriction in body of revolution analyses since such

an approach is the easiest way to build the finite element grid on a specific

geometry.

Overall, the foregoing simplifications can be implemented in several

steps namely:

i)   Circumferential direction treated consistently;

ii) Radial and meridional directions treated in lumped

     parameter format.

Based on such an approach, the calculation of the matrix involves a

quadratic variation in displacement in the circumferential direction

specifically

$$u \propto a + bn + cn^2 \tag{3.4}$$

such that n is the circumferential coordinate. Note these proportionalities

are assumed for the inertia calculations only. The displacement fields used

for the stiffness matrix calculation remain as orginally defined.

Using the known circumferential positions of the nodes, as shown for one

circumferential line of nodes in Figure 3.2, the values of the coefficients

in equation (3.4) are determined. These are then used to give shape functions

and derivatives of the shape functions for these nodes. Each circumferential

line of nodes in the element is defined as a zone, as shown in Figure 3.3.

The center zone has only end nodes in the shell element, but a pseudo-node is defined at the element center so that the same formulation can be used for this zone. Each zone is given a weighting value due to the lumped formulation being used in the meridional direction.

The mass terms for the center node of the middle zone, the pseudo-node, must be condensed out because it is not present in the stiffness matrix calculations, and hence has no degrees of freedom in the global equations. This can be done in the usual manner on the element level, before the element mass matrix is assembled into the global mass matrix. This method of calculating the transformed mass matrix should be computationally more efficient because numerical integration is not needed.

4. Three Dimensional Pantographing Gap Element Strategy

There are several different ways to handle the problem of contact. These include:

i) Direct application by continuous modification of boundary conditions [8];

ii) Hughes type auxiliary matrices [9];

iii) Penalty methods [10];

iv) Influence coefficients [11] and;

v) Gap type procedures [12,15].

Each of these schemes have various advantages and disadvantages. Perhaps the single most often occurring problem involves the fact that some form of stiffness update and inversion is typically required during the overall solution process.

To reduce computational effort, use is made here of substructuring

concepts. Specifically, the global incremental stiffness formulation is recast in the form

$$
\begin{bmatrix} [K_I] & [K_{IC}] \\ [K_{CI}] & [K_C] \end{bmatrix} \begin{Bmatrix} \Delta \underline{Y}_I \\ \Delta \underline{Y}_C \end{Bmatrix} = \begin{Bmatrix} \Delta \underline{F}_I \\ \Delta \underline{F}_C \end{Bmatrix} \tag{4.1}
$$

such that I, C, ($\Delta\underline{Y}_I$, $\Delta\underline{Y}_C$), ($\Delta\underline{F}_I$, $\Delta\underline{F}_C$) and ([K_I],...,[K_C]) respectively define the subscripts associated with internal and contact degrees of freedom, the incremental deflection fields, the incremental nodal forces and lastly the various partitions of the tangential stiffness matrix. Solving for the incremental internal and contact degrees of freedom, we yield the following substructural expressions namely

$$
\Delta\underline{Y}_C = [[K_C] - [K_{CI}][K_I]^{-1}[K_{IC}]]\Delta\underline{F}_C - [K_{CI}][K_I]^{-1}\Delta\underline{F}_I \tag{4.2}
$$

and

$$
\Delta\underline{Y}_I = -[K_I]^{-1}[K_{IC}]\Delta\underline{Y}_C + [K_I]^{-1}\Delta\underline{F}_I \tag{4.3}
$$

To streamline the computational effort, [K_I] is updated only at the beginning of a given load step. During successive iterations, [K_{IC}], [K_{CI}] and [K_C] are intermittently updated depending on the type of contact procedure employed. In this context, (4.2) and (4.3) can be recast in the following algorithmic form namely

$$
_i\Delta\underline{Y}_C = [_{i-1}[K_C] - {}_{i-1}[K_{CI}] \, _o[K_I]^{-1} \, _{i-1}[K_{IC}]]_i\Delta\underline{F}_C -
$$

$$
_{i-1}[K_{CI}] \, _o[K_I]^{-1} \, _{i-1}\Delta\underline{F}_I \tag{4.4}
$$

$$
_i\Delta\underline{Y}_I = {}_o[K_I]^{-1} \, _{i-1}[K_{IC}] \, _i\Delta\underline{Y}_C + {}_o[K_I]^{-1} \, _{i-1}\Delta\underline{F}_I
$$

where the sub $_i(\ )$ denotes the ith iteration of the given load step and sub-zero the initial value.

To enable the more controlled handling of contact problems, local constraints can be imposed on the individual degrees of freedom associated with $\Delta \underline{Y}_I$ and $\Delta \underline{Y}_C$. Recalling Part 1 of the paper, the nonlinear FE formulation can be solved via a multiply constrained partitioned NR solver. In terms of the substructuring noted in (4.1), the constraint process is applied directly to successive deflection excursions. Specifically, $\Delta \underline{Y}$ is replaced by $[diag(\lambda)]\Delta \underline{Y}$ and hence (4.1) takes the form

$$\begin{bmatrix} [K_I] & [K_{IC}] \\ [K_{CI}] & [K_C] \end{bmatrix} [diag(\lambda)] \left\{ \begin{array}{c} \Delta \underline{Y}_I \\ \Delta \underline{Y}_C \end{array} \right\} = \left\{ \begin{array}{c} \Delta \underline{F}_I \\ \Delta \underline{F}_C \end{array} \right\} \qquad (4.5)$$

where

$$[diag(\lambda)] = \begin{bmatrix} [diag(\lambda_I)] & [0] \\ [0] & [diag(\lambda_C)] \end{bmatrix} \qquad (4.6)$$

such that $[diag(\lambda_I)]$ and $[diag(\lambda_C)]$ respectively denote diagonal matrices defining individual constraints on the internal and contact degrees of freedom. Based on the form of (4.5), it follows that

$$[diag(_i\lambda_C)]_i\Delta \underline{Y}_C =$$

$$[_{i-1}[K_C] - _{i-1}[K_{CI}] \ _0[K_I]^{-1} \ _{i-1}[K_{IC}]]_i\Delta \underline{F}_C -$$

$$_{i-1}[K_{CI}] \ _0[K_I]^{-1} \ _{i-1}\Delta \underline{F}_I \qquad (4.7)$$

and

$$[diag(_i\lambda_I)]_i\Delta\underline{Y}_I =$$

$$_o[K_I]^{-1} {}_{i-1}[K_{IC}][diag(_i\lambda_C)]_i\Delta\underline{Y}_C + {}_o[K_I]^{-1} {}_{i-1}\Delta\underline{F}_I \qquad (4.8)$$

Note, each of the individual constraints appearing in $[diag(_i\lambda_C)]$ and $[diag(_i\lambda_I)]$ can be defined by either:

i) Establishing upper bounds on the deflections [3] of each particular substructural partition of $[K_I]$ and $[K_C]$ or;

ii) Employ a constraint function to bound allowable excursions [14].

For the problem of contact, it is preferable to employ i) wherein upperbound allowable excursions for the various partitions of $\Delta\underline{Y}_C$ can be continuously reset by monitoring the gap between contact surfaces. The various partitions of $\Delta\underline{Y}_I$ can be controlled in the manner defined by ii), namely by locally defined constraint functions [4].

Since a very large scale rolling simulation will be considered in this paper, to avoid the potential instabilities of the penalty method and inefficiencies of the Hughes scheme, the pantographing gap methodology of Padovan and Moscarello [13] is employed. Noting Figs. 4.1, 4.2, and 4.3, pantographing enables the gap element to avoid severe distortion which occurs if ground nodes are constrained. Additionally, the gap element is subdivided into several zones associated with the level of integration employed. Specifically, as can be seen from Fig. 4.4, since 3-3-3 integration is employed for the 20 node element, 9 separate zones are defined in the

contact area. These zones are alternatively turned on and off by the appropriate proximity criteria [13]. In much the way as elastic plastic formulations [15].

Noting Fig. 4.3, the element is continuously pantographed until a given node is found to satisfy the requisite proximity/contact criteria [13]. At this point, the zone associated with the given node is handled via an updated Lagrangian observer referencing the frozen pantographed portion of the node. If the node is found to release, then pantographing is resumed such that the prehistory is erased.

The stiffness of the gap has essentially three phases of operation namely:

   i)   Completely noncontacted wherein the stiffness is very small;

   ii)   Partially or fully contacted wherein no slip is allowed and;

   iii) Partially or fully contacted wherein frictional slips is allowed.

In the uncontacted mode, the gap element stiffness returned for assembly in the global matrix is numerical very small. For the partially or fully contacted mode wherein no slip is allowed, the appropriate zonal or whole element stiffness is made stiffer than the neighboring element. Lastly, for the case where frictional slip is allowed, the material stiffness of the gap is replaced by an adjusted orthotropic version of that of the neighboring structural element. Specifically:

   i)   The direction normal to the contact surface is made very stiff (an order of magnitude larger than the neighboring element);

ii)   The Poisson effect terms linking the normal and

      tangential behavior are deleted;

iii) Tangential direction to contact is reset so as to have

      the same stiffness properties as neighboring element and;

iv)   Tangential contact nodal deflections are released and

      replaced by appropriate friction forces.

Note, the criteria defining contact and slip-stick behavior are given by the following expressions namely:

i)   Contact conditions;

$$(Y^e_{CN\ell} - Y^e_{\ell Crit}) - \delta \begin{cases} >0, \text{ no contact} \\ <0 \text{ contact} \end{cases} \tag{4.14}$$

$$F^e_{N\ell} \begin{cases} >0 \text{ no contact} \\ <0 \text{ contact} \end{cases} \tag{4.15}$$

ii)   Slip/stick conditions;

$$(F^e_{\tau\ell} - F_{Crit}) \begin{cases} >0 \text{ slip} \\ \leq 0 \text{ stick} \end{cases} \tag{4.16}$$

where here ℓ defines the contact nodes of the eth element, and $Y^e_{CN\ell}$, $Y^e_{\ell Crit}$, δ, $F^e_{N\ell}$, $F^e_{\tau\ell}$ and F_{Crit} respectively represent the normal deflection, contact gap distance of given node, error tolerance, normal force, tangential force and the slip force threshold.

From an operational point of view, the slip mode will require the gap

stiffness to be restructured. In particular, given the eth gap element expression, after partitioning we have that

$$\left\{ \begin{array}{c} F_g^e \\ F_\tau^e \end{array} \right\} = \left[\begin{array}{cc} [K_g^e] & [K_{g\tau}^e] \\ [K_{\tau g}^e] & [K_\tau^e] \end{array} \right] \left\{ \begin{array}{c} Y_g^e \\ Y_\tau^e \end{array} \right\} \tag{4.9}$$

where noting Fig. 4.4, the sub τ denotes slipping tangential degrees of freedom at the contact nodes, while g defines the remaining field variables. Based on (4.9), the slip condition can be defined by the following substructural representation namely

$$F_g^e = [[K_g^e] - [K_{g\tau}^e][K_\tau^e]^{-1}[k_{\tau g}^e]]Y_g^e + [K_{g\tau}^e][K_\tau^e]^{-1}F_\tau \tag{4.10}$$

$$Y_\tau^e = -[K_\tau^e]^{-1}[K_{\tau g}^e]Y_g + [K_\tau^e]^{-1}F_\tau^e \tag{4.11}$$

Depending on the number of element zones involved in frictional slipping, then

$$F^e = f^e(F_N^e) \tag{4.12}$$

where here F_N^e denotes the normal forces at contact nodes and f^e the appropriately zonalized function defining the slip friction. In the classic case of Coulomb friction, the generalized function $f^e(F_N^e)$ is replaced by

$$F_\tau^e = [\mu^e] \, F_N^e \tag{4.13}$$

such that $[\mu^e]$ is properly structured so as to define the various zones of the element which are slipping.

As a final note, it follows that due to the use of moving coordinates, no special change needs to be implemented in the pantographing gap strategy. In particular it applies to both standing and rolling situations involving both steady and transient simulations.

5. Benchmarking

To benchmark the foregoing rolling 3-D shell and contact schemes, several comprehensive simulations will be considered. Overall, these include:

    i)   2-D evaluation to determine operational characteristics;

    ii)   Purely shell type 3-D model to evaluate mesh spacing requirements;

    iii) Mixed shell and 3-D element simulation of rolling tire.

To enable such testing, the various formulations developed in sections 2-4 were encoded in the NONSAP derivative code NFAP. The only major modification needed to convert the code involved the extension of the blocked skylined out of core solver [17] to handle the nonsymmetric matrices arising from the rolling/moving formulation. Beyond this, only standard modifications were introduced into the shell and 3-D (20 node) element libraries.

    Note, the main thrust of the benchmarking will be to:

    i)   Correlate current modelling scheme with previous results and;

    ii)   Compare results with experimental tests.

These comparisons will consider several aspects of system behavior, namely:

i)   Determine capabilities of rolling shell and 3-D

     elements to capture proper small deformation

     superposed on large eigenvalue properties and

     associated mode shapes;

ii) Establish capabilities of gap contact scheme and;

iii) Establish capabilities to handle overall interplay

     between geometric/material nonlinearity and inertia

     effects.

As a first test, we consider the dynamic response of the 2-D ring on

elastic foundation model of the tire [17]. Noting the model defined in

Fig. 5.1, Figs. 5.2 and 5.3 illustrate the mixed shell/3-D and purely 3-D

simulations. To evaluate and compare the dynamic characteristics of the

shell and 3-D elements, we shall consider the problem of a circumferential

traveling radial load, Fig. 5-4. Recalling the analytical solution developed

by Padovan [18], when the circumferential traveling speed of the radial load

is matched with the ratio of an individual frequency ω_M and its mode number

M, namely ω_M/M, a resonance type response is excited. For instance, con-

sidering the 11th mode depicted in Fig. 5.5, the shell and 3-D models yielded

critical speeds of 119.7 mph and 120.3 mph respectively. Similar levels of

accuracy were noted for all the critical speeds/natural frequencies ranging

from the minimum to those above 180 mph (namely the first 25 frequencies).

As a next test, we shall consider the problem of viscoelastic rolling contact.

Figure 5.6 illustrates the gap element supported model. Based on this simu-

lation, Fig. 5.7 depicts the rolling contact shape and associated normal pres-

sure distribution in the contact zone. Both the shell and 3-D simulations

yielded essentially the same results for all reasonable ranges of rolling speed.

The next model considered consists of simulating a two layer pressurized torus whose overall geometry and material properties are depicted in Fig. 5.8. As with the ring model, the pressurized torus is subject to a circumferentially traveling radial load. Figure 5.9 illustrates the changes in crown mode shape as a critical speed is approached and passed. The overall resonance mode shape is given in Fig. 5.10. These results were correlated with frequencies defined by the classic eigenvalue type formulation of the problem using a highly refined model. This comparison enabled the calibration of the appropriate element sizing. For instance, it was found that for the given shell element type;

i)   Element arcs that subtended greater than 1/36 of the
       circumference tended to yield slow convergence and;

ii)   In the meriodional/cross sectional orientation, at
       least 18 elements were needed to yield adequate model
       resolution.

With such element spacings, all frequencies in the range of engineering interest showed at most 3% deviations between the traveling and classic eigenvalue formulations. Such sensitivity studies enabled the reduction of the overall size of the tire model which even so is quite extensive.

As the culminating benchmark, Fig. 5.11 illustrates the 15,000 degree of freedom model of a tire. Overall, the model treated the various internal laminations via Halpin Tsai [19] type correlations. The reason for the level of both meridional and circumferential refinement follows from the torus tests. These revealed that fairly uniform circumferential element spacing is needed

to define the proper mode shape/dynamic characteristics.

The first test applied to the model consisted of pressurization and subsequent loading into ground contact. Figure 5.12 illustrates the gap element model used to define the contact region. Based on this model, the pressurization and subsequent loading into ground contact defined the axle load deflection curve denoted in Fig. 5.13. As can be seen, the model correlated quite well with experimental data obtained from the Firestone Tire and Rubber Company. The actual deflected shape of the contact region of the model is shown in Fig. 5.14.

Next, we shall consider the models' capability to capture the frequency characteristics of the tire. Again, noting Fig. 5.15, this is achieved by placing a circumferentially travelling radial load on the crown section. Figures 5.15-5.21 illustrate various aspects of the dynamics. Note, as we are strictly interested in defining inertia capturing capabilities, damping was deleted from this series of tests.

For velocities lower than 90 mph, little inertial effects were excited by pure rolling. As an example of this, Fig. 5.15 illustrates the tire response at 90 mph. Under modest increases above 90 mph, resonances were noted. For instance, Fig. 5.16 illustrates the crown node response to the approach and passing of a resonance speed. As can be seen, the range of speed is quite tight. The amplitude behavior during the resonance passing process is denoted in Fig. 5.17. Note, without damping, the resonance response is unbounded. At the critical speed (peak amplitude) associated with the given mode, Figs. 5.18 and 5.19 illustrate the crown and overall tire behavior. These results were within 1% error of the experimentally generated data. With further increases in speed, other modes were excited. Figures 5.20 and 5.21 illustrate the crown and whole tire response behavior at 138 mph.

It is interesting to note that the first critical speed of a rolling structure prototypically involves higher order modes. As the speed is gradually raised from the first critical, both lower and higher order modes may be excited. This is clearly seen by comparing Figs. 5.19 and 5.21 which illustrate the 8th (117 mph) and 6th (138 mph) modal responses.

Such behavior is a direct outgrowth of the fact that the critical modes are directly related to ω_M/M. Noting Fig. 5.22, we see that usually ω_M is monotone increasing in M. Based on this, ω_M/M prototypically is nonmonotone for small M. Figure 5.23 illustrates such behavior. The dip in the curve illustrated, points to the fact that higher order modes can give rise to the first critical. As the speed is increased, noting the trends depicted in Fig. 5.23, various lower and higher resonces are subsequently excited. Additionally, depending on the inherent curvature of the ω_M versus M behavior of the structure, the critical velocities can either be tightly or loosely packed. Such trends are depicted in Fig. 5.24.

When damping is introduced, the individual modes tend to merge into a single so-called standing wave which appears behind the contact region and attenuates in the circumferential direction [3]. This behavior is clearly seen in Fig. 5.7. As the speed is gradually increased, the wave length tends to elongate. Such behavior is an outgrowth of the dissipation of higher order modes.

As the last benchmark problem, we shall consider the steady freely rolling tire. Since the upper bound behavior of rolling tires is the so-called standing wave problem, main emphasis will be given to model this form of dynamic response. Figure (5.25) illustrates the standing wave response developed on a road wheel type test rig. As can be seen, extremely large deformation cha-

racteristics are excited. Employing the model depicted in Fig. 5.11, the rolling behavior is obtained in several steps namely:

    i)   Pressurize tire structure accounting for follower type forces;

    ii)   Push rolling tire into contact by varying hub deflection incrementally or alternatively;

    iii)   Push non-rolling tire into contact by varying the hub deflection; once converged, rolling velocity is incrementally increased.

To evaluate the importance of friction to the global effects, both pure slip and stick conditions were considered. While this induced different very localized shear distributions in the tread area of the contact patch, no changes were recorded in the global dynamic resonse. In this context, a stick condition was employed for the freely rolling full scale model. This significantly reduces run times.

Based on the foregoing, Figs. 5.26-5.29 illustrate the response under different ranges of viscoelasticity. As can be seen from Figs. 5.26-5.27, for the very lightly damped case, standing wave patterns appear both fore and aft of the contact patch. This follows from the fact that there was insufficient damping to attenuate the inertial interplay in circumferential direction. Once sufficient damping is introduced, essentially all the fore interactions are attenuated.

From a comparison of Figs. 5.25 and 5.29, we see that excellent accuracy is obtained. In this context, it is noted that the moving element approach if used inconjunction with the appropriate FE mesh spacing can handle the complex dynamics associated with real world traveling load problems. This includes

the possibility of handling:

i)   2-D, 3-D and shell type formulations;

ii)   Contact with and without friction;

iii) Small and large deformations effects and;

iv)   Viscoelastic behavior.

6. Summary

Based on the moving strategy developed in Part 1, this paper derived 3-D, shell and contact algorithm extensions. These modelling capabilities were extensively benchmarked to evaluate their operational capabilities. This included both analytical and experimental correlations. As was seen, excellent agreement was obtained over a wide range of physical situations namely:

i)   Traveling load problems involving moving
      velocities over the full interval including
      critical speeds;

ii)   3-D, shell and 2-D situations; and

iii) Full simulation of rolling contact accomo-
      dating viscoelasticity and the full definition
      of inertial effects.

Note, due to the manner of formulation, the moving element procedure can be encoded into any of the currently available general purpose codes. This will enable the handling of moving load/boundary condition problems.

The author acknowledges the helpful technical stimulation of John Tanner of NASA Langley.

References

1. Padovan, J. and Tovichakchaikul, S., "Finite Element Analysis of Steadily Moving Contact Fields", Jr. of Computers and Structures, 18, 191, 1984.

2. Padovan, J. and Paramadilok, O., "Transient and Steady State Viscoelastic Rolling Contact", Jr. of Computers and Structures, 20, 545, 1985.

3. Padovan, J., "Finite Element Analysis of Steady and Transiently Moving/Rolling Nonlinear Viscoelastic Structure - Part I, Theory", Jr. of Computers and Structure (in review).

4. Padovan, J. and Moscarello, R., "Locally Bound Constrained Newton Raphson Solution Algorithms", Jr. of Computers and Structures, (in press).

5. Zienkiewicz, O.C., "The Finite Element Method", McGraw Hill, New York, 1982.

6. Bathe, K.J., "Finite Element Procedures in Engineering Analysis", Prentice Hall, New Jersey, 1983.

7. Archer, J.S., "Consistent Mass Matrix for Distributed Systems", Proc. Am. Soc. Civ. Eng., 89, ST4, 161, 1963.

8. Padovan, J., Zeid, I., "Finite Element Modelling of Rolling Contact", Jr. of Computers and Structures, 14, 163, 1981.

9. Hughes, R.L., Taylor, R.L., Sackman, J.L., Curnier, A. and Kanoknukulchai, W., "A Finite Element Method for a Class of Contact Impact Problems", Comp. Math. .Mech. Engr., 8, 249, 1976.

10. Oden, J.T. and Kikuchi, N., "Finite Element Methods for Constrained Problems in Elasticity", Int. J. Num. Meth. Engr., 18, 701, 1982.

11. Zienkiewicz, O.C., Best, B., Dullage, C. and Stagg, K.G., "Analysis of Nonlinear Problems in Rock Mechanics with Particular Reference to Jointed Rock Systems", Proc. 2nd Conf. ISRM, Beograd, 8, 1970.

12. Stadler, J.T. and Weiss, R.O., "Analysis of Contact Through Finite Element Gaps", Jr. of Computers and Structures, 10, 867, 1978.

13. Padovan, J. and Moscarello, R., Stafford, J. and Tabaddor, F:, "Pantographing Self Adaptive Gap Elements", Jr. of Computers and Structures, 20, 745, 1985.

14. Padovan, J. and Arechages, T., "Formal Convergence Characteristics of Elliptically Constrained Incremental Newton Raphson Algorithm", Int. Jr., Engrg. Sci., 20, 1077, 1982.

15. Bathe, K. J. and Ozdemir, H., "Elastic-Plastic Large Reformation Static and dynamic Analysis", Jr. Computers and Structures, 6, 81, 1976.

16. Chang, T.Y. and Sarwamiphakdi, K., "Large Deformation Analysis of Laminated Shells by Finite Element Method", Jr. of Computers and Structures, 13, 331, 1981.

17. Lestingi, J. and Prachuktam, A., "Blocking Technique for Large Scale Structural Analysis", 3, 669, 1973.

18. Padovan, J., "On Viscoelasticity and Standing Waves in Tires", Tire Sci. and Technology, 4, 233, 1976.

19. Halpin, J.C. and Tsai, S.W., "Environmental Factors in Composity Materials", Design AFML TR67-423.

Figure and Table Captions

| Table No.	Caption
2.1	Shape function components for 20 node isoparametric solid element
2.2	First derivative of shape function components with respect to ξ_1; 20 node isoparametric solid element
2.3	Second derivative of shape function components with respect to ξ_1; 20 node isoparametric solid element
2.4	Mixed second derivative of shape function components with respect to ξ_1; ξ_2; 20 node isoparametric solid element

Figure and Table Captions

| Fig. No.	Caption
2.1	Three Dimensional 20 Node Solid Element in Cartesian Space
2.2	Three Dimensional 20 Node Solid Element in ξ_1, ξ_2, ξ_3 Isoparametric Space
3.1	Reference Surface of the Thick Shell Element in Cartesian Space
3.2	Local Circumferential Positions for a Line of Nodes Used in the Closed Form Mass Formulation
3.3	Division of the Shell Element into Three Zones for the Closed Form Approach
4.1	Attachment and Constrained Face of the Three Dimensional Gap Element with Node Ordering
4.2	Deformed Shape of a Gap Element with Lower Nodes Constrained
4.3	Initial (– + –) and Pantographed (—x—) Shapes Minimizing Gap Element Distortion
4.4	Zone Divisions in the Gap Element Used to Impose Partial Contact by Material Property Change at Integration Points
5.1	Ring on Elastic Foundation Tire Model
5.2	Finite Element Grid of the Ring on Elastic Foundation Tire Model Using Shell Elements for the Ring
5.3	Finite Element Grid of the Ring on Elastic Foundation Tire Model Using Solid Elements for the Ring
5.4	Line Load Across the Width of the Model Used as "Point" Load Excitation
5.5	11th Mode Resonance Response at 145.6 Rad/Sec (119.7 MPH) for Ring Modeled by Shell Elements
5.6	Finite Element Grid for the Ring on Elastic Foundation Model Including Gap Elements
5.7	Deformed Shape and Contact Stress Distribution at 145.6 Rad/Sec (119.7 MPH) and Damping ($\mu=10^{-4}$)
5.8	Finite Element Grid of the Half Torus Model Viewed at a Slight Angle from the Axis of Rotation
5.9	Response of the Torus Model as a Resonance/Critical Speed is Approached and Passed

$$(\xi_1; \ \xi_2; \ \xi_3) \equiv (r; \ s; \ t)$$

NODE	SHAPE FUNCTION (N)
1	$(1/8)(1+r)(1+s)(1+t) - (1/2)(N_9+N_{12}+N_{17})$
2	$(1/8)(1-r)(1+s)(1+t) - (1/2)(N_9+N_{10}+N_{18})$
3	$(1/8)(1-r)(1-s)(1+t) - (1/2)(N_{10}+N_{11}+N_{19})$
4	$(1/8)(1+r)(1-s)(1+t) - (1/2)(N_{11}+N_{12}+N_{20})$
5	$(1/8)(1+r)(1+s)(1-t) - (1/2)(N_{13}+N_{16}+N_{17})$
6	$(1/8)(1-r)(1+s)(1-t) - (1/2)(N_{13}+N_{14}+N_{18})$
7	$(1/8)(1-r)(1-s)(1-t) - (1/2)(N_{14}+N_{15}+N_{19})$
8	$(1/8)(1+r)(1-s)(1-t) - (1/2)(N_{15}+N_{16}+N_{20})$
9	$(1/4)(1-r^2)(1+s)(1+t)$
10	$(1/4)(1-r)(1-s^2)(1+t)$
11	$(1/4)(1-r^2)(1-s)(1+t)$
12	$(1/4)(1+r)(1-s^2)(1+t)$
13	$(1/4)(1-r^2)(1+s)(1-t)$
14	$(1/4)(1-r)(1-s^2)(1-t)$
15	$(1/4)(1-r^2)(1-s)(1-t)$
16	$(1/4)(1+r)(1-s^2)(1-t)$
17	$(1/4)(1+r)(1+s)(1-t^2)$
18	$(1/4)(1-r)(1+s)(1-t^2)$
19	$(1/4)(1-r)(1-s)(1-t^2)$
20	$(1/4)(1+r)(1-s)(1-t^2)$

Table 2.1   Shape function components for 20 node
            isoparametric solid element

$$(\xi_1; \; \xi_2; \; \xi_3) \equiv (r; \; s; \; t)$$

NODE	DERIVATIVE OF SHAPE FUNCTION ($N_{,r}$)
1	$(1/8)(1+s)(1+t) \; - \; (1/2)(N_{9,r}+N_{12,r}+N_{17,r})$
2	$(-1/8)(1+s)(1+t) \; - \; (1/2)(N_{9,r}+N_{10,r}+N_{18,r})$
3	$(-1/8)(1-s)(1+t) \; - \; (1/2)(N_{10,r}+N_{11,r}+N_{19,r})$
4	$(1/8)(1-s)(1+t) \; - \; (1/2)(N_{11,r}+N_{12,r}+N_{20,r})$
5	$(1/8)(1+s)(1-t) \; - \; (1/2)(N_{13,r}+N_{16,r}+N_{17,r})$
6	$(-1/8)(1+s)(1-t) \; - \; (1/2)(N_{13,r}+N_{14,r}+N_{18,r})$
7	$(-1/8)(1-s)(1-t) \; - \; (1/2)(N_{14,r}+N_{15,r}+N_{19,r})$
8	$(1/8)(1-s)(1-t) \; - \; (1/2)(N_{15,r}+N_{16,r}+N_{20,r})$
9	$(-1/2)(r)(1+s)(1+t)$
10	$(-1/4)(1-s^2)(1+t)$
11	$(-1/2)(r)(1-s)(1+t)$
12	$(1/4)(1-s^2)(1+t)$
13	$(-1/2)(r)(1+s)(1-t)$
14	$(-1/4)(1-s^2)(1-t)$
15	$(-1/2)(r)(1-s)(1-t)$
16	$(1/4)(1-s^2)(1-t)$
17	$(1/4)(1+s)(1-t^2)$
18	$(-1/4)(1+s)(1-t^2)$
19	$(-1/4)(1-s)(1-t^2)$
20	$(1/4)(1-s)(1-t^2)$

Table 2.2   First derivative of shape function components with respect to ξ_1: 20 node isoparametric solid element

$$(\xi_1; \xi_2; \xi_3) \equiv (r; s; t)$$

NODE	DERIVATIVE OF SHAPE FUNCTION ($N_{,rr}$)
1	$(-1/2)(N_{9,rr} + N_{12,rr} + N_{17,rr})$
2	$(-1/2)(N_{9,rr} + N_{10,rr} + N_{18,rr})$
3	$(-1/2)(N_{10,rr} + N_{11,rr} + N_{19,rr})$
4	$(-1/2)(N_{11,rr} + N_{12,rr} + N_{20,rr})$
5	$(-1/2)(N_{13,rr} + N_{16,rr} + N_{17,rr})$
6	$(-1/2)(N_{13,rr} + N_{14,rr} + N_{18,rr})$
7	$(-1/2)(N_{14,rr} + N_{15,rr} + N_{19,rr})$
8	$(-1/2)(N_{15,rr} + N_{16,rr} + N_{20,rr})$
9	$(-1/2)(1+s)(1+t)$
10	0
11	$(-1/2)(1-s)(1+t)$
12	0
13	$(-1/2)(1+s)(1-t)$
14	0
15	$(-1/2)(1-s)(1-t)$
16	0
17	0
18	0
19	0
20	0

Table 2.3   Second derivative of shape function components with respect to ξ_1; 20 node isoparametric solid element

$$(\xi_1;\ \xi_2;\ \xi_3) \equiv (r;\ s;\ t)$$

NODE	DERIVATIVE OF SHAPE FUNCTION $(N,_{rs})$
1	$(1/8)(1+t) - (1/2)(N_{9,rs}+N_{12,rs}+N_{17,rs})$
2	$(-1/8)(1+t) - (1/2)(N_{9,rs}+N_{10,rs}+N_{18,rs})$
3	$(1/8)(1+t) - (1/2)(N_{10,rs}+N_{11,rs}+N_{19,rs})$
4	$(-1/8)(1+t) - (1/2)(N_{11,rs}+N_{12,rs}+N_{20,rs})$
5	$(1/8)(1-t) - (1/2)(N_{13,rs}+N_{16,rs}+N_{17,rs})$
6	$(-1/8)(1-t) - (1/2)(N_{13,rs}+N_{14,rs}+N_{18,rs})$
7	$(1/8)(1-t) - (1/2)(N_{14,rs}+N_{15,rs}+N_{19,rs})$
8	$(-1/8)(1-t) - (1/2)(N_{15,rs}+N_{16,rs}+N_{20,rs})$
9	$(-1/2)(r)(1+t)$
10	$(1/2)(s)(1+t)$
11	$(1/2)(r)(1+t)$
12	$(-1/2)(s)(1+t)$
13	$(-1/2)(r)(1-t)$
14	$(1/2)(s)(1-t)$
15	$(1/2)(r)(1-t)$
16	$(-1/2)(s)(1-t)$
17	$(1/4)(1-t^2)$
18	$(-1/4)(1-t^2)$
19	$(1/4)(1-t^2)$
20	$(-1/4)(1-t^2)$

Table 2.4   Mixed second derivative of shape function components with respect to $\xi_1;\ \xi_2$; 20 node isoparametric solid element
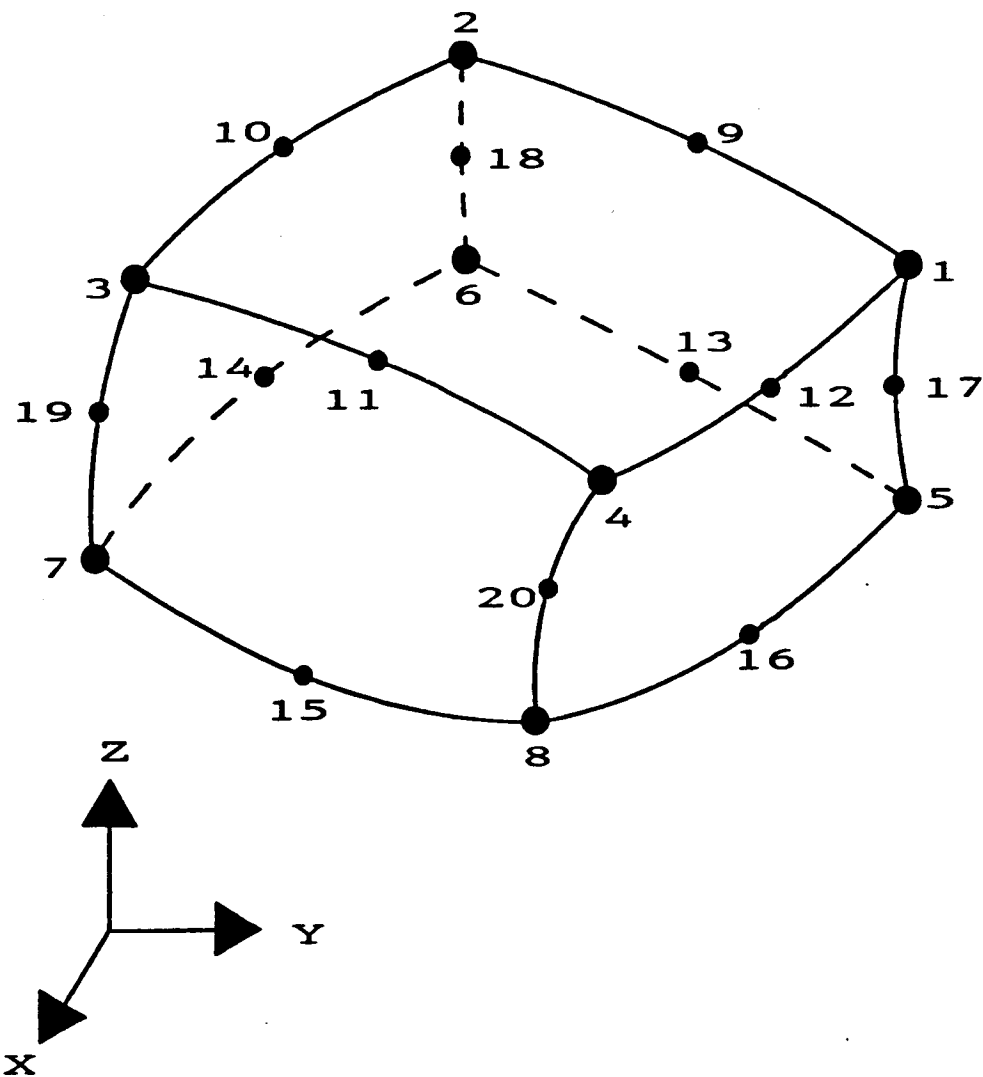
Fig. 2.1   THREE DIMENSIONAL 20 NODE
           SOLID ELEMENT IN CARTESIAN
           SPACE
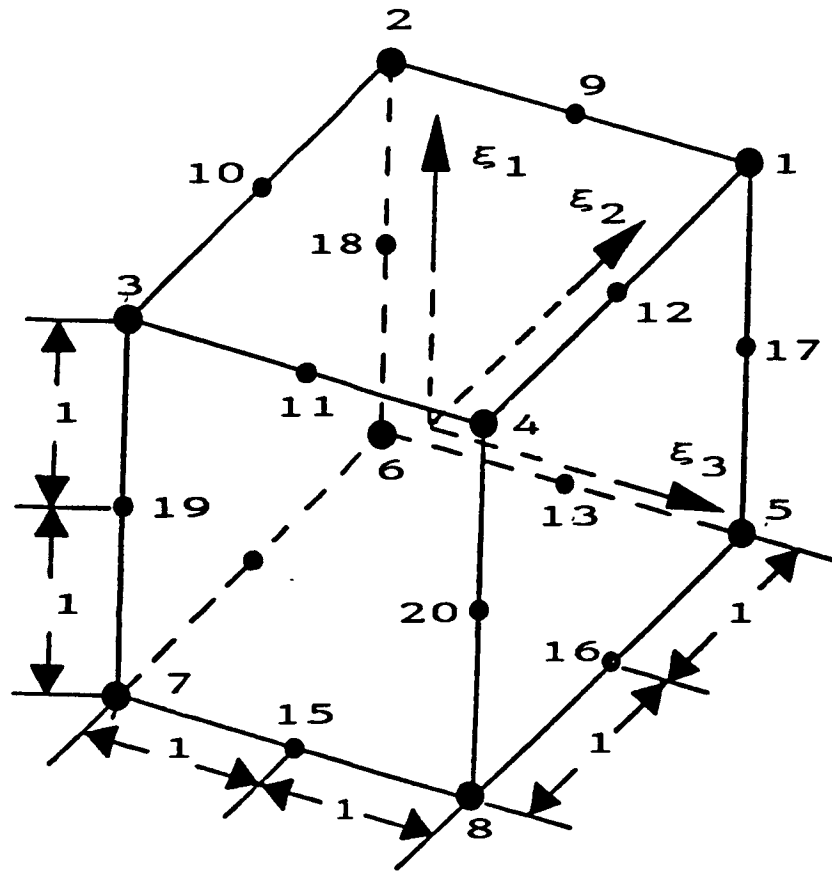
Fig. 2.2   THREE DIMENSIONAL 20 NODE SOLID ELEMENT IN ξ_1, ξ_2, ξ_3 ISOPARAMETRIC SPACE
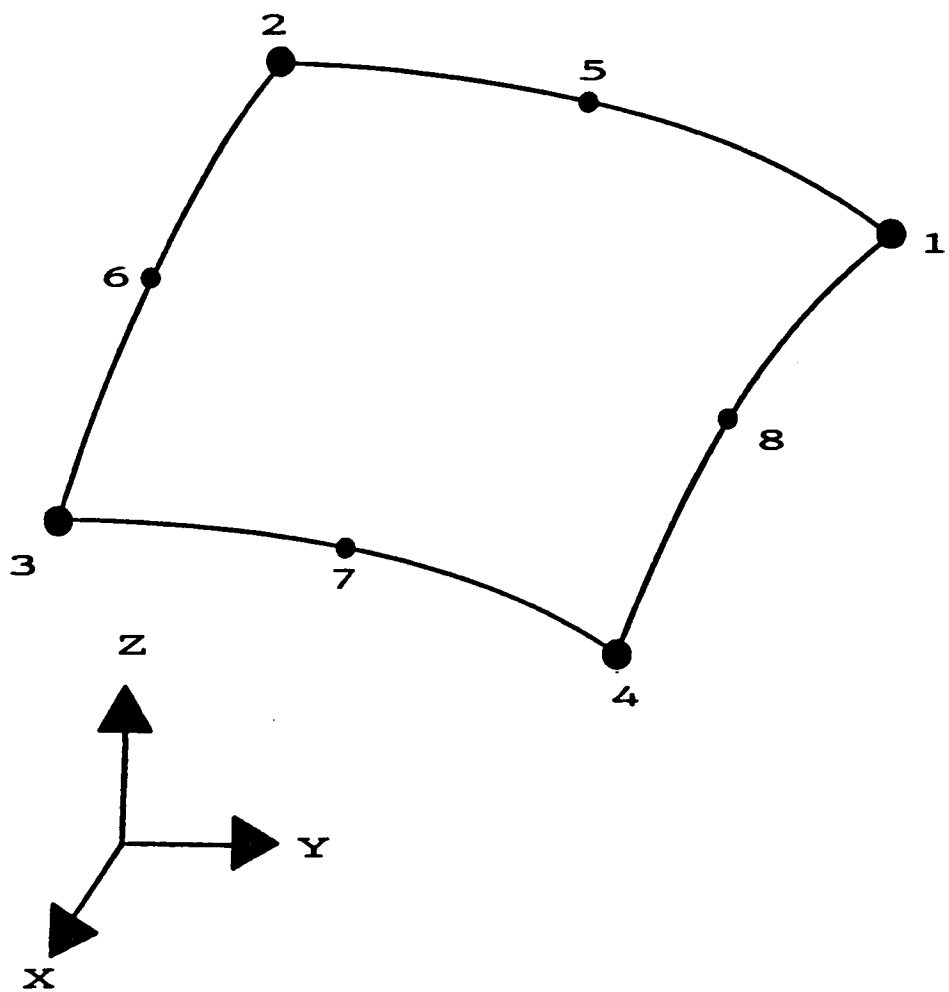
Fig. 3.1 REFERENCE SURFACE OF
THE THICK SHELL ELEMENT
IN CARTESIAN SPACE
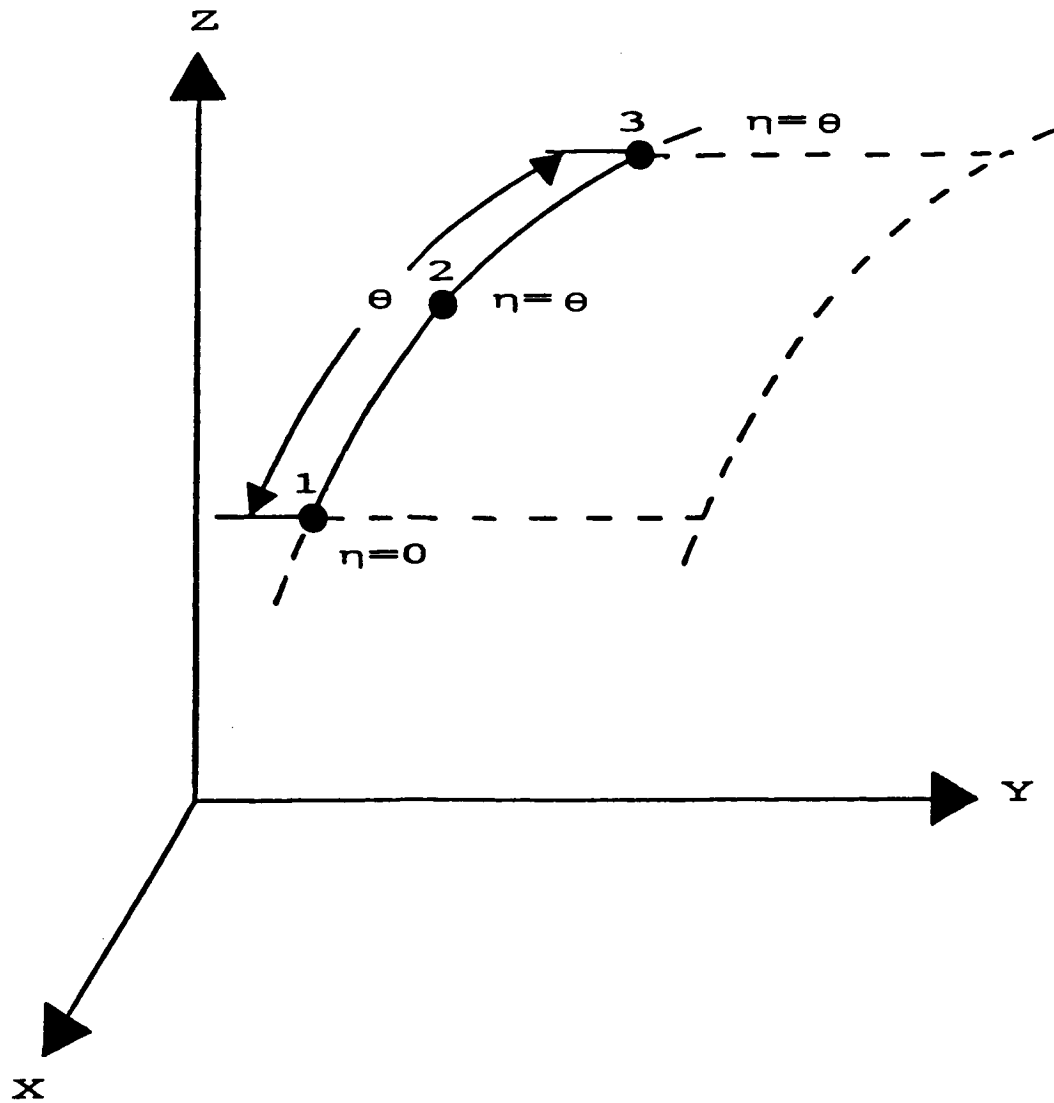
Fig. 3.2 LOCAL CIRCUMFERENTIAL
POSITIONS FOR A LINE
OF NODES USED IN THE
CLOSED FORM MASS
FORMULATION
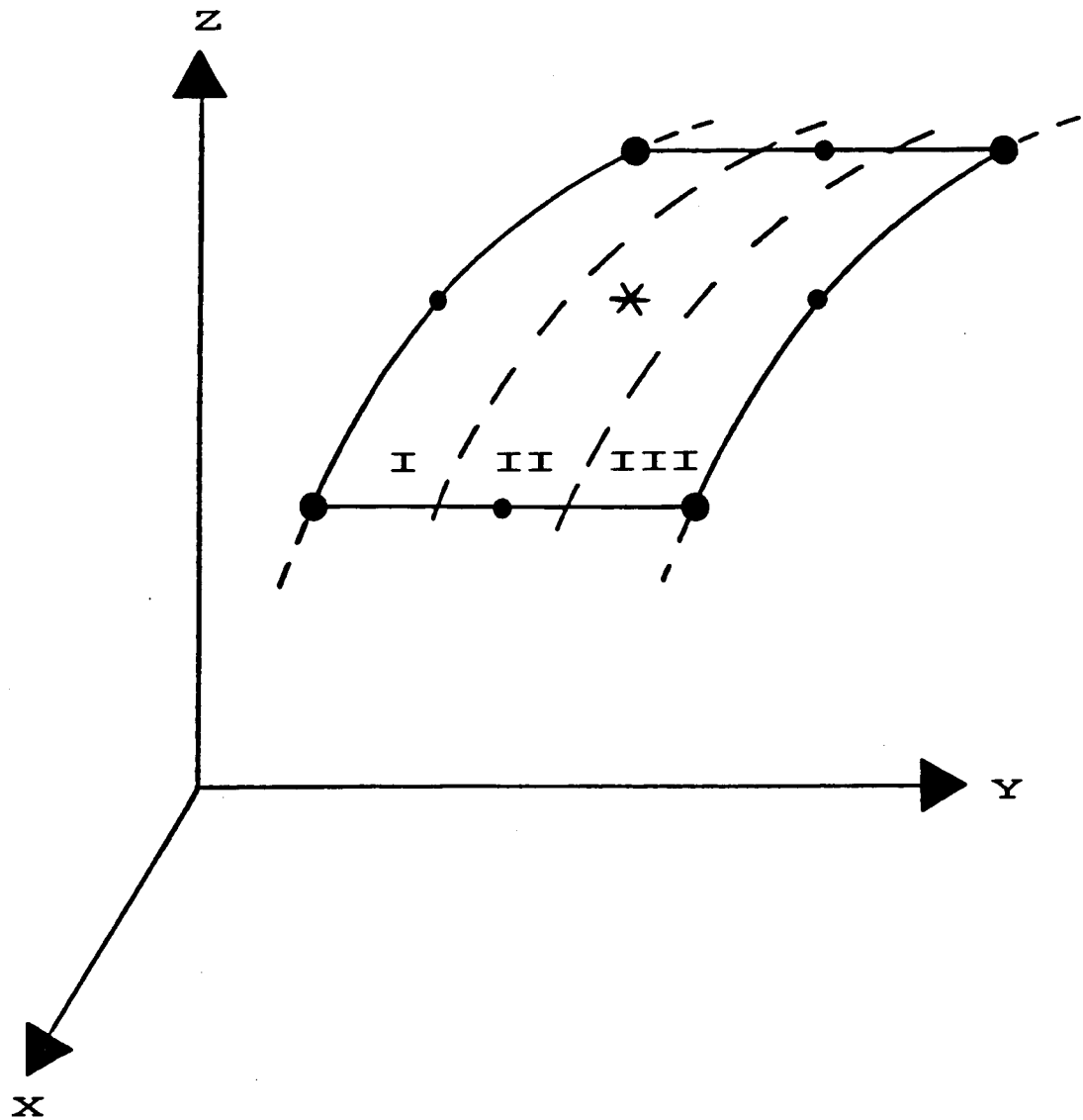
Fig. 3.3   DIVISION OF THE SHELL
           ELEMENT INTO THREE ZONES
           FOR THE CLOSED FORM
           APPROACH
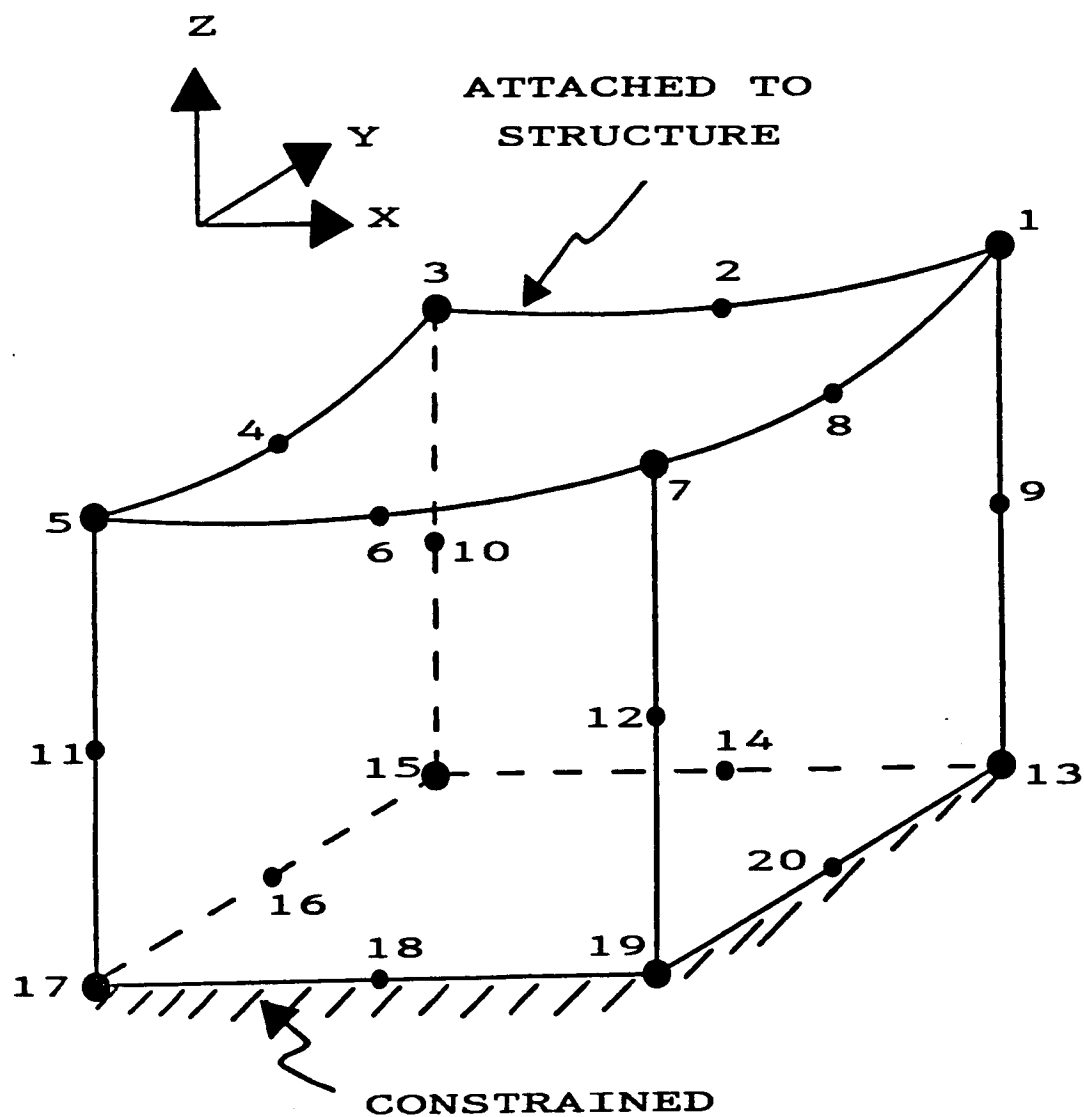
Fig. 4.1 ATTACHMENT AND CONSTRAINED
FACES OF THE THREE DIMEN-
SIONAL GAP ELEMENT WITH NODE
ORDERING
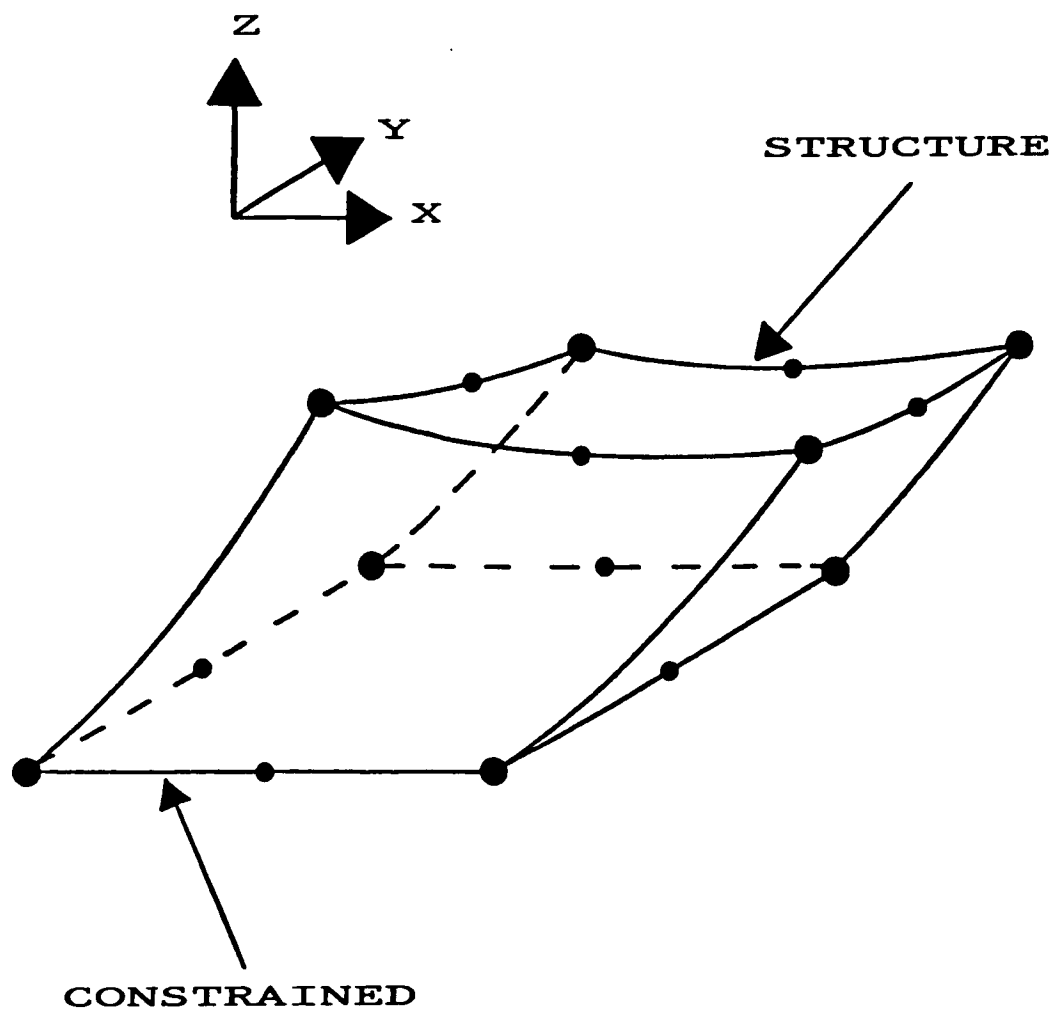
Fig. 4.2   DEFORMED SHAPE OF A GAP
ELEMENT WITH LOWER NODES
CONSTRAINED
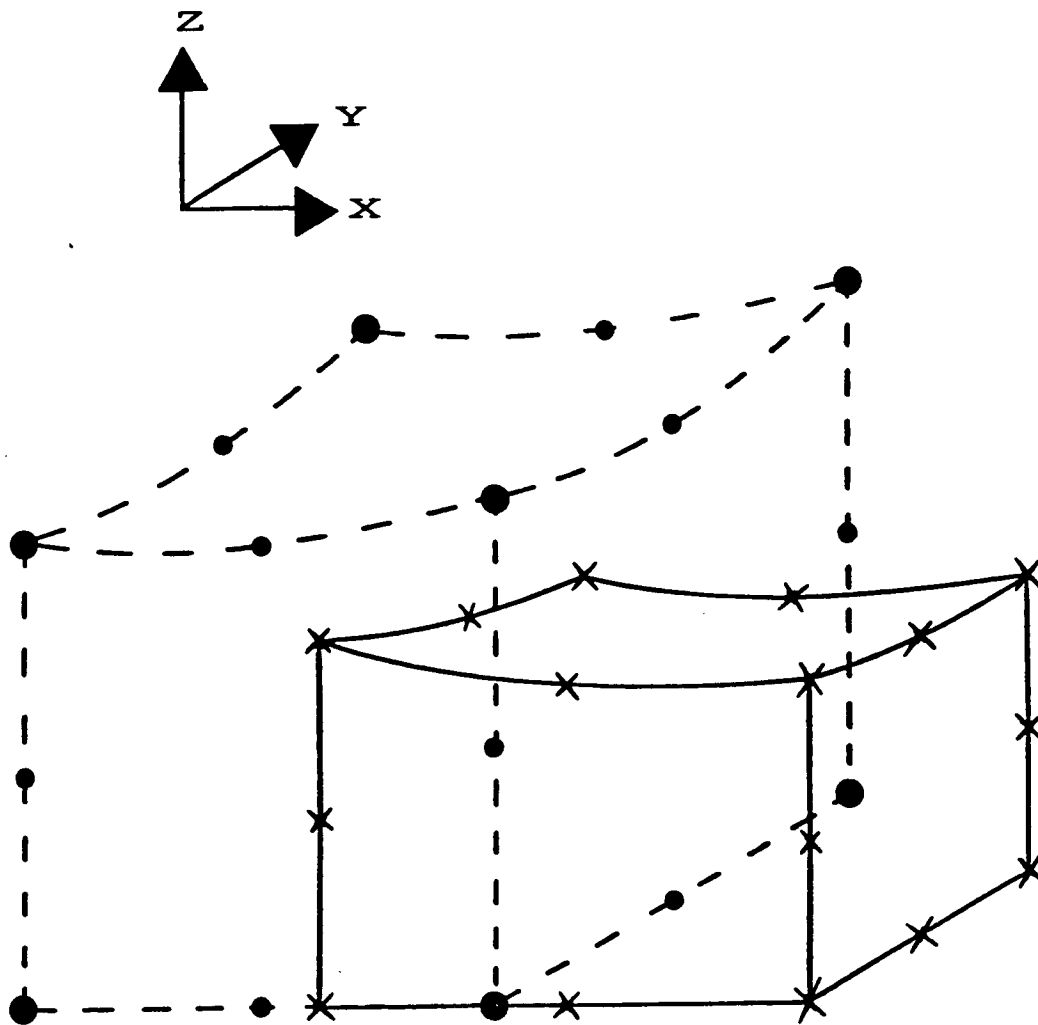
Fig. 4.3   INITIAL (— • —) AND
            PANTOGRAPHED (—X—)
            SHAPES MINIMIZING GAP
            ELEMENT DISTORTION
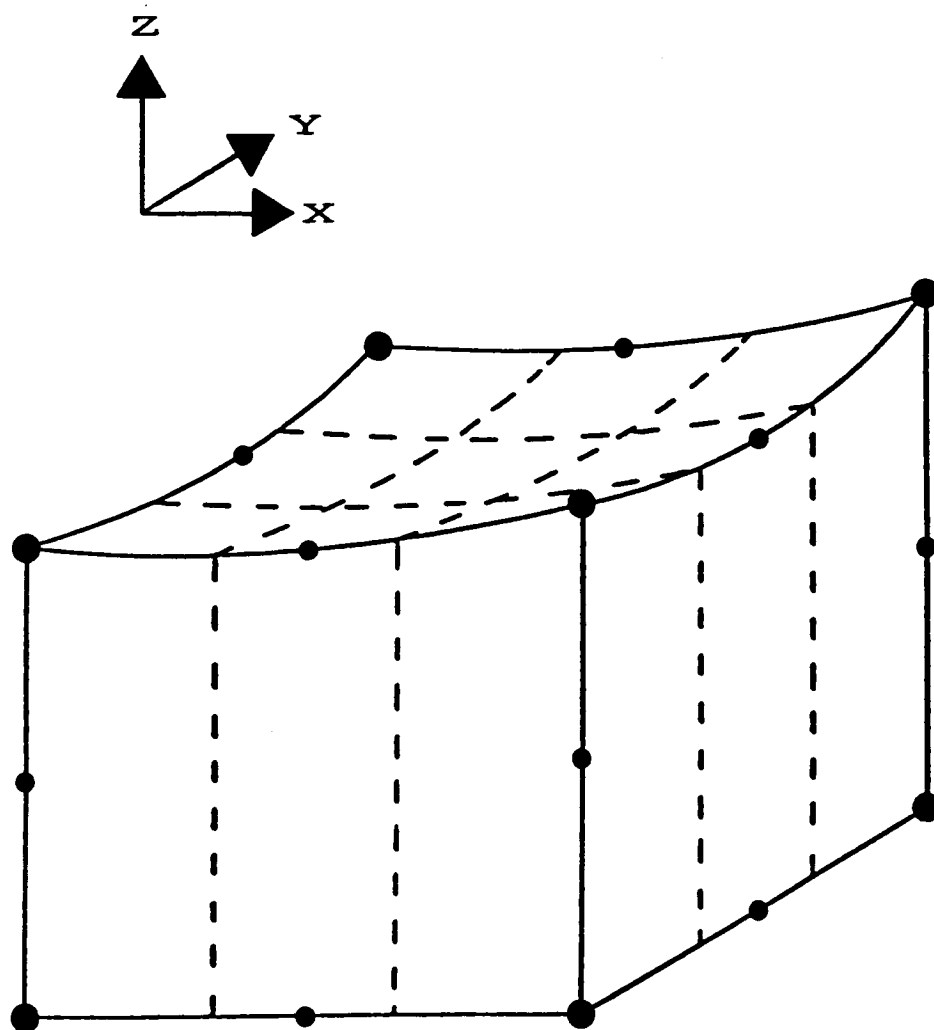
Fig. 4.4   ZONE DIVISIONS IN THE GAP
           ELEMENT USED TO IMPOSE
           PARTIAL CONTACT BY MATERIAL
           PROPERTY CHANGE AT INTE-
           GRATION POINTS

14.467"

13.533"

7.5"

FIXED RIM

RING
(TREAD/BELT)

FOUNDATION
(SIDEWALL)

Fig. 5.1 RING ON ELASTIC FOUNDATION
TIRE MODEL

3-D SOLID
ELEMENT
(FOUNDATION)

SHELL ELEMENT
(RING)

Fig. 5.2 FINITE ELEMENT GRID OF THE
RING ON ELASTIC FOUNDATION
TIRE MODEL USING SHELL
ELEMENTS FOR THE RING

3-D SOLID
ELEMENTS
(FOUNDATION)
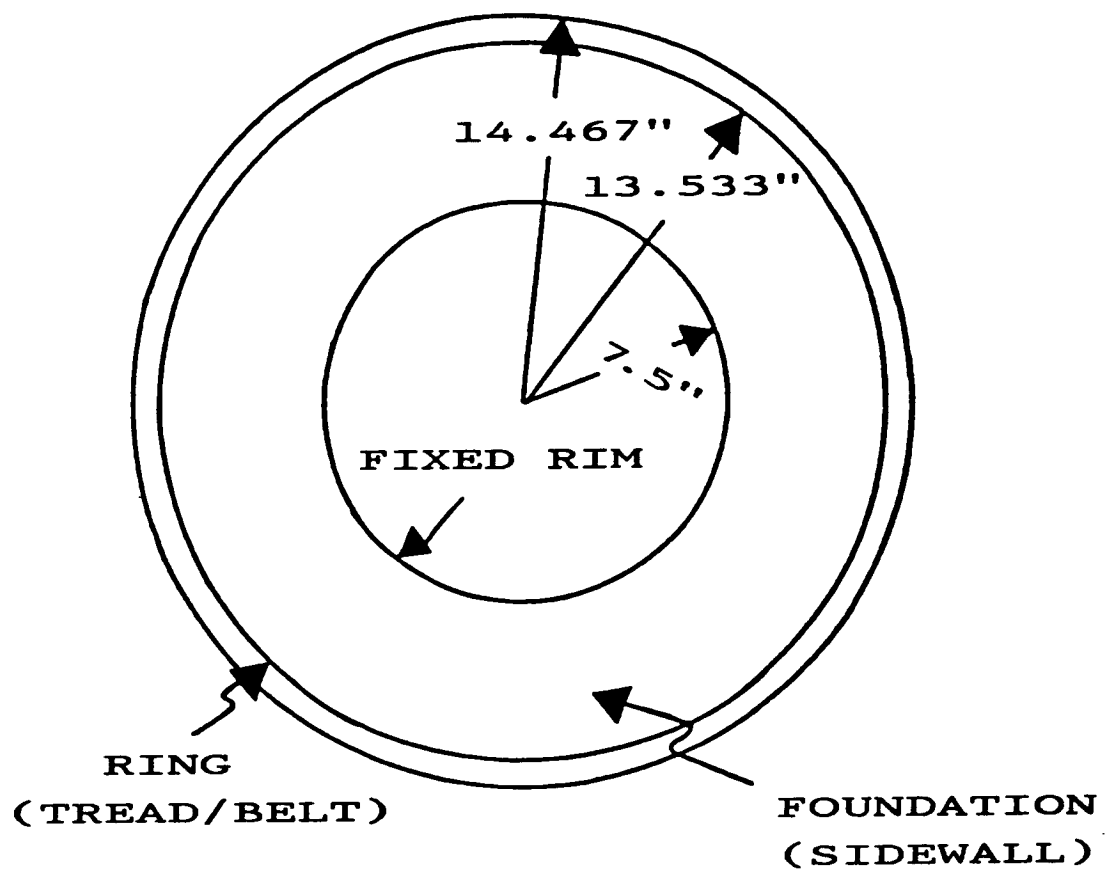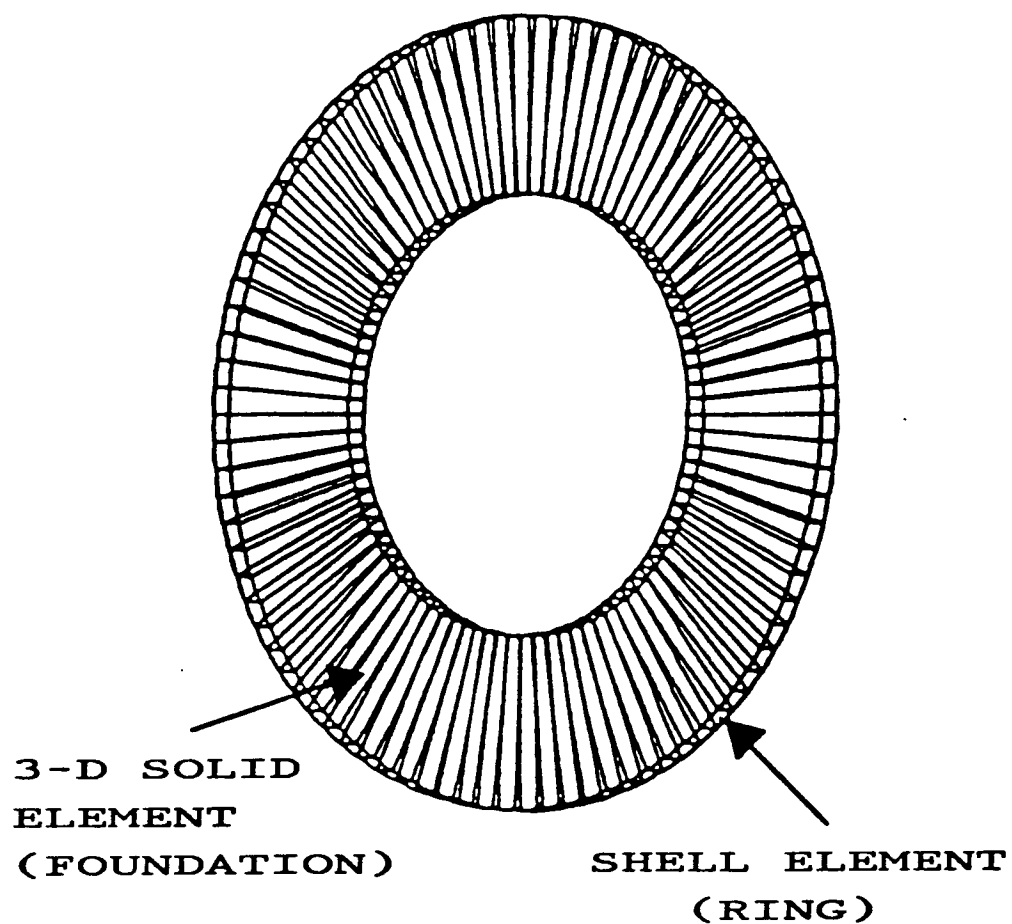
3-D SOLID ELEMENTS
(RING)
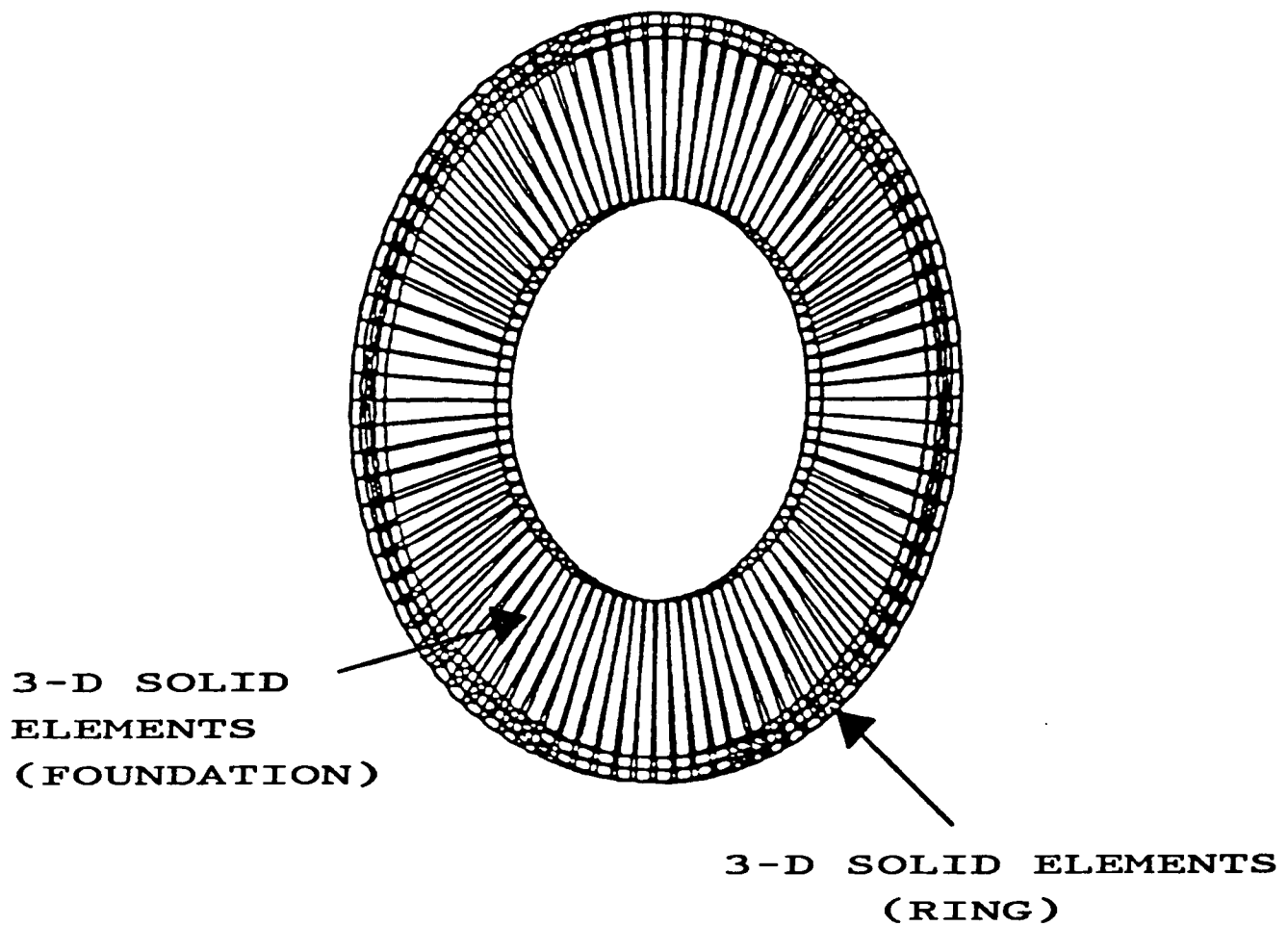
Fig. 5.3 FINITE ELEMENT GRID OF THE RING
ON ELASTIC FOUNDATION TIRE MODEL
USING SOLID ELEMENTS FOR THE
RING
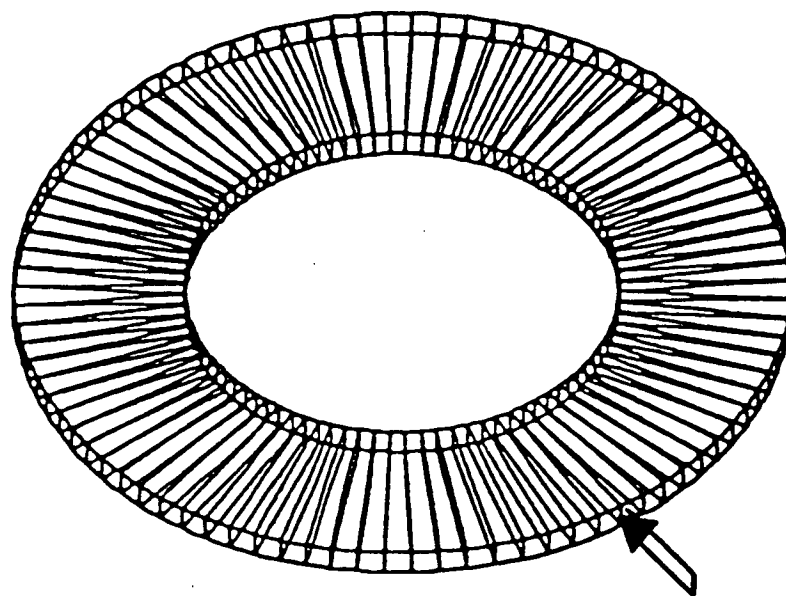
APPLIED "TRAVELING"
RADIAL "POINT" LOAD

Fig. 5.4   LINE LOAD ACROSS THE WIDTH
           OF THE MODEL USED AS "POINT"
           LOAD EXCITATION
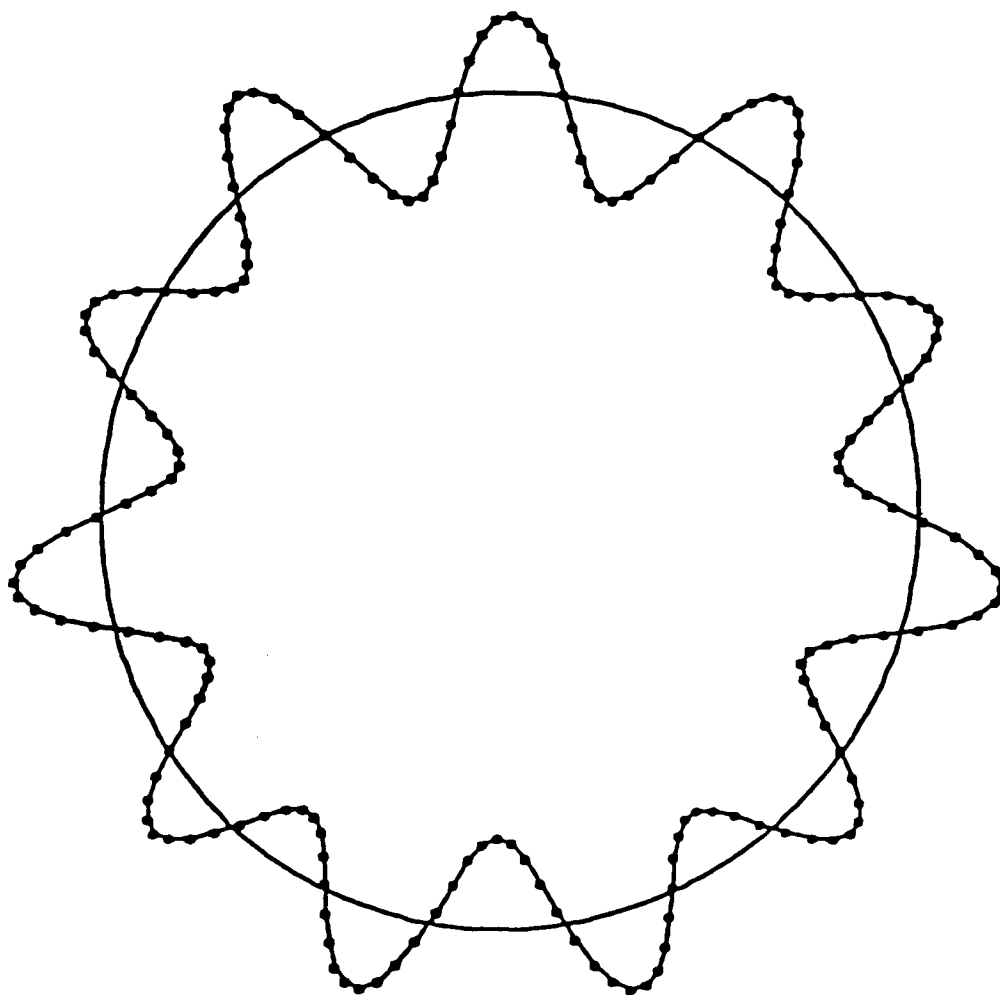
Fig. 5.5 11th MODE RESONANCE
RESPONSE AT 145.6 RAD/SEC
(119.7 MPH) FOR RING
MODELED BY SHELL ELEMENTS
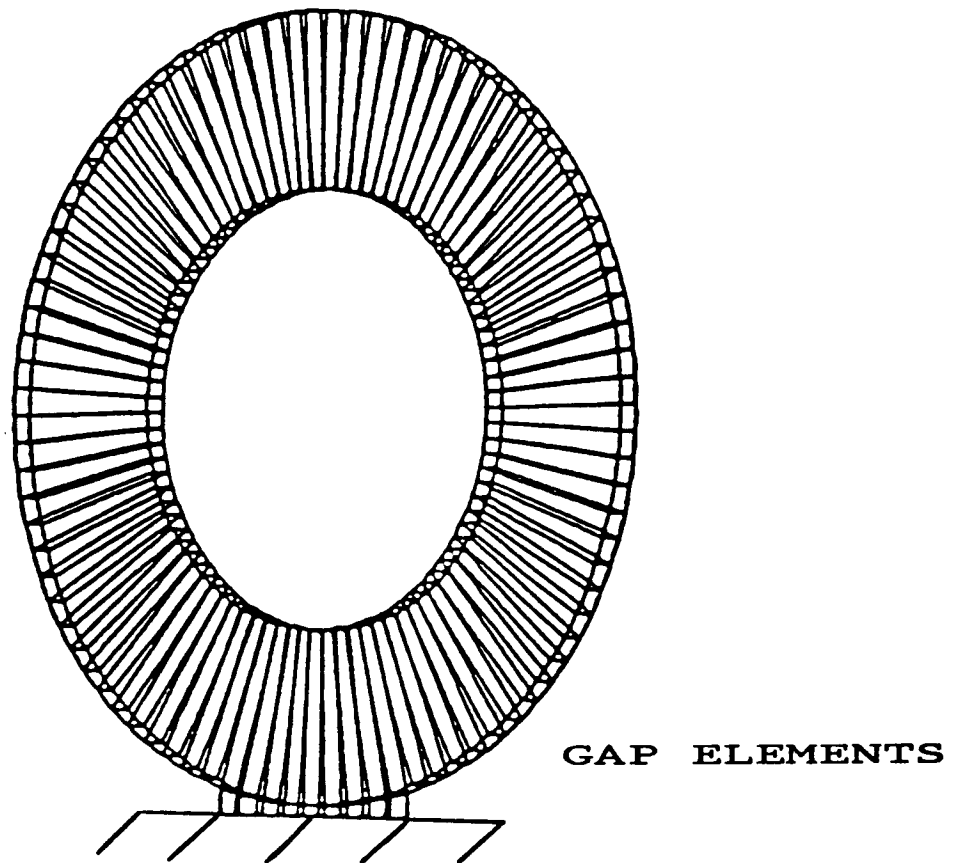
GAP ELEMENTS

Fig. 5.6 FINITE ELEMENT GRID FOR
THE RING ON ELASTIC
FOUNDATION MODEL INCLUDING
GAP ELEMENTS

STANDING
WAVE

CONTACT FORCE DISTRIBUTION
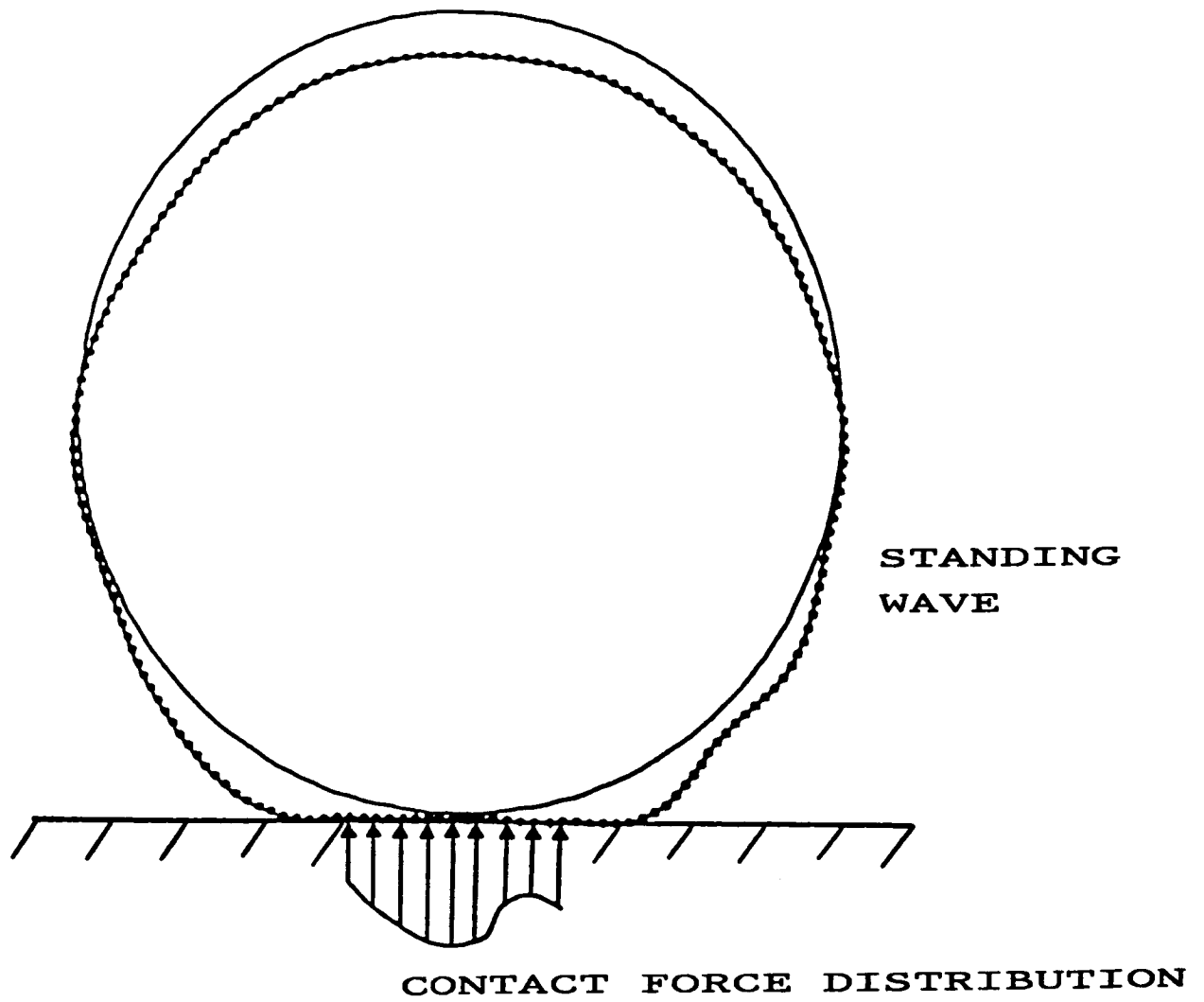
Fig. 5.7   DEFORMED SHAPE AND CONTACT STRESS
DISTRIBUTION AT 145.6 RAD/SEC
(119.7 MPH) AND DAMPING
($\mu=10^{-4}$)
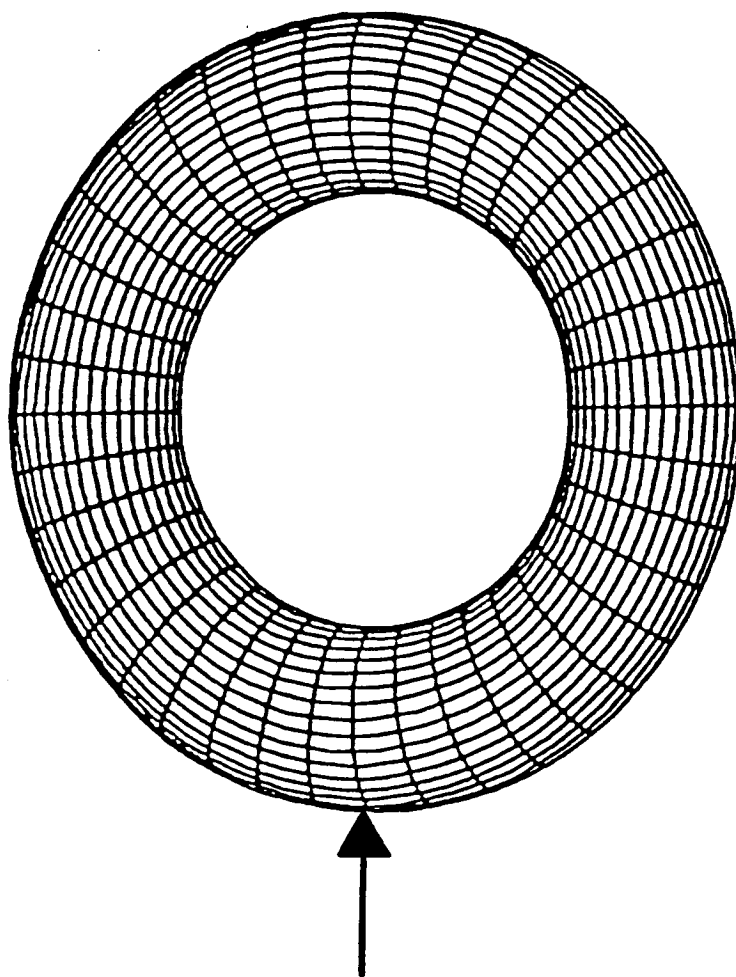
RADIAL TRAVELING LOAD

Fig. 5.8   FINITE ELEMENT GRID OF THE HALF
           TORUS MODEL VIEWED AT A SLIGHT
           ANGLE FROM THE AXIS OF ROTATION
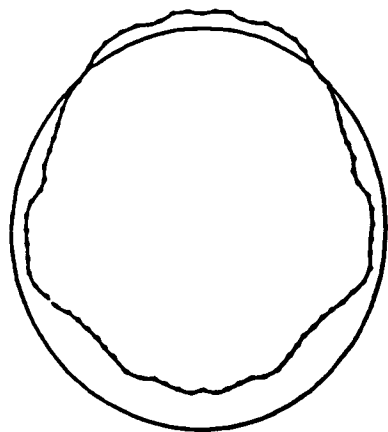
a) 275 RAD/SEC
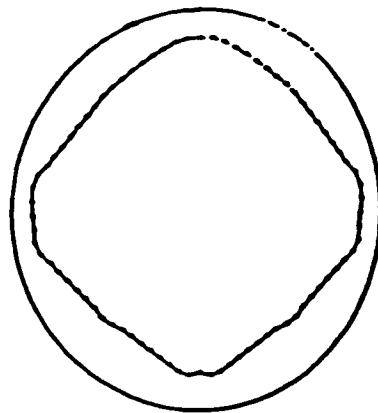
b) 282 RAD/SEC
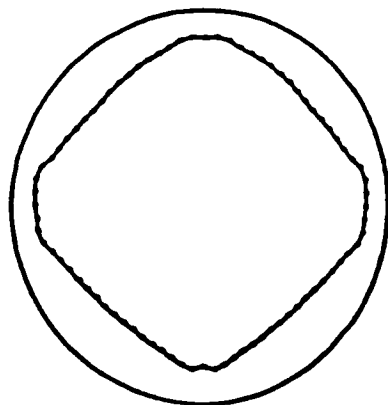
c) 283 RAD/SEC
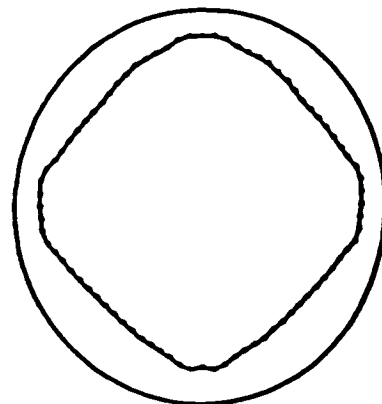
d) 284 RAD/SEC
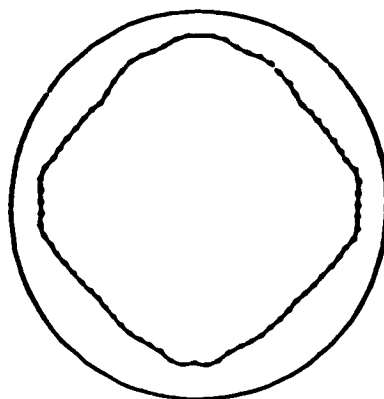
e) 285 RAD/SEC

Fig. 5.9   RESPONSE OF THE TORUS MODEL AS A
RESONANCE/CRITICAL SPEED IS
APPROACHED AND PASSED.
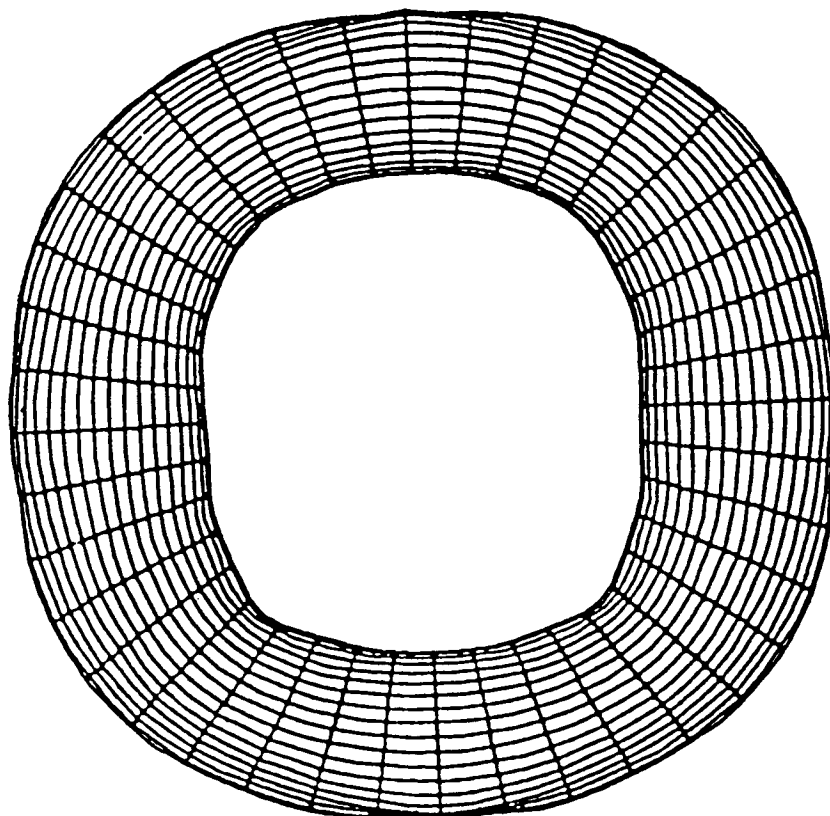
Fig. 5.10   4th MODE RESONANCE
             RESPONSE OF THE TORUS
             MODEL AT 284 RAD/SEC
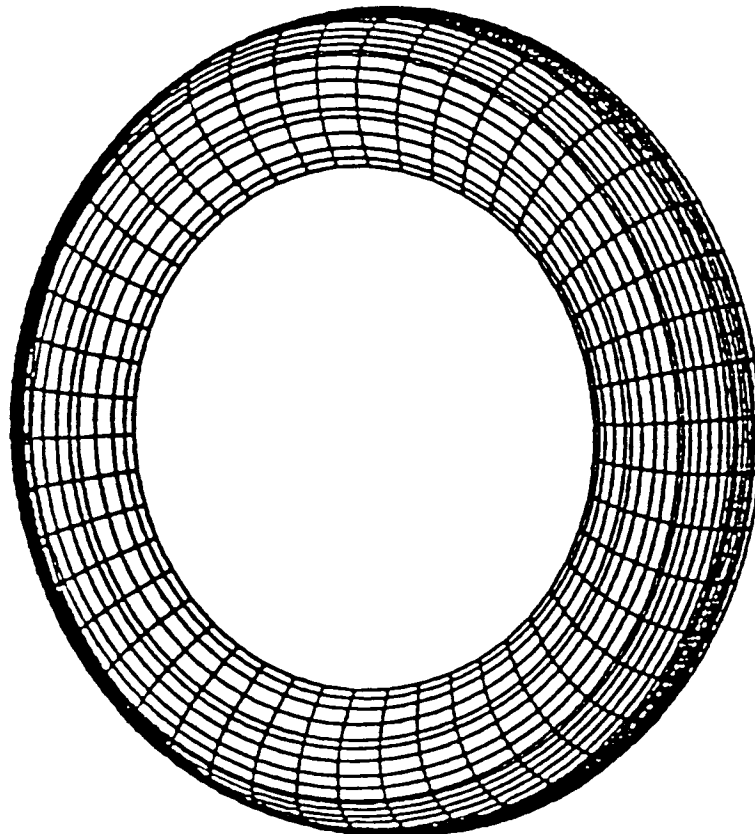
Fig. 5.11   FINITE ELEMENT GRID OF THE
            HALF TIRE MODEL USED IN THE
            ROLLING CONTACT MODEL
            (15000 DEGREES)
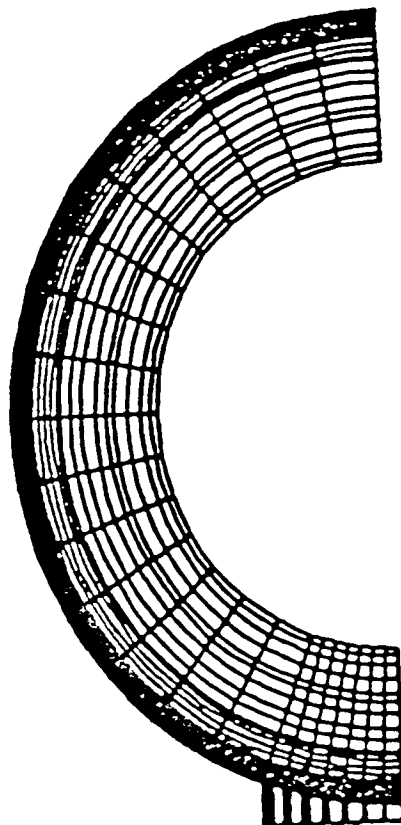
GAP ELEMENTS

Fig. 5.12   FINITE ELEMENT GRID OF THE
            QUARTER TIRE MODEL WITH GAP
            ELEMENTS ATTACHED IN
            POTENTIAL CONTACT ZONE
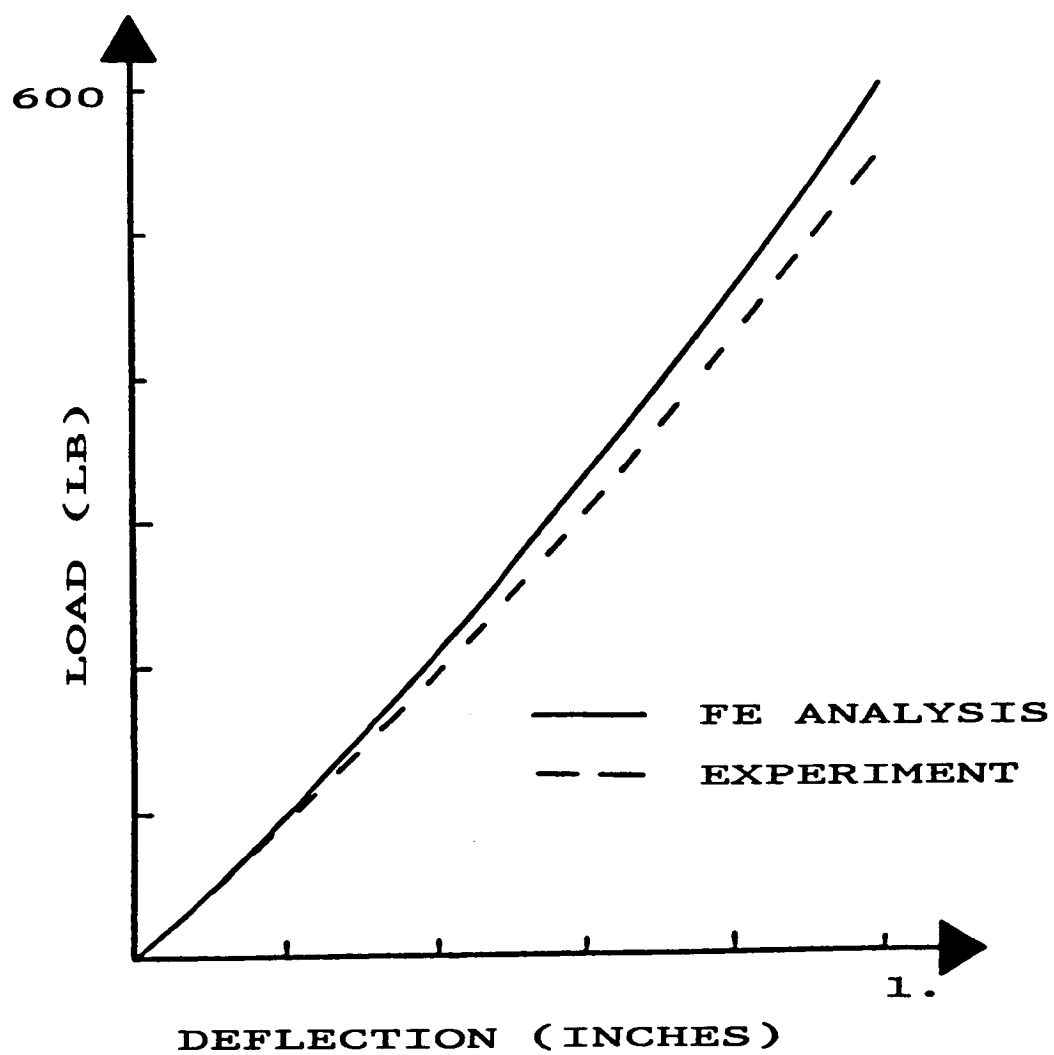
Fig. 5.13 PREDICTED AND MEASURED
STATIC LOAD-DEFLECTION
RESPONSE OF TIRE
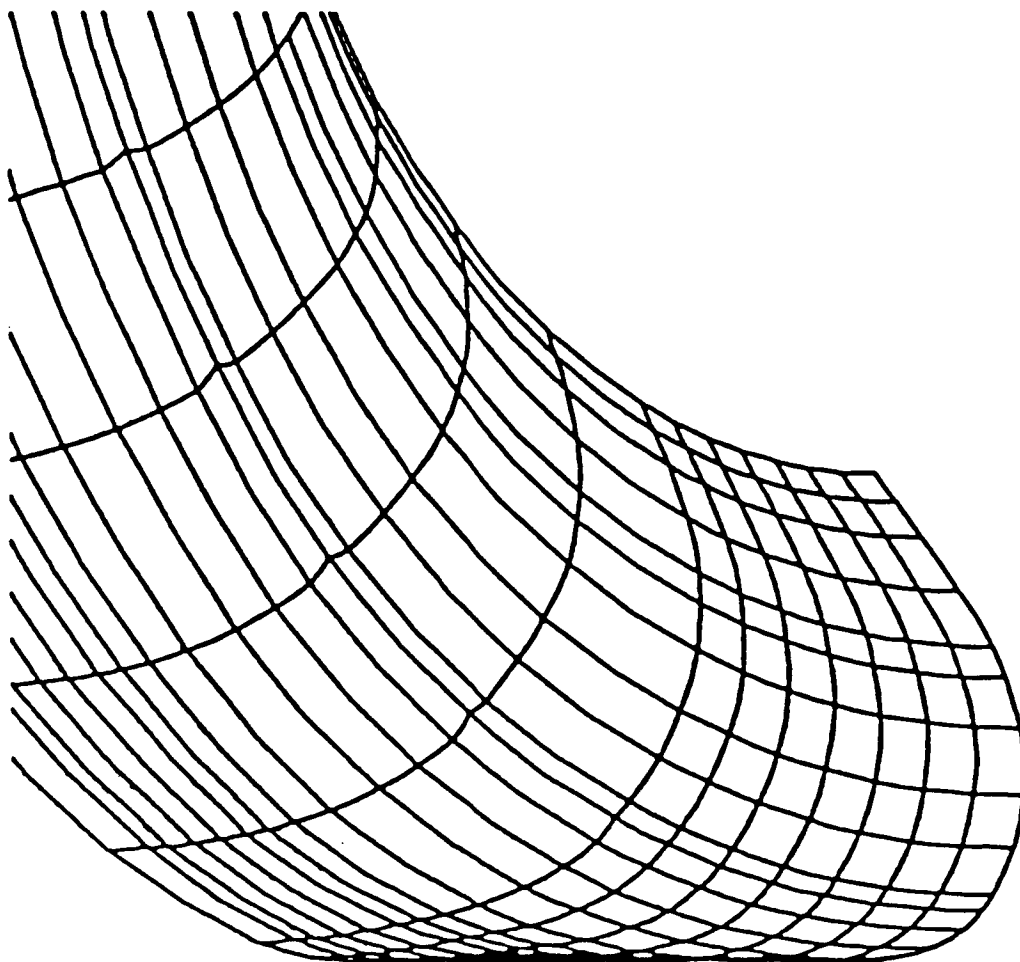
Fig. 5.14   DEFORMED SHAPE OF THE
            QUARTER TIRE MODEL WITH
            1.0 INCH AXLE DEFLECTION

RADIAL TRAVELING
LOAD
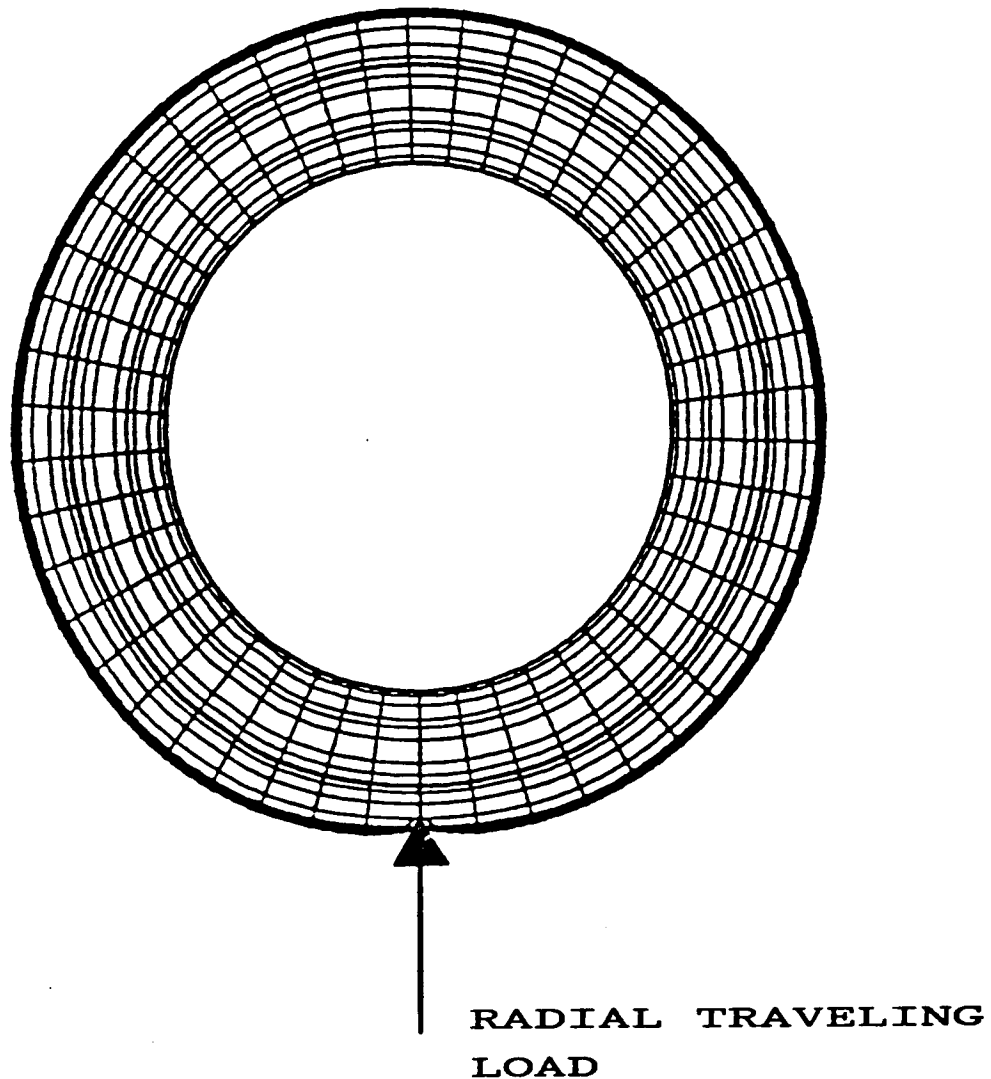
Fig. 5.15   SIDE VIEW OF THE FE
MODEL RESPONSE TO RADIAL
CIRCUMFERENTIALLY TRAVEL-
ING LOAD MOVING AT 135.2
RAD/SEC (90 MPH)
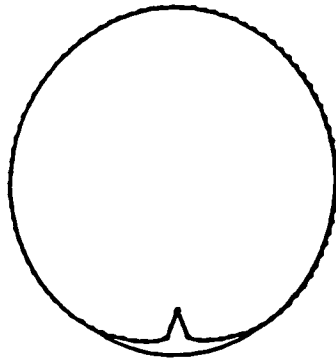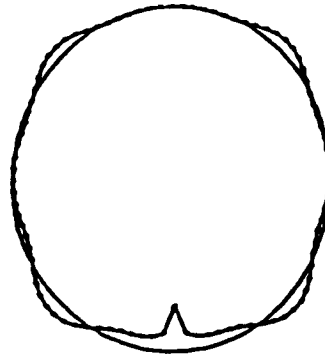
a) 170.0 RAD/SEC   b) 175.0 RAD/SEC
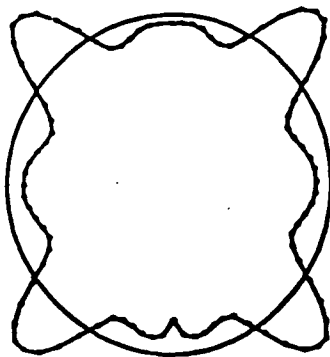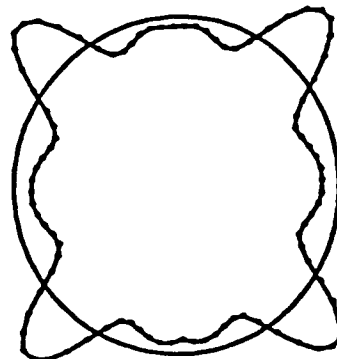
c) 175.5 RAD/SEC   d) 175.7 RAD/SEC
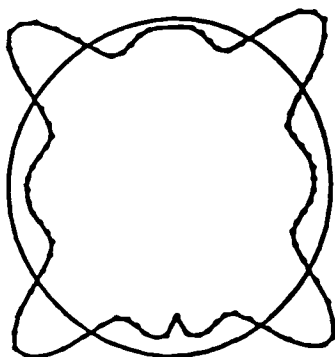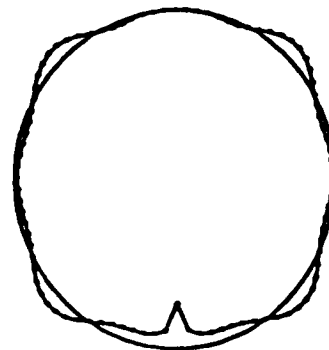
e) 176.0 RAD/SEC   f) 176.5 RAD/SEC

Fig. 5.16   PREDICTED RESPONSE OF TIRE'S
CROWN NODES AS TRAVELING LOAD
SPEED APPROACHES AND PASSES A
RESONANCE/CRITICAL SPEED
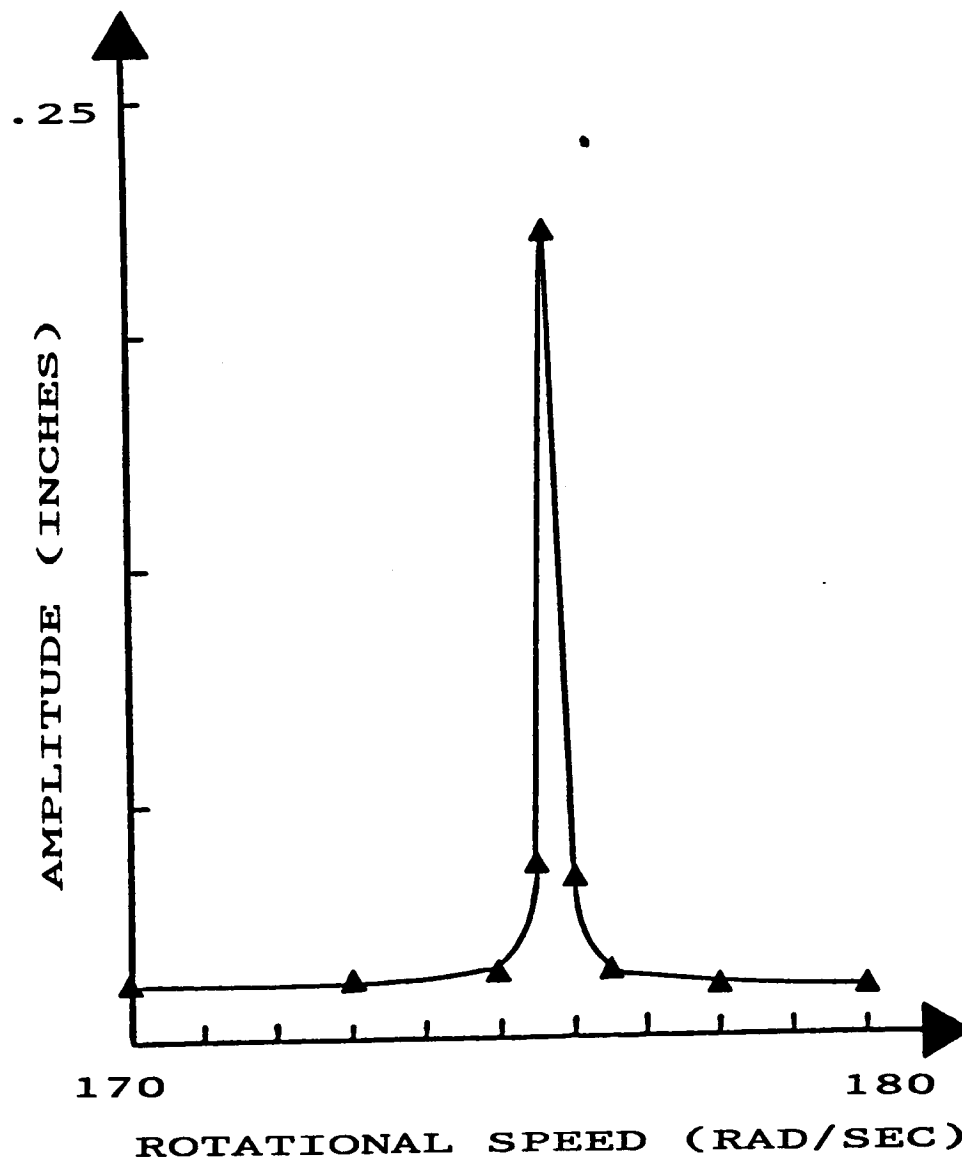
Fig. 5.17 TRAVELING SPEED-RADIAL
DISPLACEMENT SPECTRUM;
APPROACH AND PASSING
BEHAVIOR ABOUT RESONANCE/
CRITICAL SPEED

RADIAL TRAVELING
LOAD
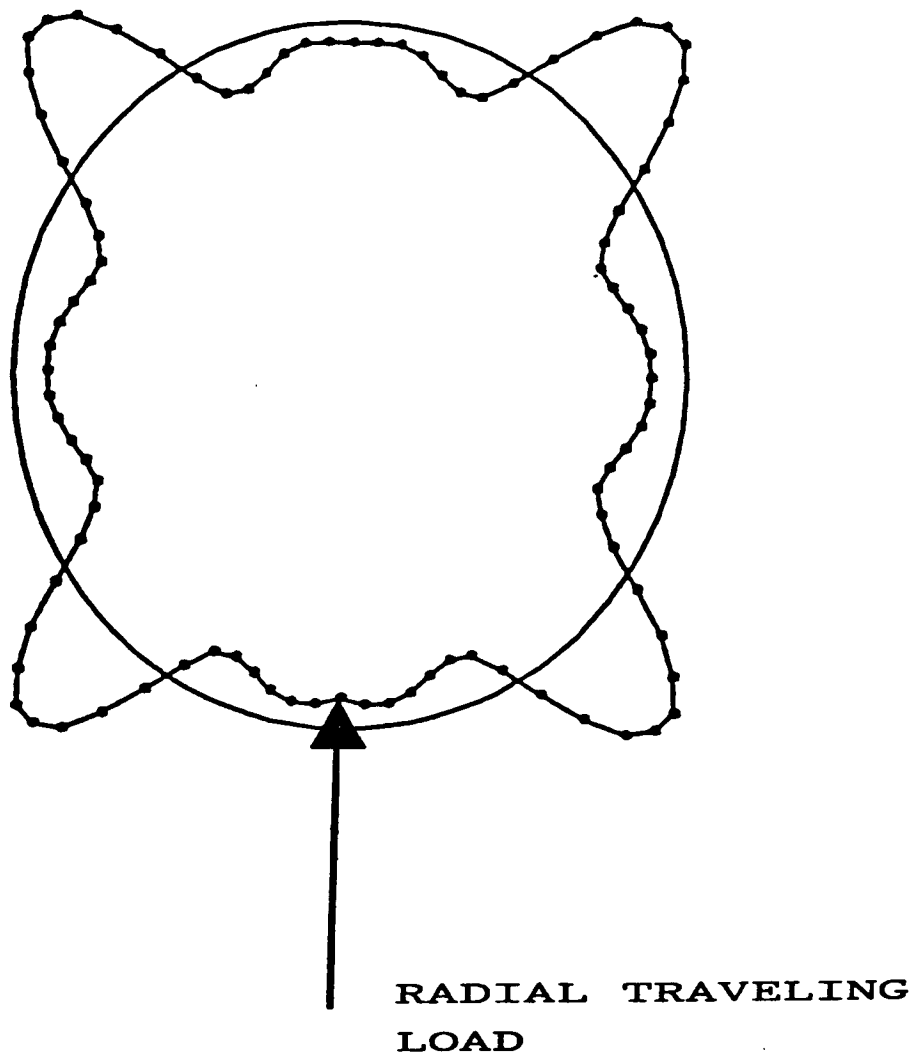
Fig. 5.18   RESPONSE OF THE TIRE'S
CROWN NODES AT 175.7
RAD/SEC (117 MPH) DUE TO
CIRCUMFERENTIALLY TRAVELING
RADIAL LOAD

RADIAL TRAVELING
LOAD
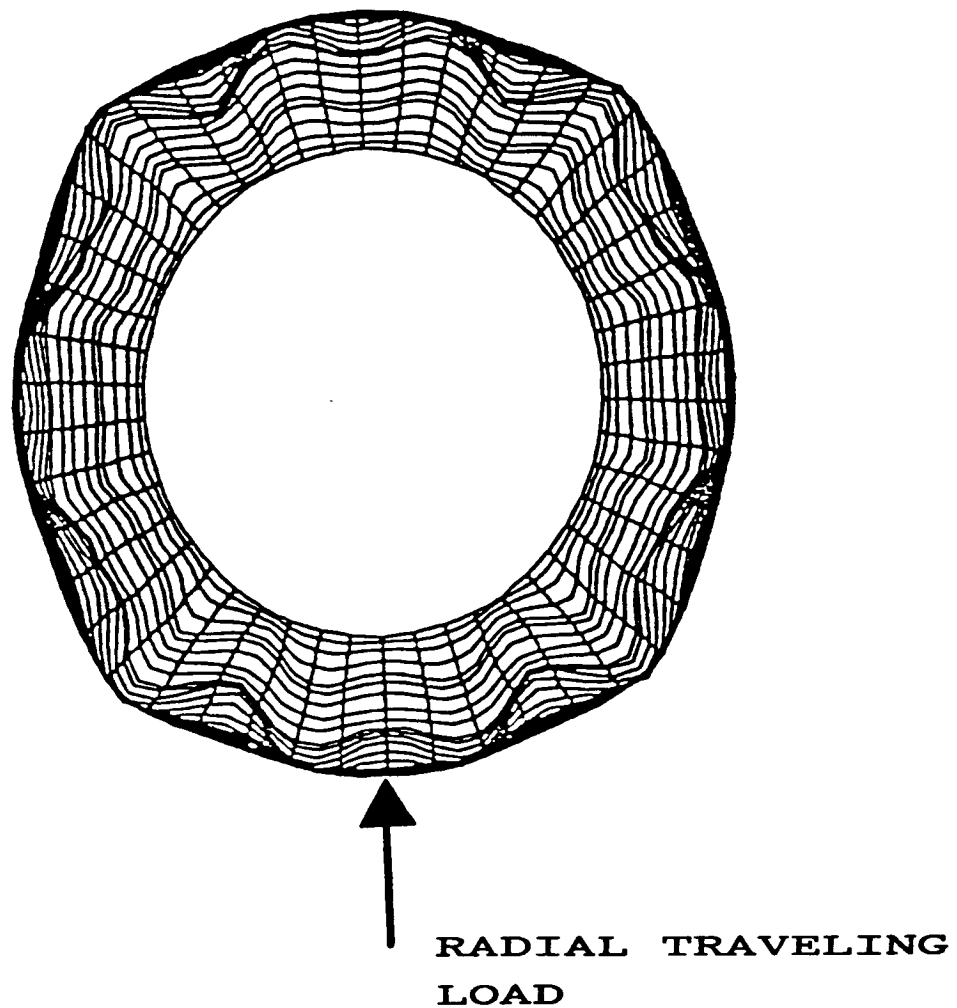
Fig. 5.19   SIDE VIEW OF THE FE MODEL
RESPONSE AT 175.7 (117 MPH)
DUE TO CIRCUMFERENTIALLY
TRAVELING RADIAL LOAD

RADIAL TRAVELING
LOAD
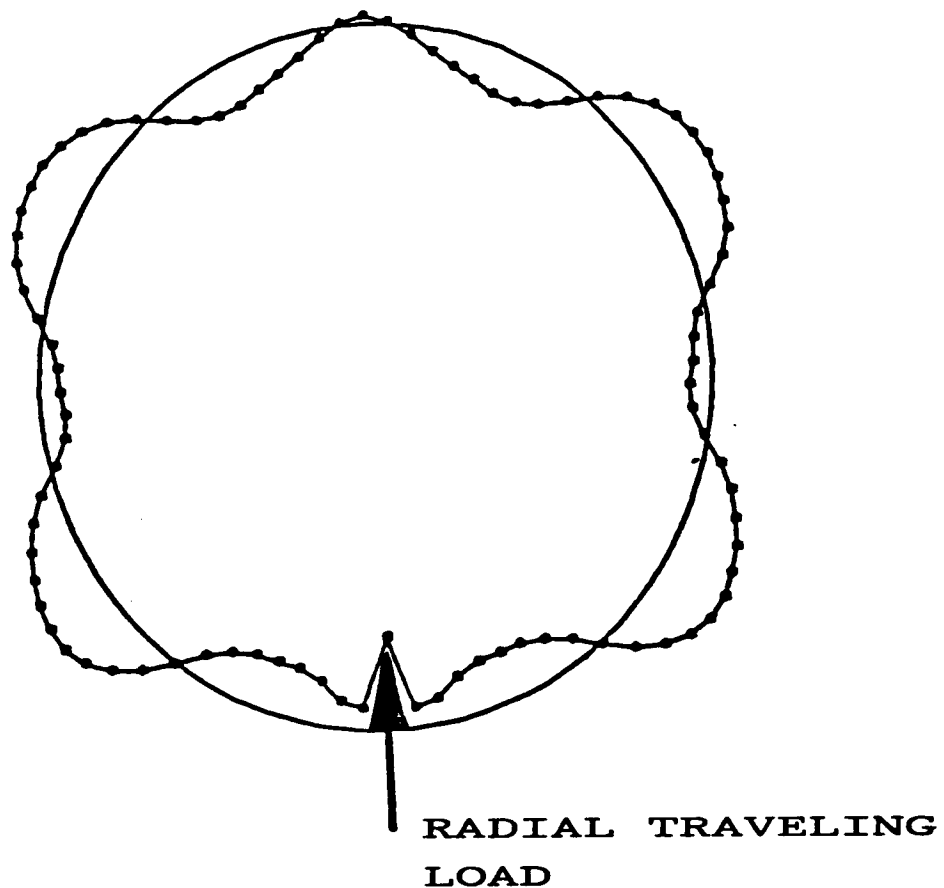
Fig. 5.20   RESPONSE OF THE TIRE'S CROWN
NODES AT 207 RAD/SEC (138 MPH)
DUE TO CIRCUMFERENTIALLY
TRAVELING RADIAL LOAD

RADIAL TRAVELING LOAD
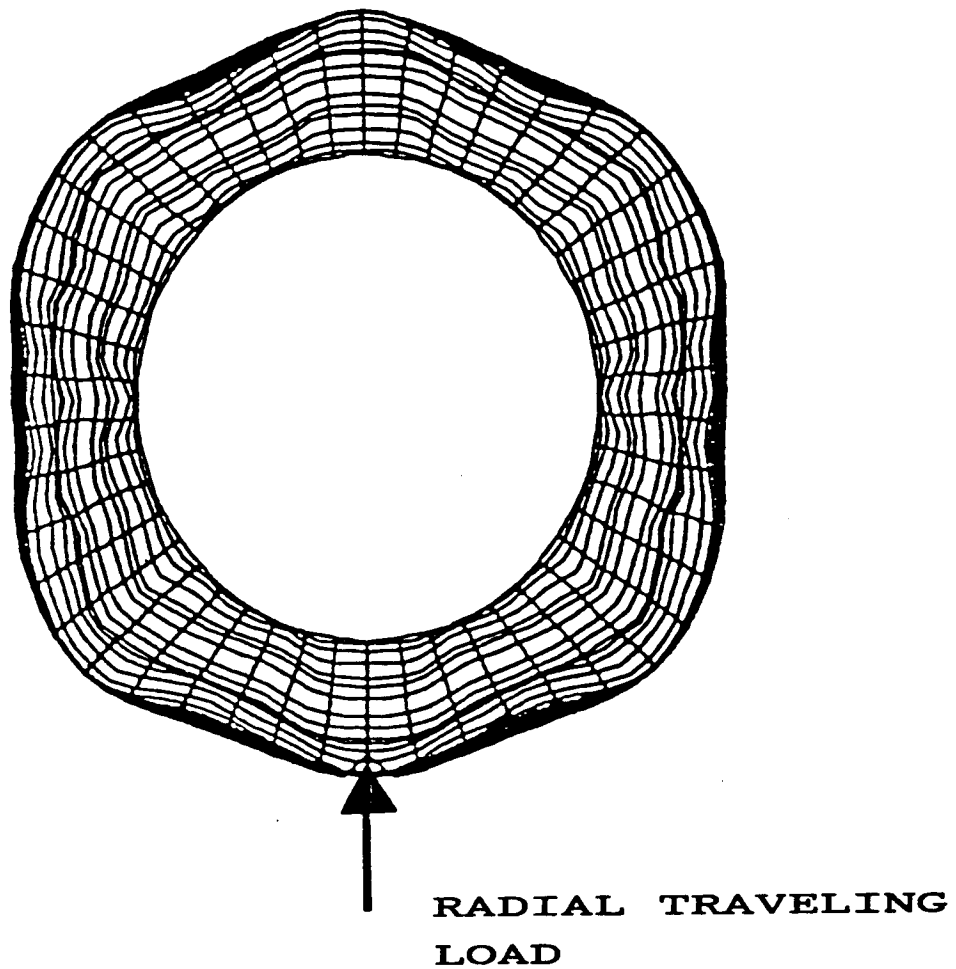
Fig. 5.21   SIDE VIEW OF THE FE MODEL
RESPONSE AT 207 RAD/SEC
(138 MPH) DUE TO CIRCUMFER-
ENTIALLY TRAVELING RADIAL
LOAD
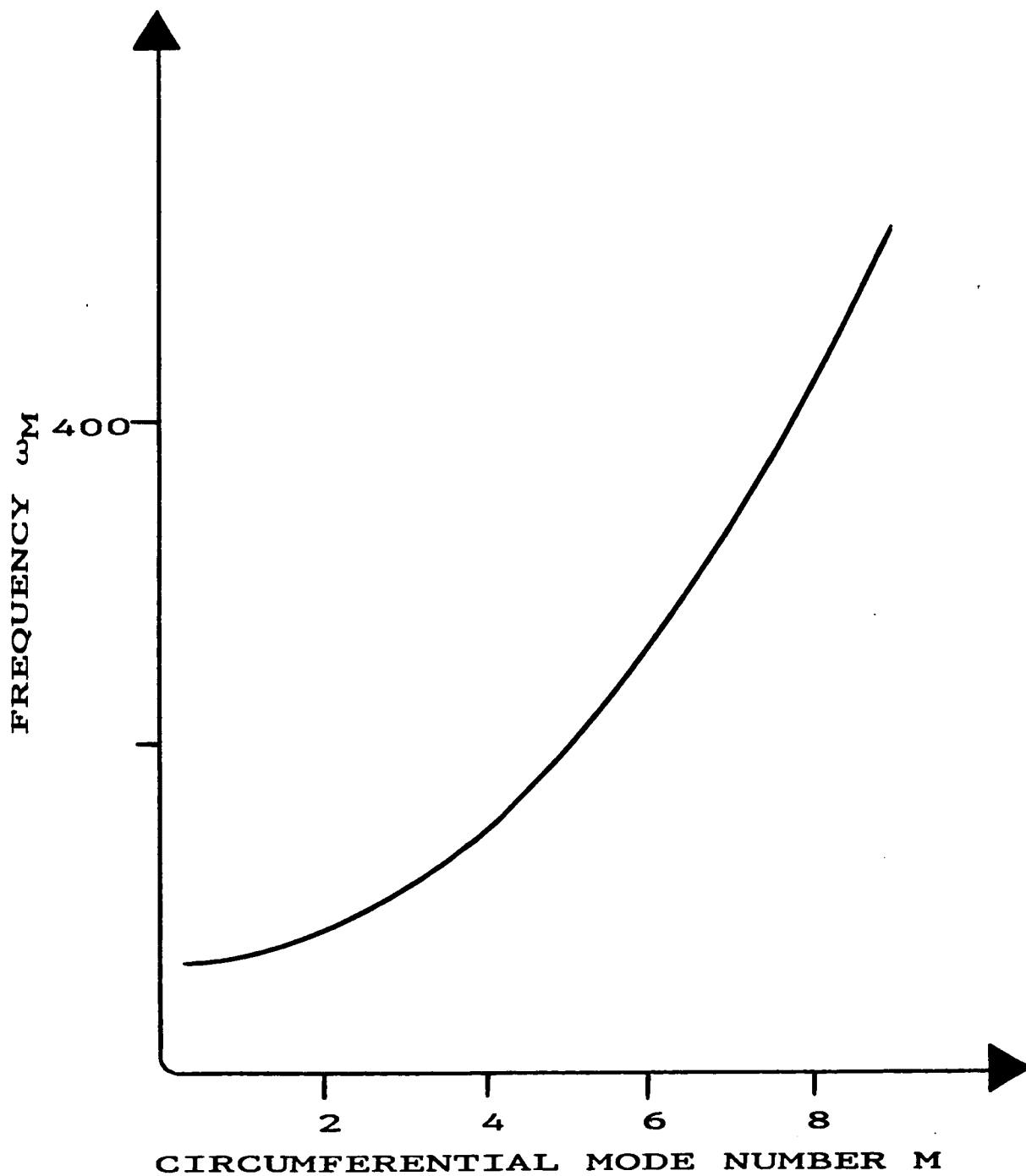
Fig. 5.22   TYPICAL FREQUENCY SPECTRUM
             CHARACTERISTICS TO CIRCUM-
             FERENTIAL MODE VARIATIONS
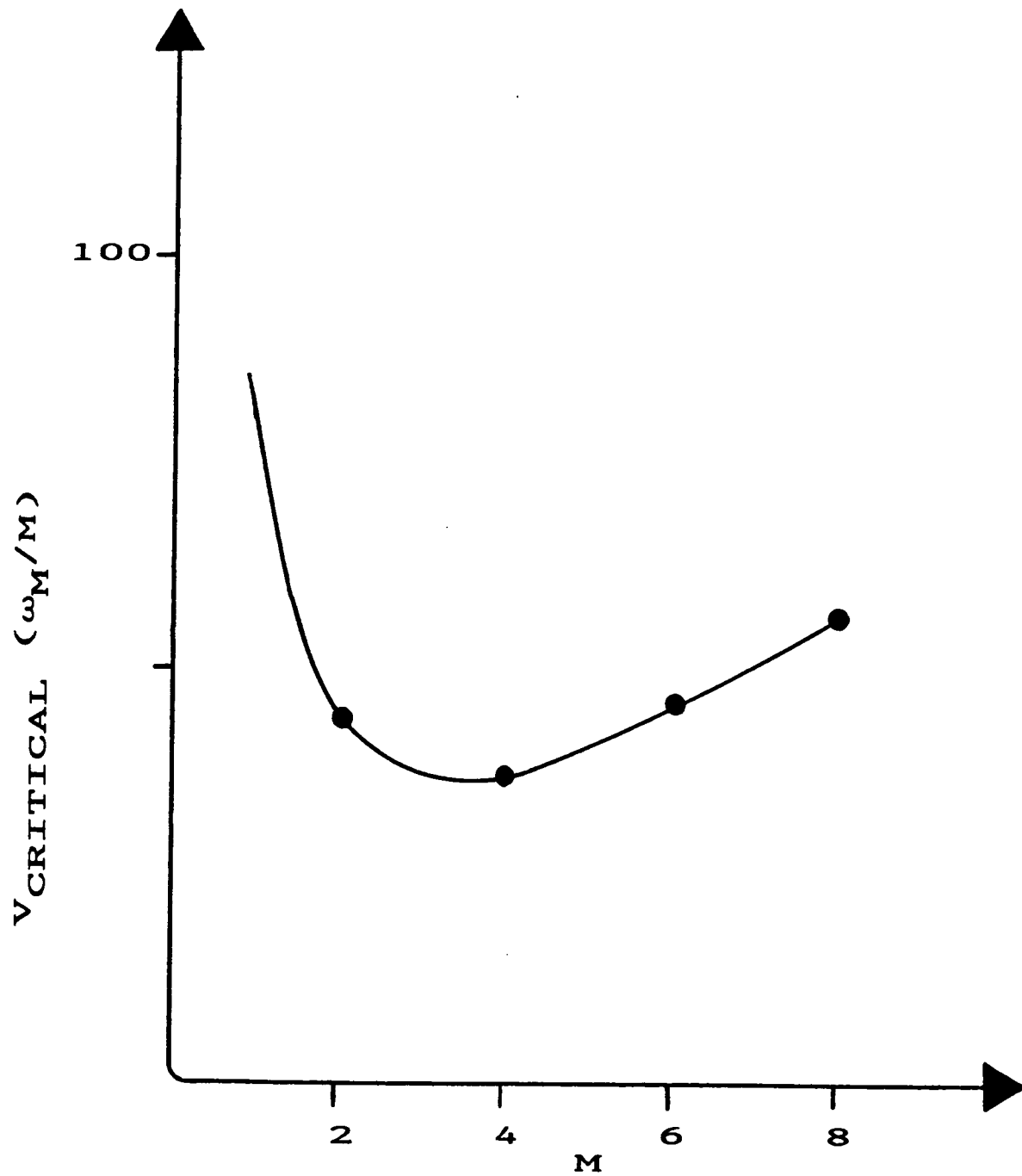
Fig. 5.23   CRITICAL VELOCITY
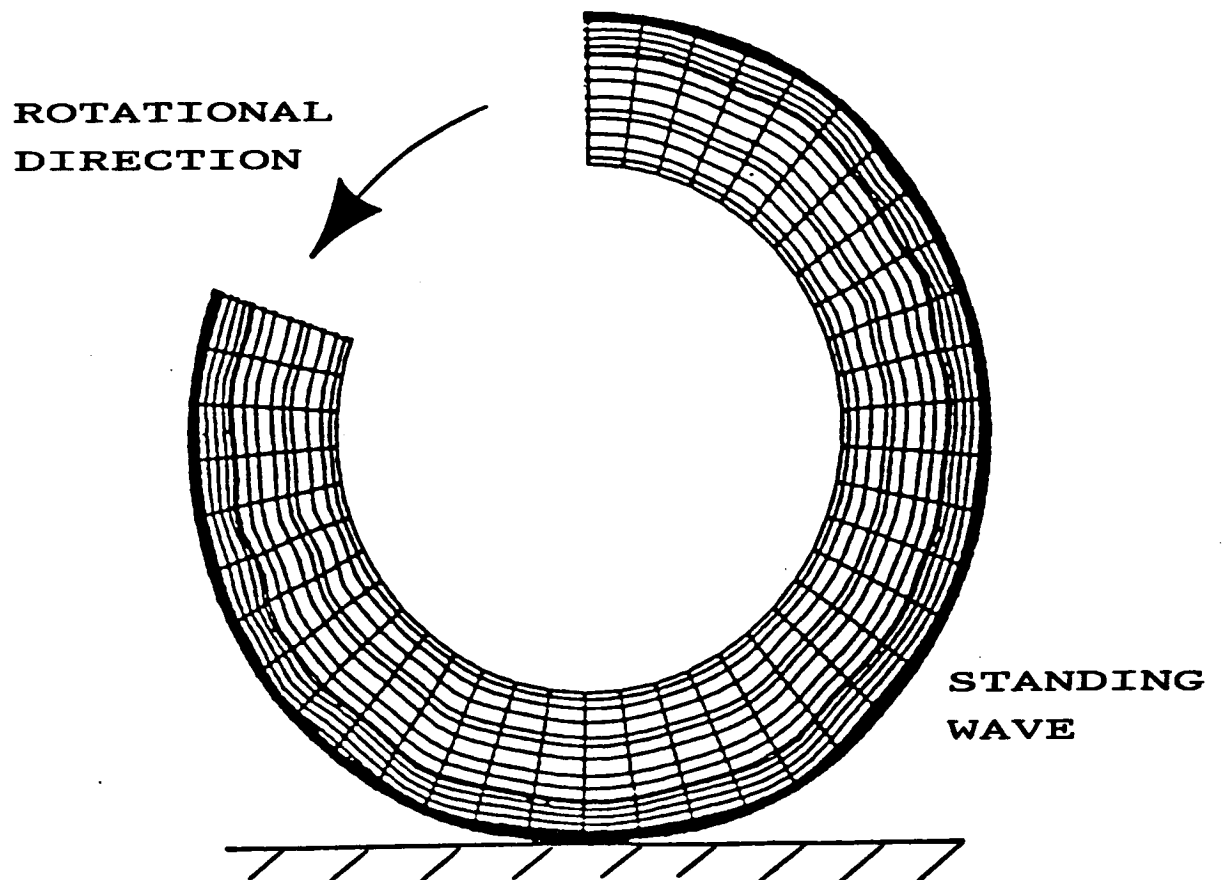RELATIONSHIP
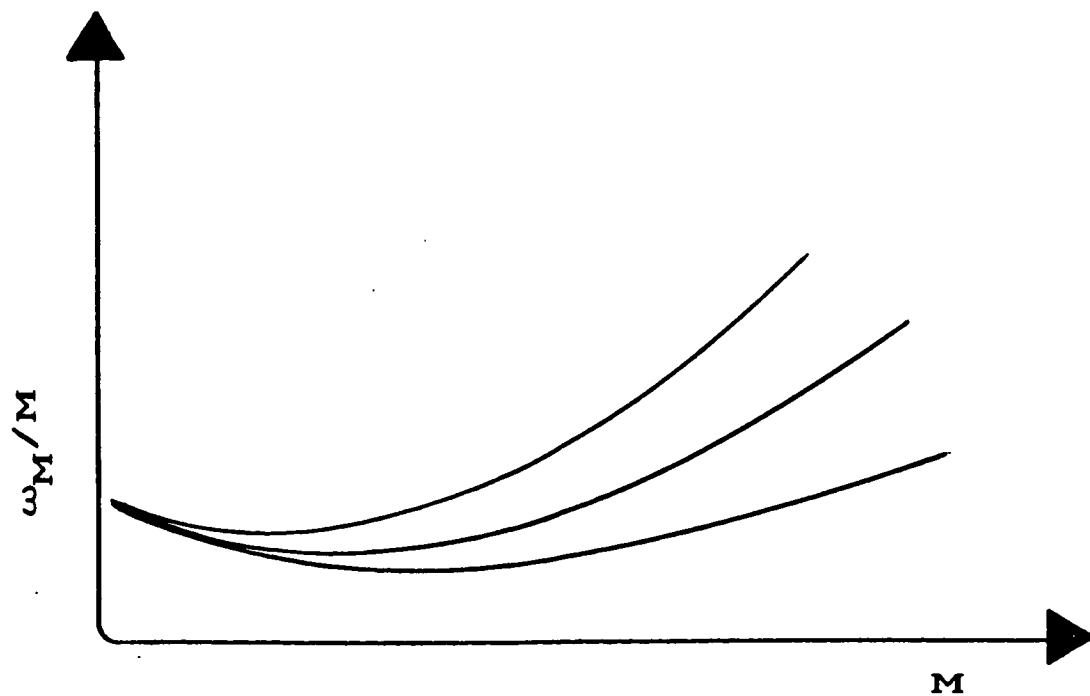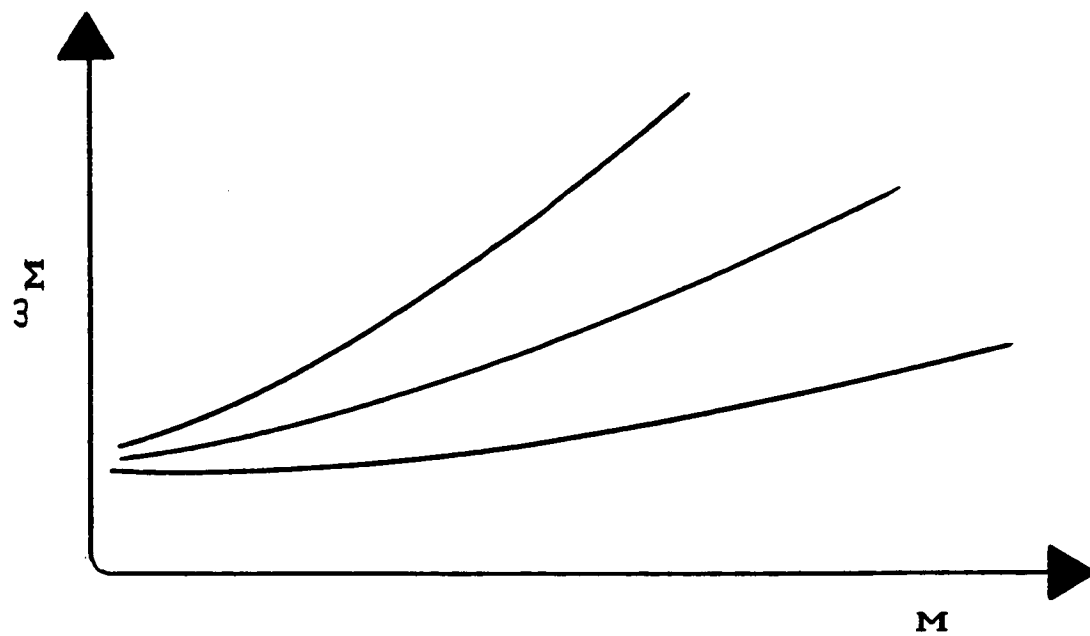
Fig. 5.24 EFFECTS OF FREQUENCY SPECTRAL
PROPERTIES ON CRITICAL SPEED
CHARACTERISTICS
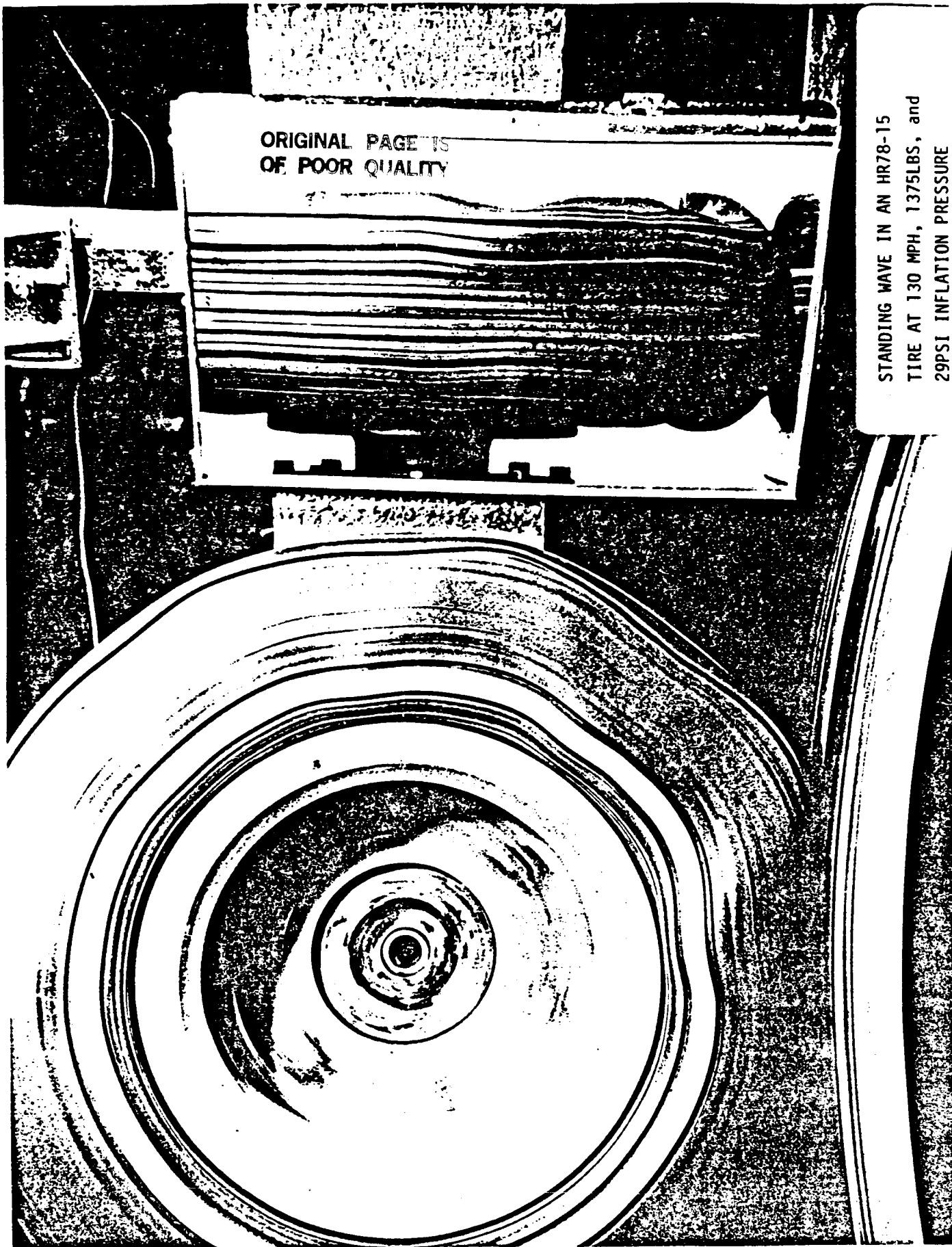
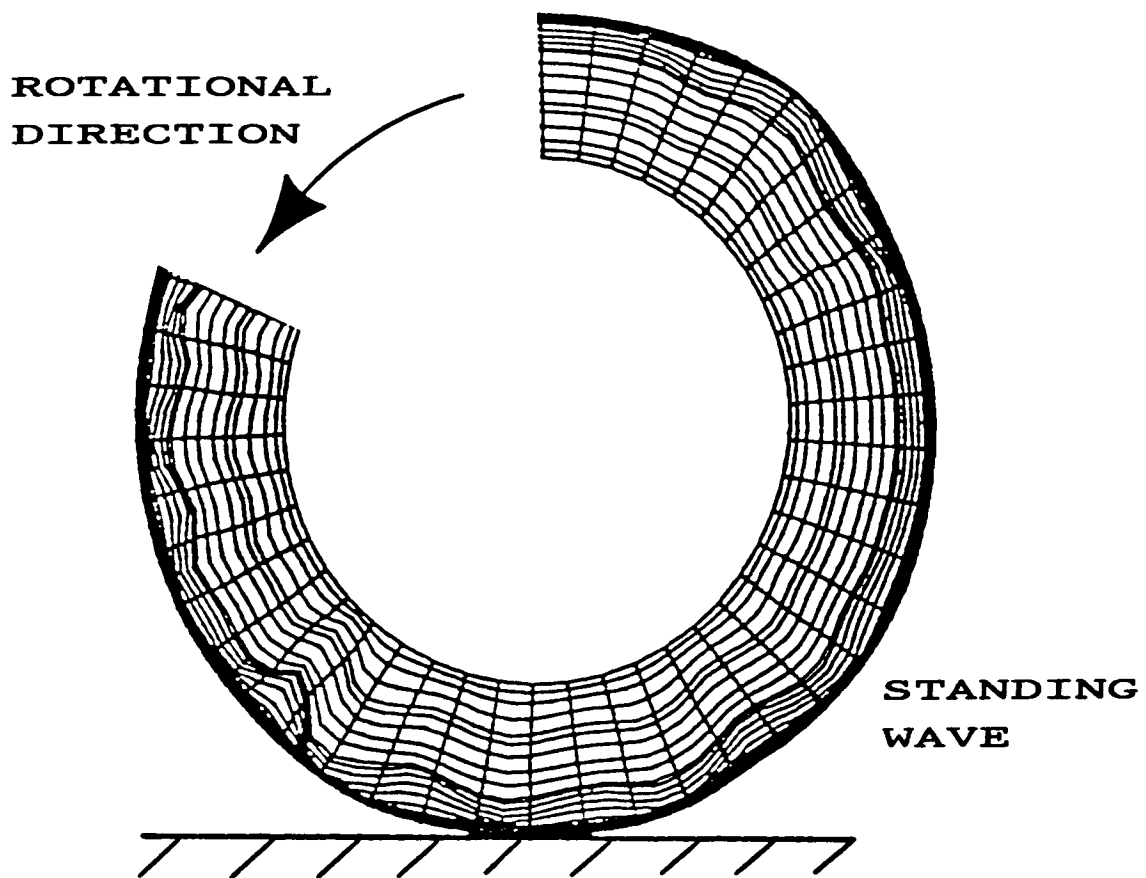STANDING WAVE IN AN HR78-15 TIRE AT 130 MPH, 1375LBS, and 29PSI INFLATION PRESSURE
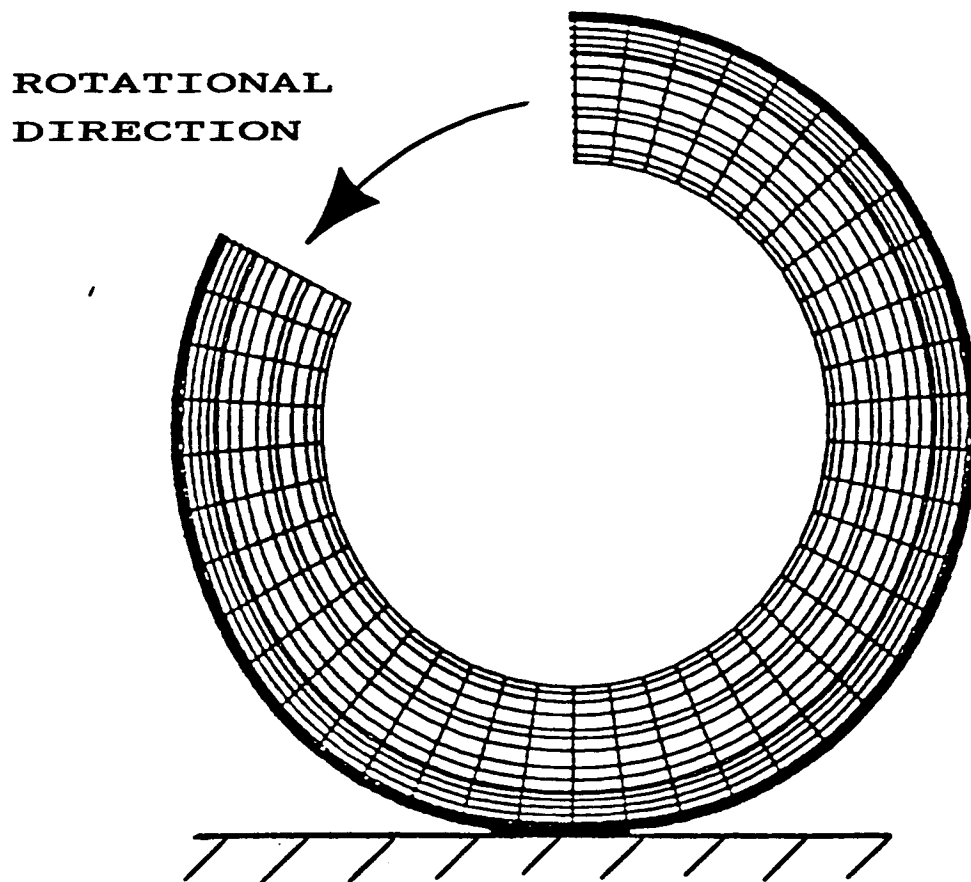
FIGURE 5.25

ROTATIONAL
DIRECTION

STANDING
WAVE

Fig. 5.26 RESPONSE OF THE DAMPED TIRE
MODEL ($\mu=10^{-4}$) ROTATING AT
175.7 RAD/SEC (117 MPH) IN
CONTACT WITH THE GROUND DUE
TO A .1 INCH AXLE DEFLECTION

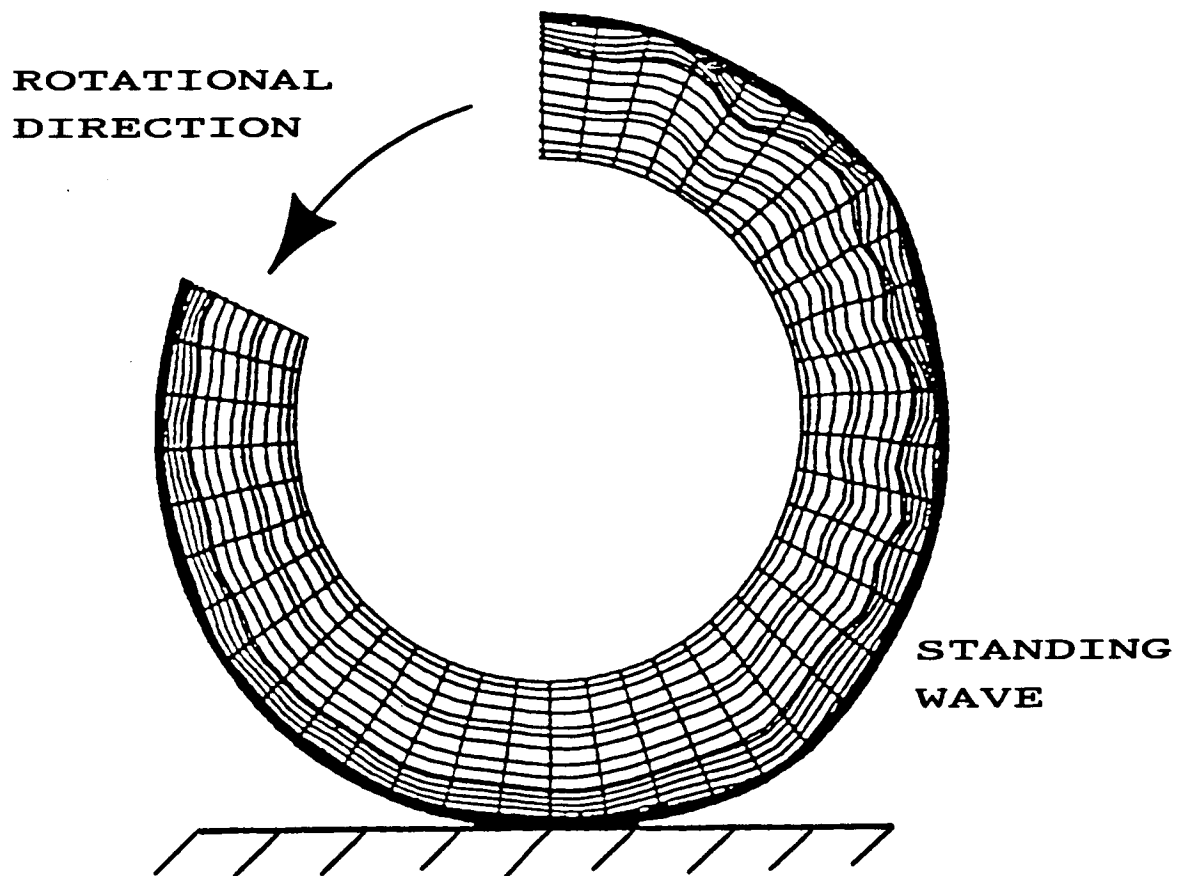ROTATIONAL
DIRECTION

STANDING
WAVE

Fig. 5.27   RESPONSE OF DAMPED TIRE MODEL
($\mu = 10^{-4}$) ROTATING AT 175.7
RAD/SEC (117 MPH) IN CONTACT
WITH GROUND DUE TO 1. INCH
AXLE DEFLECTION

ROTATIONAL
DIRECTION

Fig. 5.28   RESPONSE OF DAMPED TIRE MODEL
             ($\mu=1.5*10^{-4}$) ROTATING AT 175.7
             RAD/SEC (117 MPH) IN CONTACT
             WITH THE GROUND DUE TO A 0.1
             INCH AXLE DEFLECTION

Fig. 5.29   RESPONSE OF THE DAMPED TIRE
MODEL ($\mu=1.5*10^{-4}$) ROTATING
AT 175.7 RAD/SEC (117 MPH)
IN CONTACT WITH THE GROUND
DUE TO A 1. INCH AXLE DEFLEC-
TION